ALMA MATER STUDIORUM
UNIVERSITÀ DI BOLOGNA

DEPARTMENT OF ELECTRICAL, ELECTRONIC, AND INFORMATION ENGINEERING "GUGLIELMO MARCONI"

SECOND CYCLE DEGREE IN
ELECTRIC VEHICLE ENGINEERING

CONTROL AND ANALYSIS OF PERMANENT MAGNET DUAL-THREE-PHASE DRIVES

Supervisor:
Prof. Giacomo Sala

Candidate:
Gianluca Trentin

Co-Supervisors:
Prof. Michele Degano
Prof. Gabriele Rizzoli
Dr. Lorenzo Carbone
Dr. Meiqi Wang

Graduation session July 2025
Academic year 2024/2025

Abstract

Multiphase electric machines constitute a category of electric motors notable for high torque density, reliable operation, and robust performance under fault conditions, making them strong candidates for automotive propulsion. This thesis, conducted during a research period at the Power Electronics and Machine Centre of the University of Nottingham (UK), focuses on stability analysis and control strategies for multiphase electric machines.

Initially, an overview of the three-phase machines is presented, including the derivation of all fundamental equations and the associated reference frame transformations. This is followed by an analysis of the mathematical models and control schemes used for speed, torque, and current regulation. From this, the fundamental equations for dual-three-phase machines are derived, along with a description of their topologies and the methodology used for machine characterization.

A comprehensive inductance analysis is conducted for both Interior Permanent Magnet (IPM) and Surface Permanent Magnet (SPM) multiphase machines, accounting for linear and nonlinear $B-H$ material characteristics. Based on the derived values, classical, modified, and autotuned PI controllers are investigated, along with a comparison of various feedforward compensation techniques. The current control strategy is developed using the modular approach and the vector space decomposition (VSD). Furthermore, instead of relying on inductance values for flux estimation, a control strategy based on a flux observer is proposed and evaluated.

All control loops are implemented on the derived machine models to evaluate their effect on system stability and dynamic performance. For current control, which is modeled as a multiple-input multiple-output (MIMO) system, a state-space representation is developed and analyzed through eigenvalue analysis.

To validate the theoretical models and control algorithms, detailed studies are carried out in Matlab and Simulink. The simulation results are analyzed to compare the dynamic response and robustness of the various control strategies under a range of operating conditions, including different load torques and speed profiles.

Sommario

Le macchine elettriche multifase costituiscono una categoria di motori elettrici noti per l'elevata densità di coppia, il funzionamento affidabile e le prestazioni robuste in condizioni di guasto, rendendole forti candidate per la propulsione automobilistica. Questa tesi, svolta durante un periodo di ricerca presso il Power Electronics and Machine Centre dell'Università di Nottingham (Regno Unito), si focalizza sull'analisi della stabilità e sulle strategie di controllo per macchine elettriche multifase.

Inizialmente, viene presentata una panoramica delle macchine trifase, inclusa la derivazione di tutte le equazioni fondamentali e le trasformazioni del sistema di riferimento associate. Segue un'analisi dei modelli matematici e degli schemi di controllo utilizzati per la regolazione della velocità, della coppia e della corrente. Da ciò, vengono derivate le equazioni fondamentali per le macchine doppio trifase, insieme a una descrizione delle loro topologie e della metodologia utilizzata per la caratterizzazione della macchina.

Viene condotta un'analisi completa dell'induttanza sia per macchine multifase a magneti permanenti interni (IPM) sia per macchine a magneti permanenti superficiali (SPM), tenendo conto delle caratteristiche lineari e non lineari del materiale $B-H$. Sulla base dei valori ottenuti, vengono studiati controllori PI classici, modificati e autotunati, insieme a un confronto tra varie tecniche di compensazione in avanti. La strategia di controllo della corrente è sviluppata utilizzando l'approccio modulare e la decomposizione dello spazio vettoriale (VSD). Inoltre, anziché basarsi sui valori di induttanza per la stima del flusso, viene proposto e valutato un approccio di controllo che impiega un osservatore di flusso.

Tutti i loop di controllo sono implementati sui modelli derivati della macchina per valutarne l'impatto sulla stabilità del sistema e sulle prestazioni dinamiche. Nel caso del controllo di corrente, modellato come un sistema a ingressi e uscite multiple (MIMO), viene sviluppata una rappresentazione nello spazio degli stati e analizzata mediante analisi degli autovalori.

Per validare i modelli teorici e gli algoritmi di controllo, vengono condotte simulazioni dettagliate in Matlab e Simulink. I risultati delle simulazioni sono analizzati per confrontare la risposta dinamica e la robustezza delle varie strategie di controllo sotto una gamma di condizioni operative, inclusi diversi carichi di coppia e profili di velocità.

List of Terms

Latin letters

$\mathbf{A}$: state matrix

A_z: z-component of the magnetic vector potential normal to the analysis plane

$\mathbf{B}$: input matrix

B: viscous friction coefficient

B_x and B_y: flux density components

$\mathbf{C}$: constant matrix

C_1, C_2: constants determined by initial or boundary conditions

$\mathbf{D}$: output matrix

D_f: denominator factor

$\mathbf{E}$: feed-through matrix

e: current error

e_ω: speed error

f_{mod}: modulation frequency

f_{rk}: rotor MMF harmonic frequency for order k

f_{rp}: main rotor MMF harmonic frequency

f_{sample}: sampling frequency

f_{sk}: stator MMF harmonic frequency for order k

f_{sp}: main stator MMF harmonic frequency

f_{sw}: carrier signal

G: forward loop transfer function

G_{cl}: closed loop transfer function

G_{mec}: mechanical transfer function

G_{PI}: transfer function of classic PI

G_t: closed-loop transfer function

H: feedback transfer function

$\bar{i}^* = [i_d^*, i_q^*]^T$: reference current

$\bar{i}_{dq} = [i_d, i_q]^T$: current in dq frame

$\bar{i}_{abc} = [i_a, i_b, i_c]^T$: current in abc frame

J: rotor's moment of inertia

$\bar{J}$: current density

$\bar{K}$: surface current density

K_p: proportional gain

K_i: integral gain

k_{iron}: coefficient of iron losses

k_{mech}: coefficient of mechanical losses

L: active axial length

L_d: d-axis inductance

L_q: q-axis inductance

$\mathbf{L_{dq}}$: apparent inductance matrix in dq frame

$\mathbf{dL_{dq}}$: incremental inductance matrix in the dq frame

n: number of states in state space representation

n_x and n_y: surface normal vector's components

m: number of inputs in state space representation

m_i: modulation index

p: number of outputs in state space representation

P: number of pole pairs

$\bar{r}$: position vector

$\mathbf{R}$: stator resistance described as diagonal matrix

R_s: stator resistance

R_{rc}: radius from the rotor center

r_1: vector of an infinitesimal current located on the surface S_1, where it is evaluated A_z

r_2: vector of an infinitesimal current on the surface S_2, which generates the magnetic vector potential (A) at r_1

S_1 and S_2: slot cross-sectional areas

$\mathbf{T}$: transformation matrix

T_e: electric torque produced by the motor

T_e^*: reference electric torque

T_L: torque load

$\mathbf{T_{vsd}}$: VSD transformation matrix

$\bar{u}$: input vector

$\bar{v} = [v_d, v_q]^T$: voltage vector in dq frame

$\bar{v}_{abc} = [v_a, v_b, v_c]^T$: voltages in abc frame

$v_{\mathrm{c,pk}}$: peak amplitude of the carrier signal

v_{ff}: voltage from feedforward compensation

v_{in}: summing point input voltage with feedforward compensation

$v_{\mathrm{mod,pk}}$: peak amplitude of the modulation signal

$\bar{x}$: state vector

$(\bar{x}_e, \bar{u}_e)$: coordinates of the equilibrium point

$\bar{y}$: output vector

Greek letters

λ: eigenvalue
μ_0: magnetic permeability of free space
δ_{ij}: Kronecker delta
ω: electrical angular velocity of the motor
ω_c: control bandwidth
ω_m: mechanical angular velocity of the motor
ω_m^*: reference mechanical speed
ω_n: natural pulsation
θ: angular position
φ^*: target flux on a generic axis
$\hat{\varphi}$: flux estimated by the observer
$\bar{\varphi}_{abc} = [\varphi_a, \varphi_b, \varphi_c]^T$: magnetic flux linkages in abc frame
$\bar{\varphi}_{pm}$: permanent magnet flux linkage
ξ: damping factor
σ: Maxwell stress tensor

Abbreviations

DOF: Degrees Of Freedom
DMS: Decoupled Modular–Stator
DTP: Dual Three Phase
EMF: Electric Motive Force
$FEMM$: Finite Element Method Magnetics
GCD: Greatest Common Divisor
IPM: Interior Permanent Magnet
LUT: Lookup Tables
MMF: Magneto Motive Force
$MIMO$: Multiple Input Multiple Output
$MTPA$: Maximum Torque Per Ampere
$MTPE$: Maximum Torque Per Efficiency
PI: Proportional Integral
$PMSM$: Permanent Magnet Synchronous Motors
PWM: Pulse Width Modulation
$SISO$: Single Input Single Output

Contents

List of Figures

List of Tables

Chapter 1

Fundamentals of electric motors, power electronics, and controls

The architecture of a general electric powertrain, encompassing the electric motor, power electronic converter, and control system, forms the central theme of this introductory chapter. To effectively navigate the complexities inherent in multiphase electrical machines, this study adopts a progressive approach, initially establishing a robust understanding of the three-phase system.

1.1 Overview of three-phase drives

This chapter begins with the examination of conventional three-phase machine equations, establishing the mathematical framework necessary to develop equivalent multiphase machine models. Although three-phase machines are dominating the market due to their operational simplicity and mature control methodologies, they present several limitations. The fundamental constraints of three-phase architectures manifest primarily in their limited DOF that is possible to control. In the context of electric drives, the term DOF refers to the number of independent electrical variables that can be actively controlled to influence the electromagnetic behavior of the machine. This section provides a formal analysis of the degrees of freedom for both conventional three-phase and dual three-phase machines.

Three-phase machine

A three-phase machine includes three stator windings fed by a currents i_a, i_b, and i_c. Under balanced operating conditions, and assuming no neutral connection, these currents are constrained by Kirchhoff's current law, leading to the following condition:

$$i_a + i_b + i_c = 0 \tag{1.1}$$

This constraint implies that only two of the three phase currents are linearly independent. As a result, the number of electrical degrees of freedom is: $\mathrm{DOF}_{\mathrm{electrical}} = 3 - 1 = 2$
These two electrical degrees of freedom are typically exploited to independently control the torque-producing and the flux-producing components of the stator current. Although the physical implementation of such control is typically carried out in a transformed coordinate system, the existence of only two independent electrical variables remains fundamental.
Mechanically, the machine has one degree of freedom associated with the rotation of the rotor: $\mathrm{DOF}_{\mathrm{mechanical}} = 1$
Consequently, the total number of degrees of freedom is given by:

$$\mathrm{DOF}_{\mathrm{total}} = \mathrm{DOF}_{\mathrm{electrical}} + \mathrm{DOF}_{\mathrm{mechanical}} = 2 + 1 = 3 \tag{1.2}$$

One of the fundamental limitations of three-phase architectures is their inherently low DOF, which restricts fault tolerance and can lead to significant performance degradation or even complete system failure. This vulnerability poses a critical challenge in applications where continuous and reliable operation is essential. Additionally, three-phase systems typically exhibit higher torque ripple compared to multiphase alternatives, resulting in increased mechanical vibrations that can compromise operational smoothness and user comfort. From a power distribution standpoint, confining the electrical load to only three phases necessitates higher current in each winding, thereby increasing Joule losses and exacerbating thermal management issues.

Dual three-phase machine

A dual-three-phase machine consists of two independent three-phase winding sets, commonly referred to as sector A and sector B. Each has its stator currents: i_{a1}, i_{b1}, i_{c1} for sector A, and i_{a2}, i_{b2}, i_{c2} for sector B.
Assuming again that each sector operates under balanced conditions with no neutral connection, the following constraints apply:

$$\begin{cases} i_{a1} + i_{b1} + i_{c1} = 0 \\ i_{a2} + i_{b2} + i_{c2} = 0 \end{cases} \tag{1.3}$$

This results in two linear constraints among the six total phase currents. Therefore, the number of independent electrical variables is: $\mathrm{DOF}_{\mathrm{electrical}} = 6 - 2 = 4$
The rotor remains mechanically constrained to a single degree of freedom, representing its angular position: $\mathrm{DOF}_{\mathrm{mechanical}} = 1$
Hence, the total number of degrees of freedom in a dual three-phase machine is:

$$\mathrm{DOF}_{\mathrm{total}} = \mathrm{DOF}_{\mathrm{electrical}} + \mathrm{DOF}_{\mathrm{mechanical}} = 4 + 1 = 5 \tag{1.4}$$

The inherent redundancy of multiphase configurations provides robust fault tolerance, enabling continued operation despite partial winding failures, a capability of particular importance in aerospace propulsion and automotive traction systems where operational reliability directly impacts safety. The distributed nature of power transfer across multiple phases simultaneously reduces the current density in individual windings. Additionally, the increase in phase number inherently produces smoother torque, effectively addressing vibration and acoustic noise issues prevalent in conventional three-phase machines.

1.1.1 Machine equation

The following section outlines the derivation of the fundamental machine equations, which form the basis for developing the corresponding models for a dual-three-phase motor.
This approach enables the representation of phase voltages by synthesizing two fundamental physical principles that govern all electrical machines. The first is Ohm's law, which accounts for the resistive voltage drop across the machine windings. The second is the Faraday-Neumann-Lenz law, which describes the induced voltage components resulting from time-varying magnetic flux. By considering the three phase as three independent circuit, it is possible to express the phase voltage as following:

$$\begin{cases} v_a = R_s \cdot i_a + \frac{d\varphi_a}{dt} \\ v_b = R_s \cdot i_b + \frac{d\varphi_b}{dt} \\ v_c = R_s \cdot i_c + \frac{d\varphi_c}{dt} \end{cases} \tag{1.5}$$

Equation (1.5) can be rewritten in matrix format:

$$\begin{bmatrix} v_a \\ v_b \\ v_c \end{bmatrix} = R_s \cdot \begin{bmatrix} i_a \\ i_b \\ i_c \end{bmatrix} + \frac{d}{dt} \begin{bmatrix} \varphi_a \\ \varphi_b \\ \varphi_c \end{bmatrix} \tag{1.6}$$

The formula (1.6) can be rewritten in the stationary $\alpha\beta$ reference frame using the Clarke transformation, which converts all terms from the three-phase *abc* reference frame into two orthogonal components. This transformation is essential for simplifying both analysis and current control.

Clarke and Park transformation

Consider a general three-phase quantity u, composed of components u_a, u_b, and u_c, each separated by a phase shift of 120°. The figure 1.1 illustrates the three main reference frames:

- *abc* reference frame (three-phase system);

- Stationary $\alpha\beta$ frame (Clarke transformation);
- Rotating dq frame (Park transformation).

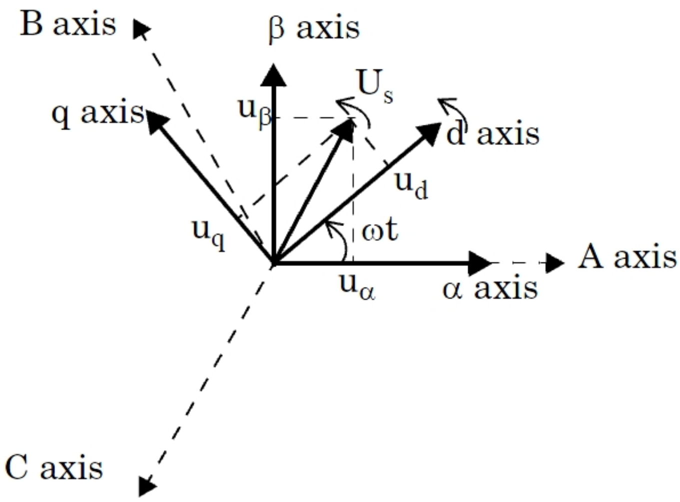

Figure 1.1: Reference frames

Clarke transformation

The Clarke transformation projects the three-phase system into two orthogonal axes:

- α-axis, aligned with phase a;
- β-axis, orthogonal to α, forming a 2D orthogonal basis.

Assuming a balanced system, the three phase vectors are separated by 120° in space and can be geometrically represented in the two-dimensional $\alpha\beta$ plane as follows:

$$\begin{cases} \bar{a} = \cos(0°)\,\hat{\imath} + \sin(0°)\,\hat{\jmath} = 1 \cdot \hat{\imath} \\ \bar{b} = \cos(120°)\,\hat{\imath} + \sin(120°)\,\hat{\jmath} = -\frac{1}{2} \cdot \hat{\imath} + \frac{\sqrt{3}}{2} \cdot \hat{\jmath} \\ \bar{c} = \cos(-120°)\,\hat{\imath} + \sin(-120°)\,\hat{\jmath} = -\frac{1}{2} \cdot \hat{\imath} - \frac{\sqrt{3}}{2} \cdot \hat{\jmath} \end{cases} \tag{1.7}$$

Considering a generic vector $\bar{u}$ in abc:

$$\bar{u} = u_a \cdot \bar{a} + u_b \cdot \bar{b} + u_c \cdot \bar{c} \tag{1.8}$$

Substituting (1.7) into (1.8):

$$\bar{u} = u_a \cdot (1 \cdot \hat{\imath}) + u_b \cdot (-\frac{1}{2} \cdot \hat{\imath} + \frac{\sqrt{3}}{2} \cdot \hat{\jmath}) + u_c \cdot (-\frac{1}{2} \cdot \hat{\imath} - \frac{\sqrt{3}}{2} \cdot \hat{\jmath}) \tag{1.9}$$

By separating the $\alpha\beta$ components, the following expressions can be obtained:

$$\begin{cases} u_\alpha = u_a - \frac{1}{2}u_b - \frac{1}{2}u_c \\ u_\beta = \frac{\sqrt{3}}{2}(u_b - u_c) \end{cases} \tag{1.10}$$

Assuming a balanced three-phase system, the sum of the phase components is zero. This allows one phase to be expressed in terms of the others, as follows:

$$u_a + u_b + u_c = 0 \quad \Rightarrow \quad u_c = -u_a - u_b \tag{1.11}$$

To preserve the vector results between the original three-phase system and its orthogonal projection, the following relationship must be satisfied:

$$\|u_{abc}\| = \|u_{\alpha\beta}\| \Rightarrow u_a^2 + u_b^2 + u_c^2 = u_\alpha^2 + u_\beta^2 \tag{1.12}$$

The first term of (1.12), in accordance with (1.11), is:

$$u_a^2+u_b^2+u_c^2 = u_a^2+u_b^2+(-u_a-u_b)^2 = u_a^2+u_b^2+u_a^2+2u_au_b+u_b^2 = 2u_a^2+2u_b^2+2u_au_b \tag{1.13}$$

The second term of (1.12), in accordance with (1.10), is:

$$\begin{aligned} u_\alpha^2 + u_\beta^2 &= \left(u_a - \frac{1}{2}u_b - \frac{1}{2}u_c\right)^2 + \left(\frac{\sqrt{3}}{2}(u_b - u_c)\right)^2 \\ &= \left(u_a - \frac{1}{2}u_b - \frac{1}{2}u_c\right)^2 + \frac{3}{4}(u_b - u_c)^2 \\ &= \left(u_a^2 - u_au_b - u_au_c + \frac{1}{4}u_b^2 + \frac{1}{2}u_bu_c + \frac{1}{4}u_c^2\right) + \frac{3}{4}(u_b^2 - 2u_bu_c + u_c^2) \\ &= u_a^2 - u_au_b - u_au_c + \frac{1}{4}u_b^2 + \frac{1}{2}u_bu_c + \frac{1}{4}u_c^2 + \frac{3}{4}u_b^2 - \frac{3}{2}u_bu_c + \frac{3}{4}u_c^2 \\ &= u_a^2 - u_au_b - u_au_c + u_b^2 - u_bu_c + u_c^2 \end{aligned} \tag{1.14}$$

Substitute (1.11) into the expression (1.14):

$$\begin{aligned} u_\alpha^2 + u_\beta^2 &= u_a^2 - u_au_b - u_a(-u_a - u_b) + u_b^2 - u_b(-u_a - u_b) + (-u_a - u_b)^2 \\ &= u_a^2 - u_ai_b + u_a^2 + u_au_b + u_b^2 + u_au_b + u_b^2 + u_a^2 + 2u_av_b + u_b^2 \\ &= 3u_a^2 + 3u_b^2 + 3u_au_b \end{aligned} \tag{1.15}$$

Finally, equation (1.12) can be validated by combining equations (1.13) and (1.15):

$$(u_\alpha^2 + u_\beta^2) = \frac{2}{3}(u_a^2 + u_b^2 + u_c^2) \tag{1.16}$$

In conclusion, combining the equations (1.10) and (1.16) is possible to obtain:

$$\begin{bmatrix} u_\alpha \\ u_\beta \end{bmatrix} = \frac{2}{3} \begin{bmatrix} 1 & -\frac{1}{2} & -\frac{1}{2} \\ 0 & \frac{\sqrt{3}}{2} & -\frac{\sqrt{3}}{2} \end{bmatrix} \begin{bmatrix} u_a \\ u_b \\ u_c \end{bmatrix} \tag{1.17}$$

In most cases, this equation is derived by incorporating the common-mode terms x_0 mathematically defined as: $x_0 = \frac{1}{3}(x_a + x_b + x_c)$
Summarizing these equations together is possible to obtain the following:

$$\begin{bmatrix} u_\alpha \\ u_\beta \\ u_0 \end{bmatrix} = \frac{2}{3} \underbrace{\begin{bmatrix} 1 & -\frac{1}{2} & -\frac{1}{2} \\ 0 & \frac{\sqrt{3}}{2} & -\frac{\sqrt{3}}{2} \\ \frac{1}{2} & \frac{1}{2} & \frac{1}{2} \end{bmatrix}}_{\mathbf{T}_{abc\to\alpha\beta}} \begin{bmatrix} u_a \\ u_b \\ u_c \end{bmatrix} \tag{1.18}$$

Considering equation (1.6) and multiplying each term for the transformation matrix $\mathbf{T}_{abc\to\alpha\beta}$ is it possible to define the following new terms:

$$\begin{bmatrix} v_\alpha \\ v_\beta \\ v_0 \end{bmatrix} = \mathbf{T}_{abc\to\alpha\beta} \begin{bmatrix} v_a \\ v_b \\ v_c \end{bmatrix}, \begin{bmatrix} i_\alpha \\ i_\beta \\ i_0 \end{bmatrix} = \mathbf{T}_{abc\to\alpha\beta} \begin{bmatrix} i_a \\ i_b \\ i_c \end{bmatrix}, \begin{bmatrix} \varphi_\alpha \\ \varphi_\beta \\ v_0 \end{bmatrix} = \mathbf{T}_{abc\to\alpha\beta} \begin{bmatrix} \varphi_a \\ \varphi_b \\ \varphi_c \end{bmatrix} \tag{1.19}$$

The previous equation can be reformulated using the following notation, which represents the machine equation in the $\alpha\beta$ reference frame:

$$\begin{bmatrix} v_\alpha \\ v_\beta \\ v_0 \end{bmatrix} = R_s \begin{bmatrix} i_\alpha \\ i_\beta \\ i_0 \end{bmatrix} + \begin{bmatrix} \varphi_\alpha \\ \varphi_\beta \\ v_0 \end{bmatrix} \tag{1.20}$$

Park transformation

Considering the vector:

$$\bar{u}_{\alpha\beta} = u_\alpha + j u_\beta \tag{1.21}$$

Now consider a new reference frame, denoted as the *d-q* frame, which is rotated by an angle θ with respect to the stationary α-β frame. The transformation of coordinates from the α-β frame to the *d-q* frame can be mathematically described by:

$$\bar{u}_{dq} = \bar{u}_{\alpha\beta} \cdot e^{-j\theta} \tag{1.22}$$

Substituting (1.21) inside (1.22):

$$\bar{u}_{dq} = u_\alpha \cdot cos(\theta) + u_\beta \cdot sin(\theta) + j(-u_\alpha \cdot sin(\theta) + u_\beta \cdot cos(\theta)) \tag{1.23}$$

To distinguish between the two reference frames, the transformation can be expressed in matrix form as follows:

$$\begin{bmatrix} u_d \\ u_q \end{bmatrix} = \underbrace{\begin{bmatrix} \cos(\theta_e) & \sin(\theta_e) \\ -\sin(\theta_e) & \cos(\theta_e) \end{bmatrix}}_{\mathbf{T}_{\alpha\beta \to \ dq}} \begin{bmatrix} u_\alpha \\ u_\beta \end{bmatrix} \tag{1.24}$$

In general, the equation (1.20) can be transformed into the dq reference frame by multiplying both sides of the equation by the Park transformation matrix $\mathbf{T}_{\alpha\beta \to \ dq}$:

$$\mathbf{T}_{\alpha\beta \to \ dq} \cdot \begin{bmatrix} v_\alpha \\ v_\beta \end{bmatrix} = \mathbf{T}_{\alpha\beta \to \ dq} \cdot R_s \cdot \begin{bmatrix} i_\alpha \\ i_\beta \end{bmatrix} + \mathbf{T}_{\alpha\beta \to \ dq} \cdot \frac{d}{dt} \begin{bmatrix} \varphi_\alpha \\ \varphi_\beta \end{bmatrix} \tag{1.25}$$

In accordance with the general equation (1.24) it is possible to obtain:

$$\begin{bmatrix} v_d \\ v_q \end{bmatrix} = R_s \begin{bmatrix} i_d \\ i_q \end{bmatrix} + \mathbf{T}_{\alpha\beta \to \ dq} \cdot \frac{d}{dt} \begin{bmatrix} \varphi_\alpha \\ \varphi_\beta \end{bmatrix} \tag{1.26}$$

The previous equation is not fully developed, as the flux terms are more complex to handle due to their dependence on the electrical angle. To completely transform the equation in the dq reference frame, it is necessary to rewrite the fluxes as follows:

$$\begin{bmatrix} \varphi_\alpha \\ \varphi_\beta \end{bmatrix} = (\mathbf{T}_{\alpha\beta \to \ dq})^{-1} \begin{bmatrix} \varphi_d \\ \varphi_q \end{bmatrix} \tag{1.27}$$

Where the inverse of the Park matrix transformation is the following:

$$(\mathbf{T}_{\alpha\beta \to \ dq})^{-1} = \begin{bmatrix} \cos(\theta_e) & -\sin(\theta_e) \\ \sin(\theta_e) & \cos(\theta_e) \end{bmatrix} \tag{1.28}$$

Applying the derivative:

$$\frac{d}{dt} (\mathbf{T}_{\alpha\beta \to \ dq})^{-1} = \omega_e \begin{bmatrix} -\sin(\theta_e) & -\cos(\theta_e) \\ \cos(\theta_e) & -\sin(\theta_e) \end{bmatrix} \tag{1.29}$$

Rewrite equation (1.26) with the previous substitution:

$$\begin{bmatrix} v_d \\ v_q \end{bmatrix} = R_s \cdot \begin{bmatrix} i_d \\ i_q \end{bmatrix} + \frac{d}{dt} \begin{bmatrix} \varphi_d \\ \varphi_q \end{bmatrix} + \mathbf{T}_{\alpha\beta \to \ dq} \cdot \frac{d}{dt} (\mathbf{T}_{\alpha\beta \to \ dq})^{-1} \cdot \begin{bmatrix} \varphi_d \\ \varphi_q \end{bmatrix} \tag{1.30}$$

Where is it possible to rewrite:

$$\mathbf{T}_{\alpha\beta \to \ dq} \cdot \frac{d}{dt} (\mathbf{T}_{\alpha\beta \to \ dq})^{-1} = \begin{bmatrix} \cos(\theta) & \sin(\theta) \\ -\sin(\theta) & \cos(\theta) \end{bmatrix} \cdot \omega \cdot \begin{bmatrix} \cos(\theta) & -\sin(\theta) \\ \sin(\theta) & \cos(\theta) \end{bmatrix} \tag{1.31}$$

Remembering the identity $\sin^2(\theta) + \cos^2(\theta) = 1$ and simplifying terms with opposite signs, it is possible to obtain:

$$\mathbf{T}_{\alpha\beta\to\ dq} \cdot \frac{d}{dt} \left(\mathbf{T}_{\alpha\beta\to\ dq}\right)^{-1} = \begin{bmatrix} 0 & -\omega \\ \omega & 0 \end{bmatrix} \tag{1.32}$$

Finally, the resulting equation, in accordance with [6], is:

$$\begin{bmatrix} v_d \\ v_q \end{bmatrix} = R_s \cdot \begin{bmatrix} i_d \\ i_q \end{bmatrix} + \frac{d}{dt} \begin{bmatrix} \varphi_d \\ \varphi_q \end{bmatrix} + \begin{bmatrix} 0 & -\omega \\ \omega & 0 \end{bmatrix} \cdot \begin{bmatrix} \varphi_d \\ \varphi_q \end{bmatrix} \tag{1.33}$$

1.1.2 Current control

A proportional-integral controller is a widely used control strategy in automatic control systems. Its aim is to minimize the error between a desired reference signal and the actual output of a system by adjusting the control input. The PI controller achieves this by combining two types of control actions:

- **Proportional term (P):** generates a control signal that is directly proportional to the current error. This term plays a significant role during transient phases, particularly when the error changes rapidly;
- **Integral term (I):** produces a control action based on the cumulative sum of past errors over time. This term becomes especially important in steady-state conditions, as even small errors persisting over a long duration can accumulate.

Mathematically, the control signal $u(t)$ generated by the PI controller is expressed as:

$$u(t) = K_p \cdot e(t) + K_i \int_0^t e(\tau) \cdot d\tau \tag{1.34}$$

where $e(t) = y_{ref}(t) - y(t)$.
Taking the Laplace transform of the time-domain PI controller, and assuming zero initial conditions, the control signal $U(s)$ in the frequency domain becomes:

$$U(s) = K_p \cdot E(s) + \frac{K_i}{s} \cdot E(s) = \left(K_p + \frac{K_i}{s}\right) \cdot E(s) \tag{1.35}$$

Where the terms that describe the transfer function of the classic PI become:

$$G_{PI}(s) = \frac{U(s)}{E(s)} = K_p + \frac{K_i}{s} \tag{1.36}$$

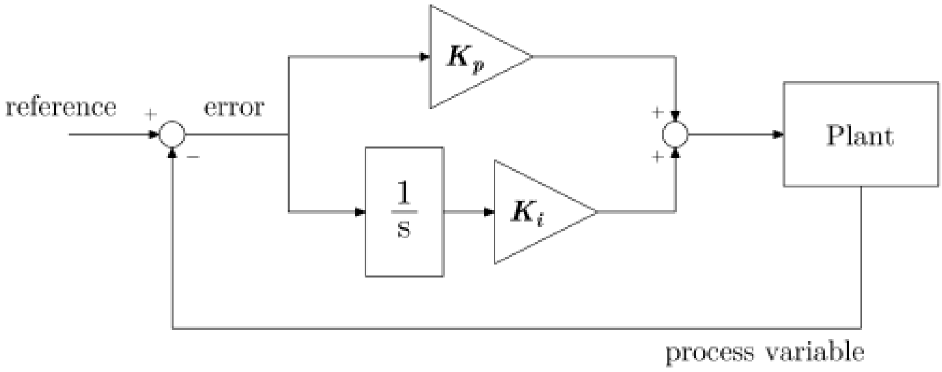

Figure 1.2: Classic PI scheme [1]

PI controller does not operate effectively when dealing directly with sinusoidal variables, due to the continuously oscillating nature of the error signals. This limitation is one of the key motivations behind the introduction of the dq transformation. By transforming the three-phase quantities into a rotating reference frame aligned with the rotor, the sinusoidal signals become steady-state values.
In this synchronous reference frame, two independent PI controllers can be employed, one for each axis (d and q), enabling effective decoupling of flux and torque control. This technique, which decomposes the stator current vector into two orthogonal components, i_d and i_q, is known as **field oriented control**.
From the machine equations presented in (1.33), the Laplace domain representation can be derived:

$$\begin{cases} V_d(s) = R_s\, I_d + sL_dI_d - \omega L_qI_q \\ V_q(s) = R_s\, I_q + sL_qI_q + \omega L_dI_d + \omega\varphi_{pm} \end{cases} \tag{1.37}$$

To obtain the plant's transfer function, it is necessary to rearrange the terms:

$$\begin{cases} V_d(s) + \omega L_qI_q = R_s\, I_d + sL_dI_d \\ V_q(s) - \omega L_dI_d = R_s\, I_q + sL_qI_q + \omega\varphi_{pm} \end{cases} \tag{1.38}$$

Where it is possible to define:

$$\begin{cases} U_d = V_d(s) + \omega L_qI_q \\ U_q = V_q(s) - \omega L_dI_d - \omega\varphi_{pm} \end{cases} \tag{1.39}$$

According to equation (1.35), and considering the error defined as $E = I^* - I$, the control output U can be expressed as follows:

$$\begin{cases} U_d = K_{p,d} \cdot (I_d^* - I_d) + \dfrac{K_{i,d}}{s} \cdot (I_d^* - I_d) \\ U_q = K_{p,q} \cdot (I_q^* - I_q) + \dfrac{K_{i,q}}{s} \cdot (I_q^* - I_q) \end{cases} \tag{1.40}$$

In conclusion, the transfer function of the plant can be expressed as follows:

$$\begin{cases} G_{plant,d} = \dfrac{U_d}{I_d} = \dfrac{1}{sL_d + R_s} \\ G_{plant,q} = \dfrac{U_q}{I_q} = \dfrac{1}{sL_q + R_s} \end{cases} \tag{1.41}$$

Having thoroughly analyzed the transfer functions of both the PI controller and the plant, I will now proceed to examine the closed-loop transfer function of the overall system. This comprehensive representation is fundamental for the setting of the proportional and integral gain.

Combining the equations (1.38), (1.40), (1.41) with the standard closed-loop transfer function formula $G_t(s) = \frac{G(s)}{1+G(s)H(s)}$ and considering the block diagram shown in figure 1.3, the closed-loop transfer function can be expressed as:

$$\begin{cases} G_{cl,d}(s) = \dfrac{\frac{sK_{p,d}+K_{i,d}}{Ld}}{s^2 + \frac{Kp,d+Rs}{Ld}s + \frac{K_{i,d}}{L_d}} \\ G_{cl,q}(s) = \dfrac{\frac{sK_{p,q}+K_{i,q}}{Lq}}{s^2 + \frac{Kp,q+Rs}{Lq}s + \frac{K_{i,q}}{L_q}} \end{cases} \tag{1.42}$$

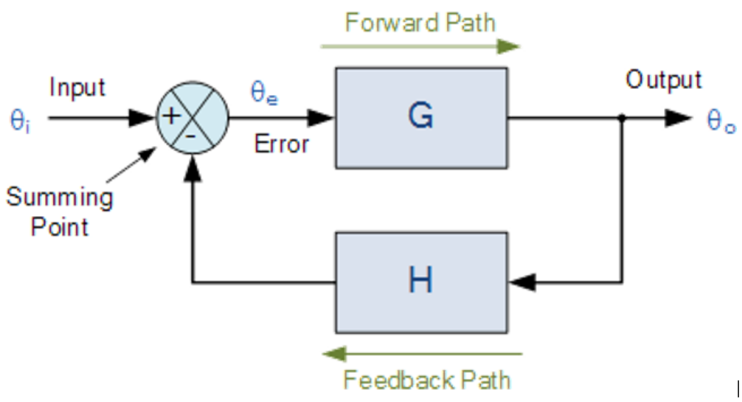

Figure 1.3: Closed loop transfer function

Given that the sole distinction in equation (1.42) lies in the reference frame, the system dynamics can be expressed in a generalized form. This unified representation captures the underlying symmetry of the equations while maintaining their fundamental structure:

$$G_{cl}(s) = \frac{\frac{sK_p+K_i}{L}}{s^2 + \frac{Kp+Rs}{L}s + \frac{K_i}{L}} \tag{1.43}$$

To determine the proportional and integral gains, the corresponding transfer function must be compared with the standard form of a second-order system:

$$G(s) = \frac{\omega_c^2}{s^2 + 2\omega_c s + \omega_c^2} \tag{1.44}$$

The transfer function in equation (1.43) exhibits a mismatch with respect to the standard transfer function (1.44), as evidenced by ω_c. To address this inconsistency, a reformulation of the control structure, referred to as the **modified PI** controller [1], is proposed in the following:

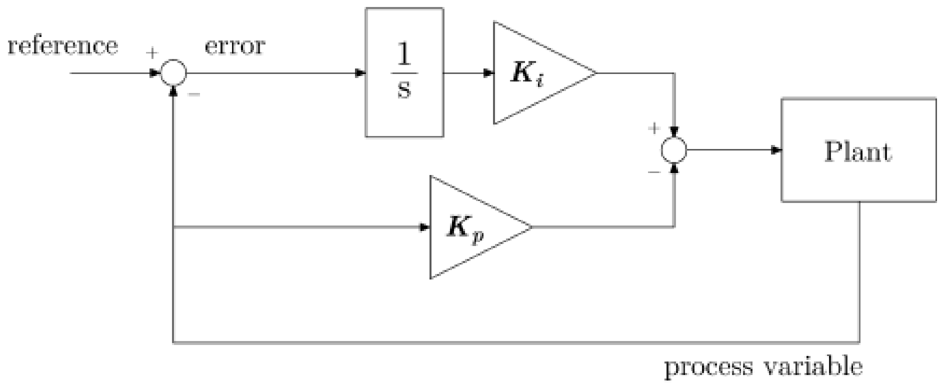

Figure 1.4: Modified PI scheme [1]

The proposed modification consists in removing the contribution of the reference signal from the proportional term. This alteration affects the transfer function that describes the closed-loop system. Based on equation (1.40), the outputs of the PI controller are now given by:

$$\begin{cases} U_d(s) = -K_{p,d} I_d + \dfrac{K_{i,d}}{s}(I_d^* - I_d) \\ U_q(s) = -K_{p,q} I_q + \dfrac{K_{i,q}}{s}(I_q^* - I_q) \end{cases} \tag{1.45}$$

By combining equations (1.38), (1.41), (1.45) with the standard closed-loop transfer function formula $G_t(s) = \frac{G(s)}{1+G(s)H(s)}$, it is possible to obtain:

$$G_{cl}(s) = \frac{\frac{K_i}{L}}{s^2 + \left(\frac{K_p + R}{L}\right) s + \frac{K_i}{L}} \tag{1.46}$$

At this point, looking at the (1.44), it is possible to proceed by comparison and obtain proportional and integral gain:

$$\begin{aligned} K_p &= 2\xi\omega_c L - R_s \\ K_i &= \omega_c^2 L \end{aligned} \tag{1.47}$$

Starting from the closed-loop transfer function with the modified PI controller given in equation (1.46), the poles of the system can be analyzed by examining the roots of the

denominator, which correspond to the values of s that make the denominator zero.
To facilitate this analysis, the following second-order differential equation is introduced. It involves an unknown function $y(x)$, along with its first derivative $y'(x)$ and second derivative $y''(x)$:

$$a(x)y'' + b(x)y' + c(x)y = g(x) \tag{1.48}$$

where $a(x), b(x), c(x)$, and $g(x)$ are known functions defined on an interval $I \subset \mathbb{R}$, with $a(x) \neq 0$ for all $x \in I$. The equation is called *homogeneous* if $g(x) = 0$, and *nonhomogeneous* otherwise.
To simplify the analysis, is possible to consider a nominal operating point where the machine poles are studied, typically corresponding to rated conditions. In this case, the equation becomes simpler because the coefficients a, b, and c are constant, being independent of L and R_s.
The equation (1.48) thus reduces to a homogeneous equation with constant coefficients:

$$ay'' + by' + cy = 0 \tag{1.49}$$

To solve this, is possible to considers the associated *characteristic equation*:

$$as^2 + bs + c = 0 \tag{1.50}$$

To determine the roots of the characteristic equation, the quadratic formula is applied: $s_{1,2} = \frac{-b\pm\sqrt{b^2-4ac}}{2a}$ where the nature of the solution depends on the discriminant $\Delta = b^2 - 4ac$. The roots s_1 and s_2 characterize the dynamic response of the system.
In this case, applying the formulas above requires analyzing the denominator of equation (1.46) and defining the natural frequency by $\omega_n = \sqrt{\frac{K_i}{L}}$, along with the damping ratio given by $\xi = \frac{K_p+R_s}{2\sqrt{LK_i}}$:

$$s^2 + \frac{K_p + R_s}{L}s + \frac{K_i}{L} = s^2 + 2\xi\omega_n s + \omega_n^2 = 0 \tag{1.51}$$

Solving for s, is possible to obtain:

$$s_{1,2} = -\xi\omega_n \pm \omega_n\sqrt{\xi^2 - 1}, \tag{1.52}$$

where the term under the square root corresponds to the discriminant $\Delta = \pm\omega_n\sqrt{\xi^2 - 1}$

Now it is possible to study separately these three possible cases:

- **Overdamped system** ($\xi > 1$, $\Delta > 0$):
  - *Poles*: two distinct real roots at:

$$s_{1,2} = -\xi\omega_n \pm \omega_n\sqrt{\xi^2 - 1} \tag{1.53}$$

    Writing the generic equation:

$$y(x) = C_1 e^{s_1 x} + C_2 e^{s_2 x} \tag{1.54}$$

  - *Response*: each pole defines an exponential decay term with time constant:
    $\tau_1 = 1/|s_1|$: dominates the long-term slow decay;
    $\tau_2 = 1/|s_2|$: governs the initial fast transient.

- **Critically damped system** ($\xi = 1$, $\Delta = 0$):
  - *Poles*: repeated real root with multiplicity 2 at $s_{1,2} = -\omega_n$
    Writing the generic equation:

$$y(x) = (C_1 + C_2 x)e^{sx} \tag{1.55}$$

  - *Response*: oscillatory with fix amplitude

- **Underdamped system** ($0 < \xi < 1$, $\Delta < 0$):
  - *Poles*: complex conjugate $\sigma = \alpha \pm \beta$ at:

$$s_{1,2} = -\xi\omega_n \pm j\omega_n\sqrt{1 - \xi^2} \tag{1.56}$$

    Writing the generic equation:

$$y(x) = e^{\alpha x}\left(C_1 \cos(\beta x) + C_2 \sin(\beta x)\right) \tag{1.57}$$

  - *Response*: oscillatory decay

For reference, the three damping cases discussed earlier are illustrated in the following figures [7]:

(a) Overdamped **(b), (c)** Underdamped **(d)** Critically damped

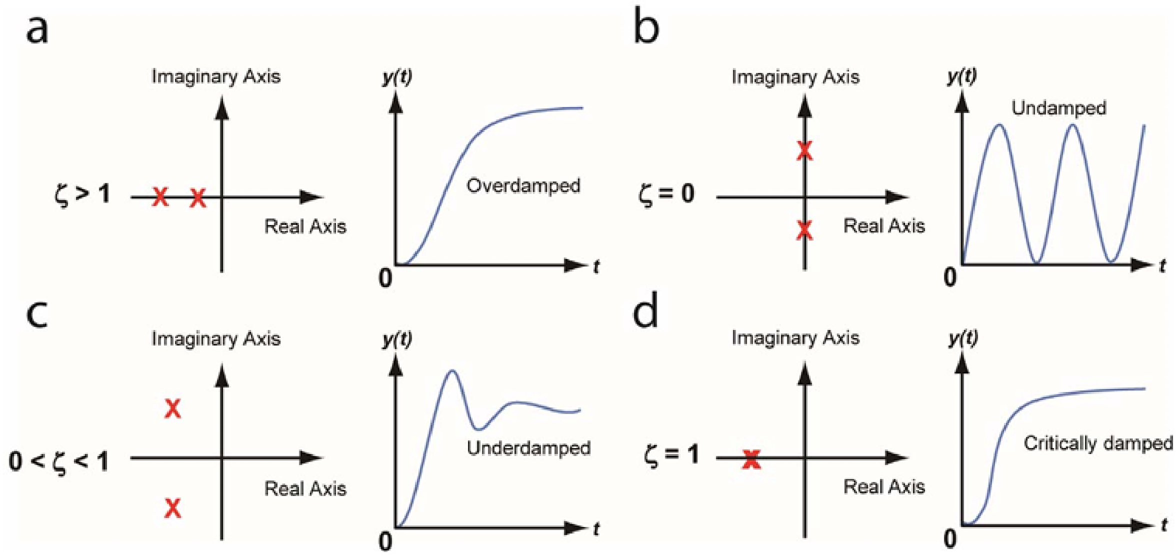

Figure 1.5: Pole position and time response

However, there may be cases where, due to the selected damping factor, control bandwidth, and system parameters, the K_p gain calculation results negative:

$$2\xi\omega_c L - R_s < 0 \Rightarrow \omega_c < \frac{R_s}{2\xi L} \tag{1.58}$$

In such cases, it is preferable to set $K_p = 0$ and re-derive K_i by imposing the desired pole location starting from the equation (1.51):

$$s_{1,2} = \frac{-\frac{R_s}{L} \pm \sqrt{\frac{R_s^2}{L^2} - \frac{4K_i}{L}}}{2} \tag{1.59}$$

Starting from this relationship, it is possible to impose the position at the dominant pole of the closed-loop system. In a transfer function, the dominant pole is the one closest to the imaginary axis. This pole is selected to be real, negative, and equal in magnitude to the desired control bandwidth. It can be shown that the second pole is also real and negative, but located further from the imaginary axis.

$$-\omega_c = \frac{-R_s + \sqrt{R_s^2 - 4LK_i}}{2L} \tag{1.60}$$

The solution for K_i is:

$$K_i = \omega_c R_s - \omega_c^2 L \tag{1.61}$$

In conclusion, the procedure for tuning the gains of PI controllers, assuming the damping factor ξ is one, can be summarised as follows:

$$
\begin{cases}
\text{if } \omega_c < \dfrac{R_s}{L} & \Rightarrow \begin{cases} K_p = 0 \\ K_i = \omega_c R_s - \omega_c^2 L \end{cases} \\
\\
\text{if } \omega_c \geq \dfrac{R_s}{L} & \Rightarrow \begin{cases} K_p = 2\xi\omega_c L - R_s \\ K_i = \omega_c^2 L \end{cases}
\end{cases}
\tag{1.62}
$$

Finally, also the schematic of the current control of a three-phase motor in the d-q reference frame is obtained:

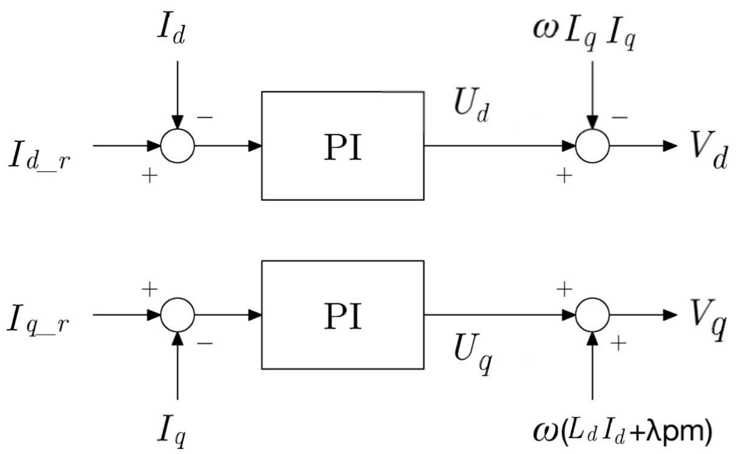

Figure 1.6: Current control

In practical applications, the PI controller does not operate in a truly continuous-time domain. Instead, its behavior is inherently discrete due to the computational requirements and the need for processing time between successive control actions. As a result, while the PI controller is often theoretically modeled as a continuous-time system for simplicity and analytical convenience, its real-world implementation necessitates the inclusion of a delay term to account for the sampling and computation intervals. This delay effectively bridges the gap between the idealized continuous model and the discrete nature of actual control systems.

1.1.3 Speed control

Accurate speed control of a three-phase motor is a fundamental aspect of electric drive systems. This section provides a mathematical foundation for IPM and SPM motor speed control, highlighting its significance and presenting essential dynamic equations.
The electromagnetic torque T_e generated by an IPM motor is expressed as:

$$
T_e = \frac{3}{2} P \left[\varphi_{pm} i_q + (L_d - L_q) i_d i_q \right], \tag{1.63}
$$

For an SPM motor, since $L_d = L_q$, the reluctance torque contribution is negligible.

The mechanical dynamics of the motor are governed by the following equation [6]:

$$T_e - T_L = J\frac{d\omega_m}{dt} + B\omega_m, \tag{1.64}$$

Rewriting in Laplace domain:

$$T_e - T_L = (Js + B)\omega_m, \tag{1.65}$$

From the previous equation is possible to obtain the mechanical transfer function:

$$G_{mec} = \frac{\omega_m}{T_e - T_L} = \frac{1}{Js + B} \tag{1.66}$$

A cascaded control structure is typically employed to regulate correctly the speed of the motor:

1. **Speed control (outer loop):** computes T_e^* based on the speed error;
2. **Current Control (inner loop):** regulates i_d and i_q to realize the desired torque.

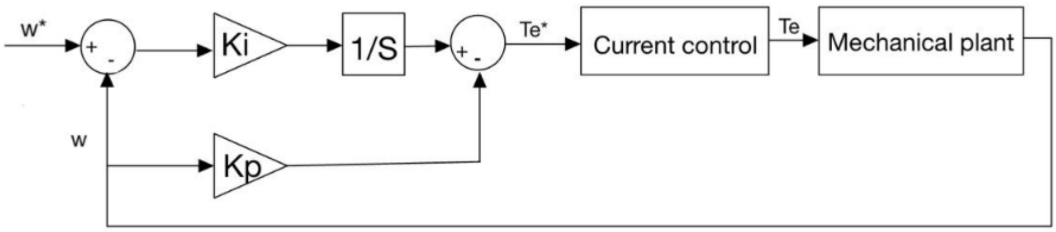

Figure 1.7: Speed and current control

The speed error e_ω is defined as:

$$e_\omega = \omega_m^* - \omega_m, \tag{1.67}$$

A modified PI controller is used to generate the torque reference:

$$T_e^* = -K_p \cdot \omega_m + K_i \int e_\omega \, dt \tag{1.68}$$

Since the current control loop typically operates at a bandwidth approximately ten times higher than that of the speed control loop, it responds significantly faster to changes in the control signal. As a result, the inner current loop can be assumed to track its reference values almost instantaneously relative to the dynamics of the outer speed loop.
This separation of time scales justifies the common control design assumption that the torque, producing current component, and hence the torque reference T_e^* is accurately and promptly achieved. Therefore, for the purpose of speed controller design, the dynamics

of the current loop can be neglected, allowing the torque reference T_e^* to be treated as directly applied to the mechanical system.

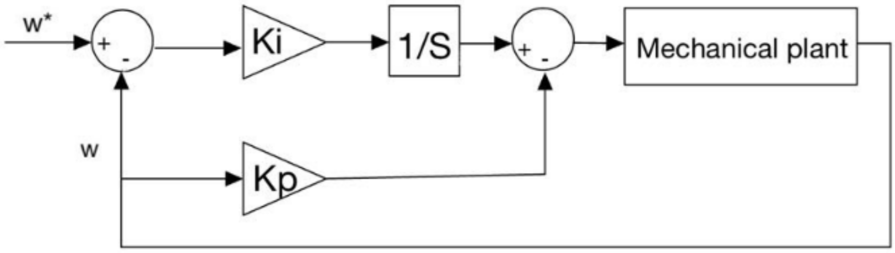

Figure 1.8: Simplify speed control

The closed-loop speed control system can be analyzed using the same approach applied in the current control analysis, but with the equations (1.66) and (1.68). In this context, the load torque T_L is neglected due to the lack of precise information about the external load. Moreover, the PI controller is designed to minimize the speed error over time, effectively compensating for unmodeled disturbances such as T_L.
The transfer function of the speed loop (neglecting load torque) is:

$$G_t = \frac{\omega_m(s)}{\omega_m^*(s)} = \frac{\frac{K_i}{J}}{s^2 + \frac{B+K_p}{J}s + \frac{Ki}{J}} \tag{1.69}$$

In conclusion, the procedure for tuning the gains of PI controllers in accordance with the procedure used in current loop control can be summarized as follows:

$$\begin{cases} \text{if } \omega_c < \dfrac{B}{J} & \Rightarrow \begin{cases} K_p = 0 \\ K_i = \omega_c B - \omega_c^2 J \end{cases} \\ \\ \text{if } \omega_c \geq \dfrac{B}{J} & \Rightarrow \begin{cases} K_p = 2\xi\omega_c J - B \\ K_i = \omega_c^2 J \end{cases} \end{cases} \tag{1.70}$$

The Simulink model incorporates both control strategies: the modified PI controller (Figures 1.7 and 1.8) and the classical PI controller. The classical PI controller, which is also used in the subsequent simulation, is chosen to simplify the tuning process and to provide an alternative approach to the modified structure employed for current control.

To enhance efficiency, the Maximum Torque per Ampere (MTPA) strategy is applied. This method determines the d-axis and q-axis current references that minimize the stator current magnitude for a given torque requirement. The complete control architecture, including the inverter stage, is depicted in the following figure:

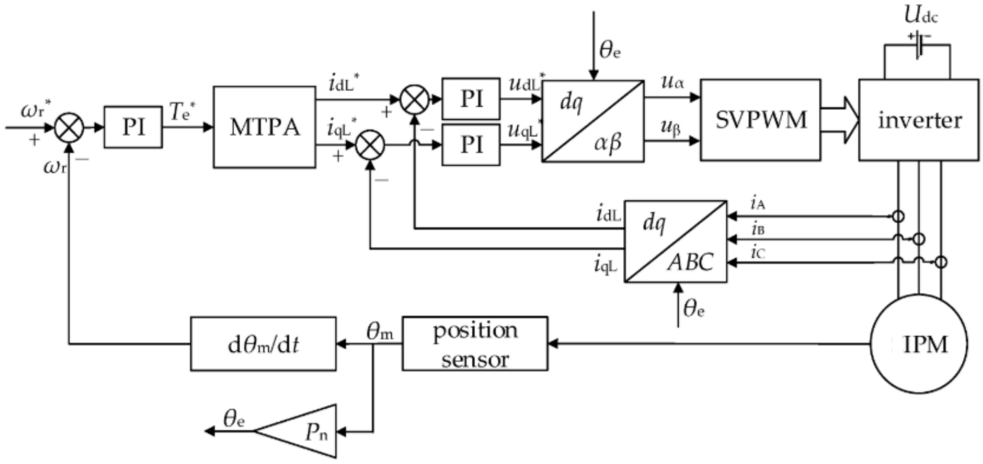

Figure 1.9: Speed and current control without feedforward compensation

1.1.4 Torque Control

Torque control constitutes a critical component in electric systems, enabling precise regulation of a motor's torque output to track a desired reference . This capability is particularly vital in electric vehicles, where the driver requests to the gas pedal a defined torque. The fundamental objective of this control, based on MTPA, is to maximize the torque output for a given magnitude of stator current.

In practical applications, particularly within Simulink environments, MTPA strategies are commonly implemented using look-up tables. This method offers significant advantages in terms of computational efficiency by eliminating the need to solve nonlinear equations in real time.

The implementation process begins with an **offline computation**, where finite element simulations are carried out using FEMM. This phase involves evaluating the motor's electromagnetic behavior for various combinations of direct and quadrature axis currents, i_d and i_q. For simplification, it is assumed that the same current is applied to both sectors of the machine, leading to the following discrete current sets:

$$i_d = i_{d1} = i_{d2} = [-213.75,\ -142.50,\ -71.25,\ -35.625,\ 0,\ 14.25]A$$

$$i_q = i_{q1} = i_{q2} = [-14.25,\ 0,\ 35.625,\ 71.25,\ 142.50,\ 213.75]A$$

Each (i_d, i_q) pair is simulated to determine the corresponding electromagnetic torque with the formulas presented in chapter 2. For each current magnitude, the configuration yielding the maximum torque is identified and stored. This data is then organized into a structured form to create a two-dimensional lookup table, which maps optimal current references to torque values and serves as the basis for real-time control implementation.

Finally, in figure 1.10 are represented the torque and current control of a three-phase motor:

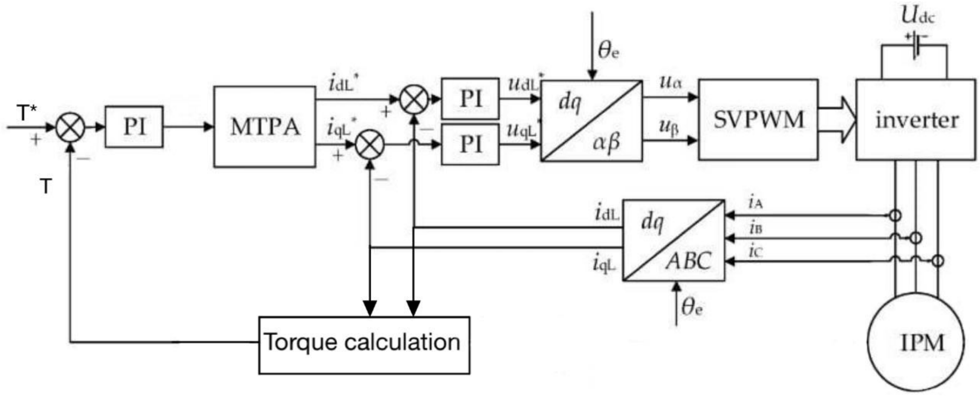

Figure 1.10: Torque and current control without feedforward compensation

The MTPA strategy minimizes the stator current magnitude for a given torque output, thereby reducing Joule losses. However, MTPA does not take into account iron losses, which increase with electrical frequency, or mechanical losses, which rise with rotor speed. Consequently, optimizing the overall drive efficiency requires a more comprehensive approach.

Efficiency maps provide a powerful tool in this context, as they account not only for copper losses but also for iron and mechanical losses. By considering these additional factors, efficiency maps enable more optimization strategies aimed at reducing total energy consumption and improving overall system performance.
These strategies are particularly effective in IPM machines, due to their inherent magnetic saliency ($L_d \neq L_q$). This characteristic enables flexible control over i_d and i_q components, allowing the exploitation of both magnetic and torque contributions for enhanced efficiency. In contrast, SPM machines typically exhibit $L_d \approx L_q$, lacking significant saliency. As a result, they generate little or no reluctance torque and offer a limited possibility for efficiency optimization.

1.2 Overview of multi-three-phase system

The concept of multiphase motor drives can be traced back to 1969, when a five-phase induction motor fed by a voltage source inverter was first proposed [8]. Although initial progress in this domain remained modest throughout the 1970s and 1980s, the 1990s marked a turning point, with a noticeable increase in research activities. This growing interest culminated in widespread global attention during the early 2000s.

The resurgence of interest in multiphase drives has been largely fueled by emerging demands in three technologically intensive application areas: marine propulsion, traction systems for electric and hybrid electric vehicles, and electric aircraft architectures [9]. These sectors present stringent requirements in terms of reliability, efficiency, and fault tolerance, attributes that multiphase machines are inherently better equipped to meet when compared to traditional three-phase solutions [10]. The intrinsic advantages of multiphase systems include enhanced fault handling capabilities, reduced current stress per phase, improved torque quality, and increased power density.

Despite substantial progress in the development of electrical machines and associated drive systems, the adoption of multiphase architectures in real electrified transportation remains relatively limited [9]. This slow integration is primarily due to several technical and economic barriers. Multiphase systems often necessitate more complex inverter topologies, a higher number of power electronic components, and sophisticated control strategies with increased computational requirements. Additionally, the lack of standardized industrial solutions and increased overall system cost further hinders their commercial deployment. Nevertheless, recent years have witnessed a marked resurgence in research activities, with particular emphasis on multi-three-phase machines.

1.2.1 Machine structure

This thesis analyzes two different multi-phase machines SPM and IPM, to understand the differences in both their control strategies and design aspects.

Starting with the SPM motor, it is a synchronous machine that achieves high power density and efficiency through the strategic integration of permanent magnets on the rotor surface. The fundamental operating principle relies on the electromagnetic interaction between the stator's rotating magnetic field and the rotor-mounted permanent magnets. When alternating current energizes the winding of the stator, the resulting rotating magnetic field interacts with the permanent magnets, generating continuous torque through alternating attraction and repulsion of magnetic poles. Electronic commutation precisely controls this interaction, maintaining synchronous operation.

Key advantages of SPM motors include their efficiency, stemming from the absence of rotor copper losses and reduced iron losses. The synchronous operation enables precise speed control across the entire operating range, while the compact design with high-strength

magnets delivers high torque density.
However, SPM motor design presents several engineering challenges. The use of rare-earth permanent magnets introduces material cost volatility and supply chain dependencies. Thermal management becomes critical as high temperatures can lead to partial demagnetization of the permanent magnets. Additionally, the motor exhibits cogging torque, a periodic torque ripple caused by magnetic attraction between rotor magnets and stator teeth.

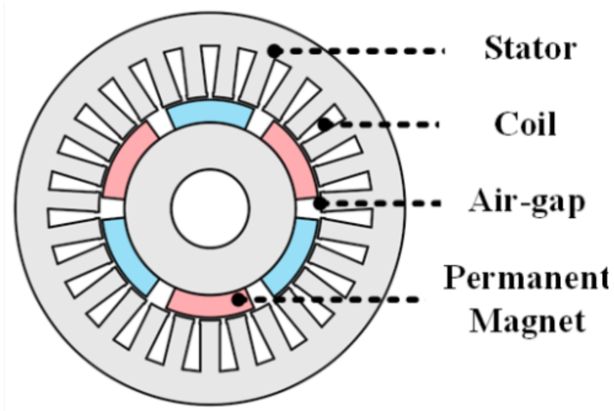

Figure 1.11: Section of a SPM motor [2]

The structure of the dual three-phase IPM motor differs from SPM configurations, offering substantial advantages in torque production. To understand its unique role, it is first necessary to explore its architecture and operating principles. An IPM motor is characterized by the placement of permanent magnets within the rotor's iron core, rather than on the rotor surface. This embedded positioning enables the motor to benefit from what is known as magnetic saliency, a difference in magnetic reluctance along different rotor axes. Saliency provides an additional torque component, called reluctance torque, which complements the torque generated by the permanent magnets. This stands in contrast to the SPM motor, where the magnets are surface-mounted and the rotor typically exhibits no significant saliency, resulting in a torque contribution purely from the magnet interaction with the stator's magnetic field.

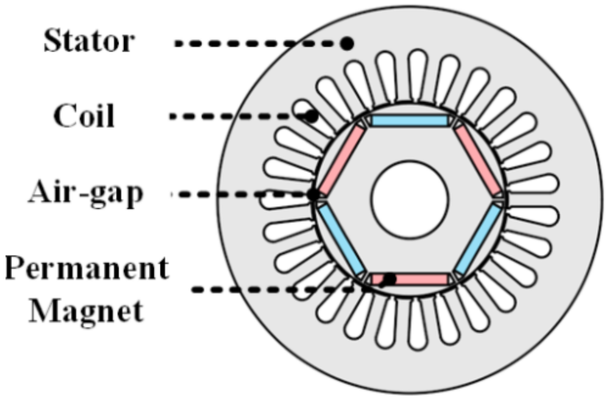

Figure 1.12: Section of an IPM motor [2]

Introducing a dual-three-phase configuration entails a stator with two independent three-phase winding sets. Typically, each winding set is connected to a dedicated power inverter, allowing for independent control. This arrangement introduces both increased design flexibility and fault tolerance. If one inverter or phase set fails, the motor may continue to operate using the remaining healthy set.
Multiphase machines can generally be categorized into two main configurations according to the winding layout:

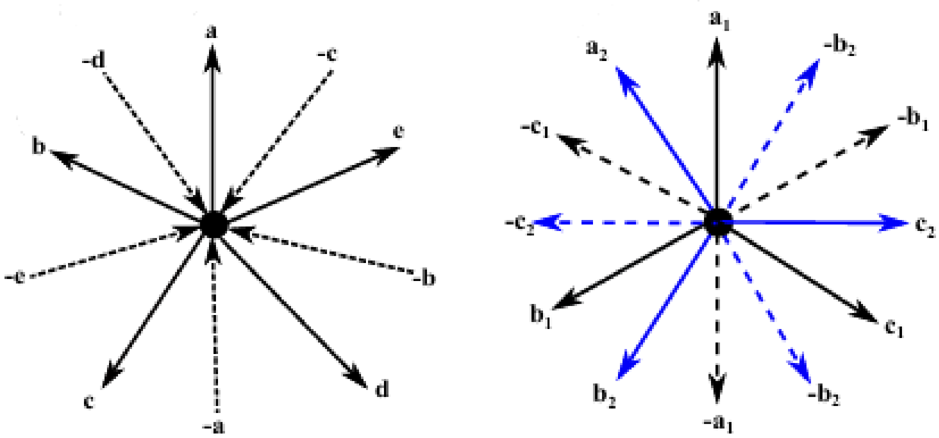

Figure 1.13: Possible winding configuration

The figure illustrates two distinct winding configurations: on the left, the multiple single-phase windings, and on the right, the multiple independent three-phase windings.The first configuration, which typically features symmetric phase distributions, involves several single-phase windings that are spatially separated and connected in a manner that ensures balanced operation. The second configuration is composed of multiple, independent sets of three-phase windings.
The choice between these configurations depends largely on the specific application requirements, such as desired fault tolerance, power density, and overall system complexity.

This thesis focuses on the second configuration.

Within the domain of multi-three-phase machine winding arrangements, two principal topologies are discernible: asymmetrical and symmetrical. Although both configurations have unique characteristics, research often focuses on the asymmetrical design: a network of star-connected three-phase stator windings, each spatially displaced and featuring electrically isolated neutral points.
The following image shows the motor under study, featuring an asymmetric winding configuration with a 30° phase shift:

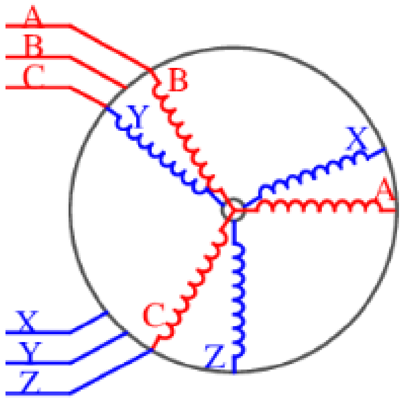

Figure 1.14: Phase shift of 30°

In Fig. 1.14 ABC is used to indicate the first segment and XYZ the second one

1.2.2 Power electronics

To enable active control, multi-three-phase machines require a dedicated drive system. In traditional electric drive architectures, a standard three-phase motor is typically powered by a two-level or three-level voltage source inverter. The more easy two-level inverter employs a bridge configuration with six switching devices arranged in three legs, controlled through duty cycle modulation techniques. When adapting this setup for multi-three-phase machines, each independent three-phase winding set is usually driven by its own conventional three-phase inverter.

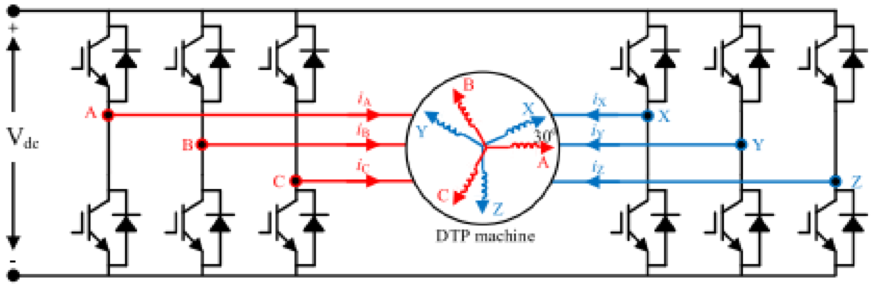

Figure 1.15: Asymmetrical dual-three-phase drive system [3]

When considering the adoption of a two-level inverter feeding a dual-three-phase motor topology rather than a conventional three-phase motor of identical power rating, several benefits become evident. First, the distribution of current among six phases instead of three reduces the RMS current per phase for the same total output power. This reduction in phase current leads to lower conduction losses in both the motor windings and the inverter devices, which can translate into higher overall efficiency.
Another significant benefit arises from the improved smoother electromagnetic torque production. In a dual-three-phase arrangement, the phase sets are spatially shifted, and by driving them appropriately through a two-level inverter, the aggregate phase voltage waveform seen by the airgap can exhibit lower harmonic content compared to a three-phase system at equal switching frequency.
Fault tolerance is also enhanced in a six-phase implementation. In the event of an open-circuit or short-circuit fault in one phase winding or its corresponding power switch leg, it is often possible to continue operating with reduced but acceptable performance by suitably reconfiguring the drive signals among the remaining healthy phases. This inherent redundancy is not available in a standard three-phase machine.
From a modulation perspective, implementing carrier-based PWM on a six-phase machine using a two-level converter allows for the exploitation of a significantly larger vector space expanding from $2^3 = 8$ vectors in a three-phase system to $2^6 = 64$ in a dual three-phase configuration. This increased number of available switching states enhances the system's DOF, enabling operation closer to the DC bus voltage limit. As a result, a slightly higher maximum amplitude of the fundamental voltage can be achieved.

1.2.3 PWM generation

1. Ideal case

In the ideal case of PWM generation, the modulation signal is continuously compared to a triangular carrier signal. The resulting PWM waveform transitions precisely at the points where the modulation and carrier signals intersect. When the carrier signal has a higher value than the modulation signal, the PWM output is low; conversely, when the modulation signal exceeds the carrier, the PWM output is high.

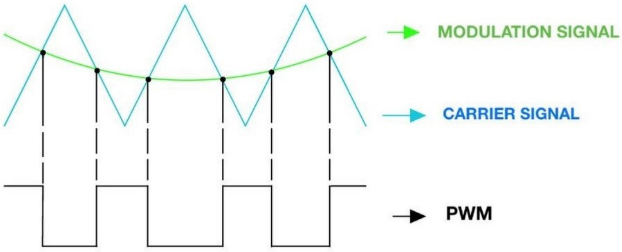

Parameter	Value
Sampling frequency	∞
Sampling	Continuous

Figure 1.16: Ideal PWM generation

This method provides the highest fidelity, but is not realizable in practical digital systems due to the need for infinite sampling resolution.
Another important parameter for the generation of the PWM is the modulation index, denoted as m, and defined as:

$$m_i = \frac{v_{\text{mod,pk}}}{v_{\text{c,pk}}} \tag{1.71}$$

The modulation index determines the characteristics of the output waveform and can be categorized as follows:

- **Linear region** ($0 \leq m \leq 1$): in this range, the AC output voltage varies linearly with the modulation index. The resulting harmonic components are well-defined, which makes filtering straightforward;
- **Overmodulation region** ($m > 1$): when the modulation index exceeds unity, harmonics emerge in the AC output voltage. This results in spectral components at lower frequencies, complicating the filter design and potentially degrading waveform quality.

2. Single sampling

In this approach, the modulation signal is sampled only once per carrier cycle, typically at either the peak or the valley of the triangular waveform. The sampled value is held constant for the duration of the switching period, resulting in a PWM output based on discrete modulation levels.

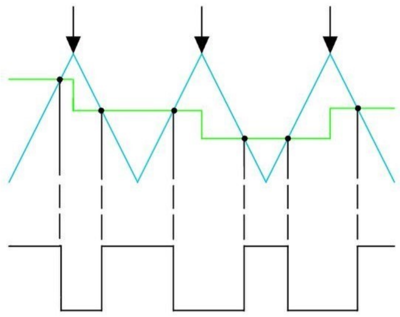

Parameter	Value
Sampling frequency:	$f_{\text{sample}} = f_{\text{sw}}$
Sampling	Discrete

Figure 1.17: Single sampling

3. Double sampling

Double sampling enhances single sampling by capturing the modulation signal twice during each carrier period, typically at both the peak and the valley of the triangular waveform. This allows for better tracking of the modulation signal and results in improved accuracy of the PWM waveform.

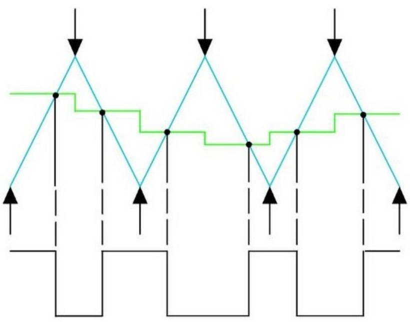

Parameter	Value
Sampling frequency:	$f_{\text{sample}} = 2 \cdot f_{\text{sw}}$
Sampling	Discrete

Figure 1.18: Double sampling

In the Simulink simulation, it is possible to select either the ideal case or the double sampling configuration in order to evaluate the differences between the ideal and practical implementations.

Chapter 2

Dual-three-phase machines

2.1 Machine equations

Building upon the three-phase machine equations derived in section 1.33, the same mathematical structure can be extended to a dual-three-phase machine. For conciseness, the full derivation is not repeated here, as the previous analysis applies analogously to both segments of the machine. Thus, the resulting equations remain consistent, leading to the final expression:

$$\underbrace{\begin{bmatrix} v_{d_a} \\ v_{q_a} \\ v_{d_b} \\ v_{q_b} \end{bmatrix}}_{\bar{v}} = \underbrace{R_s \cdot I_4}_{\mathbf{R}} \underbrace{\begin{bmatrix} i_{d_a} \\ i_{q_a} \\ i_{d_b} \\ i_{q_b} \end{bmatrix}}_{\bar{i}} + \underbrace{\frac{d}{dt}\begin{bmatrix} \varphi_{d_a} \\ \varphi_{q_a} \\ \varphi_{d_b} \\ \varphi_{q_b} \end{bmatrix}}_{\frac{d\bar{\varphi}}{dt}} + \omega \underbrace{\begin{bmatrix} 0 & -1 & 0 & 0 \\ 1 & 0 & 0 & 0 \\ 0 & 0 & 0 & -1 \\ 0 & 0 & 1 & 0 \end{bmatrix}}_{\mathbf{T}} \underbrace{\begin{bmatrix} \varphi_{d_a} \\ \varphi_{q_a} \\ \varphi_{d_b} \\ \varphi_{q_b} \end{bmatrix}}_{\bar{\varphi}} \tag{2.1}$$

Where the fluxes are defined as follows:

$$\underbrace{\begin{bmatrix} \varphi_{d_a} \\ \varphi_{q_a} \\ \varphi_{d_b} \\ \varphi_{q_b} \end{bmatrix}}_{\bar{\varphi}} = \underbrace{\begin{bmatrix} L_{da} & L_{daq_a} & L_{dad_b} & L_{daq_b} \\ L_{q_a d_a} & L_{q_a} & L_{q_a d_b} & L_{q_a q_b} \\ L_{d_b d_a} & L_{d_b q_a} & L_{d_b} & L_{d_b q_b} \\ L_{q_b d_a} & L_{q_b q_a} & L_{q_b d_b} & L_{q_b} \end{bmatrix}}_{\mathbf{L_{dq}}} \underbrace{\begin{bmatrix} i_{d_a} \\ i_{q_a} \\ i_{d_b} \\ i_{q_b} \end{bmatrix}}_{\bar{i}} + \underbrace{\begin{bmatrix} \varphi_{pm,a} \\ 0 \\ \varphi_{pm,b} \\ 0 \end{bmatrix}}_{\bar{\varphi}_{pm}} \tag{2.2}$$

Making the derivative calculation:

$$\frac{d\bar{\varphi}(i, \theta, T_{\text{mag}})}{dt} = \frac{d\bar{\varphi}}{d\bar{i}} \cdot \frac{d\bar{i}}{dt} + \frac{d\bar{\varphi}}{d\theta} \cdot \frac{d\theta}{dt} + \frac{d\bar{\varphi}}{dT_{\text{mag}}} \cdot \frac{dT_{\text{mag}}}{dt} \tag{2.3}$$

Where is possible to rewrite some terms as follows:

$$\frac{d\bar{\varphi}}{d\bar{i}} = \frac{d(\mathbf{L_{dq}} \cdot \bar{i} + \bar{\varphi}_{pm})}{di} = \frac{d(\mathbf{L_{dq}})}{d\bar{i}}\bar{i} + \mathbf{L_{dq}}$$
$$\frac{d\theta}{dt} = \omega \tag{2.4}$$

From the equation (2.3), it can be observed that the time derivative of the flux is dependent on both the rotor angular position and the magnet temperature. The rotor angular position affects the flux distribution due to the saliency of the rotor structure, leading to variations in the direct and quadrature inductances. Additionally, the temperature of the permanent magnets significantly impacts their remanent flux density, thereby altering the overall flux linkage. As the magnet temperature increases, the remanence decreases, leading to a reduction in the electromotive force and a modification in the machine's electromagnetic torque production, as possible to notice in figure 2.1.

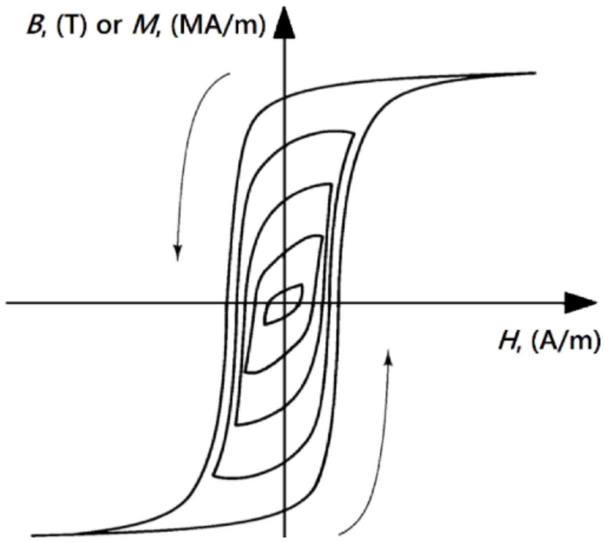

Figure 2.1: BH curve of the permanent magnet as a function of temperature [4]

This temperature dependence introduces additional complexity in the dynamic modeling and control of the machine, particularly in the estimation of temperature-dependent parameters. As the temperature increases, the B–H characteristic of the magnetic material leads to a reduction in the size of the magnetic hysteresis loop.

In this thesis, the system is assumed to operate under steady-state conditions, implying that the temperature remains constant over time. To further simplify the analysis, the magnetic flux is also assumed to be time invariant. This simplification is more challenging in IPM machines, whereas it is less significant in SPM machines. This is achieved by considering the mean values over a full electrical cycle of 360°.

Rewriting equation (2.1) in a more compact form:

$$\bar{v} = \mathbf{R}\,\bar{i} + \frac{d\bar{\boldsymbol{\varphi}}}{dt} + \omega\,\mathbf{T}\bar{\boldsymbol{\varphi}} \tag{2.5}$$

Combining equation (2.4) with equations (2.5):

$$\bar{v} = \mathbf{R} \cdot \bar{i} + \frac{d\bar{\boldsymbol{\varphi}}}{d\bar{i}}\frac{d\bar{i}}{dt} + \frac{d\bar{\varphi}}{d\theta}\omega + \omega\,\mathbf{T}\bar{\varphi} \tag{2.6}$$

Neglecting the temperature contribution and substituting the fluxes equation (2.4):

$$\bar{v} = \mathbf{R} \cdot \bar{i} + \left(\frac{d}{d\bar{i}}\mathbf{L_{dq}}d\bar{i} + \mathbf{L_{dq}}\right)\frac{d\bar{i}}{dt} + \frac{d\bar{\varphi}}{d\theta}\omega + \omega\,\mathbf{T}\left(\mathbf{L_{dq}}\bar{i} + \bar{\varphi}_{pm}\right) \tag{2.7}$$

Where is it possible to define the differential inductances $\mathbf{dL_{dq}}$ as:

$$\frac{d\bar{\varphi}}{d\bar{i}} = \mathbf{dL_{dq}} = \frac{d}{d\bar{i}}\mathbf{L_{dq}}d\bar{i} + \mathbf{L_{dq}} \tag{2.8}$$

The final equation results:

$$\bar{v} = \mathbf{R} \cdot \bar{i} + \mathbf{dL_{dq}}\frac{d\bar{i}}{dt} + \frac{d(\mathbf{L_{dq}}\bar{\mathbf{i}} + \bar{\varphi}_{pm})}{d\theta}\omega + \omega\,\mathbf{T}\left(\mathbf{L_{dq}}\bar{i} + \bar{\varphi}_{pm}\right) \tag{2.9}$$

In the modeling of a dual-three-phase machine, the dependence of both $\mathbf{L}_{dq}(\theta)$ and $\bar{\varphi}_{pm}(\theta)$ on the rotor position θ introduces significant complexity in the design of the control system. To solve this problem, these quantities are averaged over θ, making it reasonable to approximate them by their mean values. The real graphical visualization of all the inductances as a function of the angular position is given in the simulation chapter, and in particular in figure 5.23.
Finally, it is possible to rewrite the formula (2.9):

$$\bar{\mathbf{v}} = \mathbf{R} \cdot \bar{i} + \mathbf{dL_{dq}}\frac{d\bar{i}}{dt} + \omega\,\mathbf{T}\left(\mathbf{L_{dq}}\bar{i} + \bar{\varphi}_{pm}\right) \tag{2.10}$$

As can be seen in the simplified equation (2.10), the voltage is a function of $\mathbf{L_{dq}}$ and $\mathbf{dL_{dq}}$, then in the following is described the process for obtaining these values.
The development of the FEMM model required careful consideration of magnetic nonlinearities, making the principle of superposition inapplicable for this analysis. This nonlinear behavior significantly influences the machine's characteristics, particularly under saturated operating conditions. The software enables to capture of these interactions by directly solving the field equations while accounting for the material's nonlinear permeability, allowing for accurate prediction of flux density distributions and local saturation effects throughout the magnetic circuit.

Flux determination

The subsequent objective is to derive an expression for magnetic flux between two current-carrying surfaces, utilizing the magnetic vector potential formulation.

The magnetic vector potential $\bar{A}$ is defined in accordance with article [11]:

$$\bar{A}(\bar{r}) = \frac{\mu_0}{4\pi} \int \frac{\bar{J}(\bar{r}')}{|\bar{r} - \bar{r}'|} \, dV' \tag{2.11}$$

In the case of surface currents distributed over a surface S, is replaced the volume current density with the surface current density $\bar{K}$ [11]:

$$\bar{A}(\bar{r}) = \frac{\mu_0}{4\pi} \int_S \frac{\bar{K}(\bar{r}')}{|\bar{r} - \bar{r}'|} \, dS' \tag{2.12}$$

Now consider two surfaces, S_1 and S_2, with surface current densities $\bar{K}_1$ and $\bar{K}_2$. The magnetic vector potential at a point $\bar{r}_1 \in S_1$ due to currents on S_2 is:

$$\bar{A}(\bar{r}_1) = \frac{\mu_0}{4\pi} \int_{S_2} \frac{\bar{K}_2(\bar{r}_2)}{|\bar{r}_1 - \bar{r}_2|} \, dS_2 \tag{2.13}$$

The magnetic energy stored in the system can be represented either as a volume integral over the current density or, equivalently, as a surface integral over the surface current density, as discussed in [12]:

$$\varphi = \frac{1}{2} \int \bar{J} \cdot \bar{A} \, dV \quad \text{or} \quad \varphi = \frac{1}{2} \int_S \bar{K} \cdot \bar{A} \, dS \tag{2.14}$$

The linked flux resulting from the interaction between the two current distributions is:

$$\varphi = \int_{S_1} \bar{K}_1(\bar{r}_1) \cdot \bar{A}(\bar{r}_1) \, dS_1 \tag{2.15}$$

Substituting the expression (2.13) into (2.15):

$$\varphi = \frac{\mu_0}{4\pi} \int_{S_1} \int_{S_2} \frac{\bar{K}_1(\bar{r}_1) \cdot \bar{K}_2(\bar{r}_2)}{|\bar{r}_1 - \bar{r}_2|} \, dS_2 \, dS_1 \tag{2.16}$$

Assuming both currents are oriented along the z-axis, i.e., $\bar{K}_1 = K_1\hat{z}$ and $\bar{K}_2 = K_2\hat{z}$, the dot product simplifies:

$$\bar{K}_1 \cdot \bar{K}_2 = K_1 K_2 \tag{2.17}$$

So the linked flux becomes:

$$\varphi = \int_{S_1} K_1(\bar{r}_1) A_z(\bar{r}_1) \, dS_1 = \frac{\mu_0}{4\pi|\bar{r}_1 - \bar{r}_2|} \int_{S_1} \int_{S_2} K_1(\bar{r}_1) K_2(\bar{r}_2) \, dS_2 dS_1 \tag{2.18}$$

Where is it possible to define the constant terms, before the double integral, as:

$$L_A = \frac{\mu_0}{4\pi} \frac{1}{|\bar{r}_1 - \bar{r}_2|} \tag{2.19}$$

In a post-processing step, it is possible to obtain two other important quantities that are later used for machine control and modeling:

- Apparent inductances:

$$\mathbf{L_{dq}} = \begin{bmatrix} L_{da} & M_{daqa} & M_{dadb} & M_{daqb} \\ M_{qada} & L_{qa} & M_{qadb} & M_{qaqb} \\ M_{dbda} & M_{dbqa} & L_{db} & M_{dbqb} \\ M_{qbda} & M_{qbqa} & M_{qbdb} & L_{qb} \end{bmatrix} \tag{2.20}$$

  Each element of the inductance matrix $\mathbf{L}_{dq}$ can be expressed using a general formula:

$$L_{diqj} = \frac{\varphi_i(\bar{p}_1) - \varphi_i(\bar{p}_2)}{\bar{i}_j} \tag{2.21}$$

  Where:

$$\bar{p} = \left[i_{da}, i_{qa}, i_{db}, i_{qb}, \theta_e \right] \tag{2.22}$$

  Each current component may take either zero or its value, depending on the inductances considered.

- Incremental inductances:

$$\mathbf{dL_{dq}} = \begin{bmatrix} dL_{da} & dM_{daq_a} & dM_{dadb} & dM_{daq_b} \\ dM_{q_ada} & dL_{q_a} & dM_{qadb} & dM_{q_aq_b} \\ dM_{dbda} & dM_{dbq_a} & dL_{d_b} & dM_{dbq_b} \\ dM_{q_bda} & dM_{q_bq_a} & dM_{q_bd_b} & dL_{q_b} \end{bmatrix} \tag{2.23}$$

  Where each value is obtained with the following formulas:

$$\mathbf{dL_{dq}} = \begin{bmatrix} \frac{d\varphi_{dA}}{di_{dA}} & \frac{d\varphi_{dA}}{di_{qA}} & \frac{d\varphi_{dA}}{di_{dB}} & \frac{d\varphi_{dA}}{di_{qB}} \\ \frac{d\varphi_{qA}}{di_{dA}} & \frac{d\varphi_{qA}}{di_{qA}} & \frac{d\varphi_{qA}}{di_{dB}} & \frac{d\varphi_{qA}}{di_{qB}} \\ \frac{d\varphi_{dB}}{di_{dA}} & \frac{d\varphi_{dB}}{di_{qA}} & \frac{d\varphi_{dB}}{di_{dB}} & \frac{d\varphi_{dB}}{di_{qB}} \\ \frac{d\varphi_{qB}}{di_{dA}} & \frac{d\varphi_{qB}}{di_{qA}} & \frac{d\varphi_{qB}}{di_{dB}} & \frac{d\varphi_{qB}}{di_{qB}} \end{bmatrix} \tag{2.24}$$

Torque and force computation

The Maxwell stress tensor approach calculates torque and radial forces, leveraging FEMM's integrated force calculation capabilities. Consider the Maxwell stress tensor in magnetostatics, defined as:

$$\sigma_{ij} = \frac{1}{\mu_0}\left(B_i B_j - \frac{1}{2}\delta_{ij}\bar{B}^2\right), \tag{2.25}$$

where $\bar{B} = (B_x, B_y, B_z)$ is the magnetic flux density

The traction force per unit area on a surface with outward unit normal vector $\bar{n} = (n_x, n_y, n_z)$ is:

$$f_i = \sigma_{ij} \cdot n_j = \frac{1}{\mu_0}\left(B_i(\bar{B} \cdot \bar{n}) - \frac{1}{2}B^2 n_i\right) \tag{2.26}$$

The electromagnetic torque τ_z about the z-axis exerted on a body enclosed by surface S is:

$$\tau_z = \oint_S \left(\bar{r} \times (\boldsymbol{\sigma} \cdot \bar{n})\right)_z \, dS \tag{2.27}$$

where $\bar{r} = (x, y, z)$ is the position vector.

Expanding the z-component of the cross product yields:

$$\tau_z = \oint_S (x f_y - y f_x) \, dS \tag{2.28}$$

Considering a cylindrical surface C of radius R_{rc} centered on the z-axis, the outward normal vector is radial:

$$n_x = \cos(\theta), \quad n_y = \sin(\theta), \quad x = R_{rc} \cdot n_x, \quad y = R_{rc} \cdot n_y \tag{2.29}$$

Considering the $x f_y - y f_x$ inside (2.28):

$$\begin{aligned} x f_y - y f_x &= \frac{1}{\mu_0}\left[x B_y(\bar{B} \cdot \bar{n}) - \frac{1}{2}x B^2 n_y - y B_x(\bar{B} \cdot \bar{n}) + \frac{1}{2}y \bar{B}^2 n_x\right] \\ &= \frac{R_{rc}}{\mu_0}\left[B_r B_t + \frac{\bar{B}^2}{2}(n_y n_x - n_x n_y)\right] = \frac{R_{rc}}{\mu_0} B_r B_t \end{aligned} \tag{2.30}$$

where $B_r = \bar{B} \cdot \bar{n} = B_x n_x + B_y n_y$ is the radial component and $B_t = B_y n_x - B_x n_y$ is the tangential component of the magnetic flux density at the surface. The terms proportional to $\bar{B}^2$ cancel due to the antisymmetric factor.

Therefore, the torque reduces to:

$$\tau_z = \oint_C (x f_y - y f_x) dS = \frac{R_{rc}}{\mu_0} \oint_C B_r B_t \, dS. \tag{2.31}$$

Expressing the integrand in cartesian components, the torque integrand becomes:

$$T_z = \oint_C R_{rc} \left(B_x B_y n_y - B_y B_x n_x\right) dS \tag{2.32}$$

2.1.1 Comparison IPM and SPM

The existing body of literature in the field of permanent magnet synchronous machines reveals a significant disparity in research focus. A substantial portion of the published works predominantly addresses the design methodologies and control strategies applicable to SPM machines. This emphasis is likely attributed to the relative simplicity in their magnetic circuit analysis and control implementation, coupled with their well-established industrial adoption.

Torque comparison

The embedded placement of permanent magnets within the rotor core of IPM machines results in a saliency effect characterized $L_d \neq L_q$. This magnetic anisotropy provides an additional torque component, known as reluctance torque, which can significantly enhance the overall torque capability and power density of the machine. From a torque production perspective, the advantage of the IPM design becomes particularly clear. For a single three-phase IPM motor, the electromagnetic torque is expressed (1.63) where the term $(L_d - L_q)i_d i_q$, accounts for the reluctance torque. In a SPM motor this terms is zero, since $L_d = L_q$.

However, in the dual three-phase IPM motor, is important to consider that there are two independent three-phase systems contributing to the total electromagnetic torque. Assuming both stator winding sets are symmetrically loaded and identical in electrical characteristics, the total torque can be modeled as the sum of the torques produced by each subsystem:

$$T_{\text{total}} = T_1 + T_2 = 3p\left((L_d - L_q)i_d i_q + \varphi_{pm} i_q\right) \tag{2.33}$$

This clearly shows that, all else being equal, the dual three-phase configuration offers twice the torque-producing capability of a single three-phase IPM machine—assuming. The dual winding system allows not only for higher peak torque but also improved continuous operation by spreading thermal and electrical stress across a larger area.

Voltage and current limit

It is important to note that the voltage and current limitations are not identical for the two motors. Each motor operates within its own set of electrical constraints, which define the permissible ranges for voltage and current during operation. These limitations directly affect the performance envelope of each machine. Figure 2.2 illustrates the electrical characteristics of both synchronous machines, highlighting their respective current and voltage boundaries.

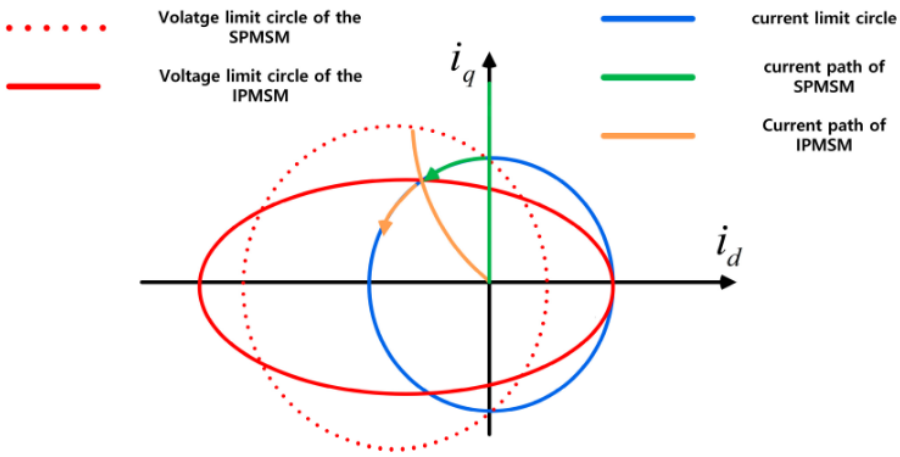

Figure 2.2: Current locus diagram [2]

In this context, the maximum voltage and current that the inverter can supply to the three-phase motor are given by the following expressions. A similar analysis can be extended to the dual three-phase configuration.

$$i^{\max} = \sqrt{i_d^2 + i_q^2} \tag{2.34}$$

$$V_{\text{max, SPM}} = \omega_m \sqrt{\varphi_{pm}^2 + (L_s i_q)^2} \tag{2.35}$$

$$V_{\text{max, IPM}} = \omega_m \sqrt{(L_d i_d + \varphi_{pm})^2 + (L_q i_q)^2} \tag{2.36}$$

During operation, the motor reaches its peak torque output at the point where current and voltage constraints intersect in the i_d-i_q plane, as described by the current locus. For SPM, this in theory occurs under an $i_d = 0$ control strategy, utilizing purely magnet torque. In contrast, IPM exploit a negative i_d current to generate additional reluctance torque, thereby increasing the total torque output.
As the machine accelerates into higher-speed regions beyond the MTPA operating point, voltage constraints become dominant. This necessitates operation in the field-weakening region, where a further negative i_d current is applied to counteract the increasing EMF, thereby allowing sustained operation beyond the base speed.

2.2 Control strategies

Following the comprehensive analysis of current, speed, and torque control in a conventional three-phase machine, where all fundamental control equations were derived, this chapter extends the discussion to a dual-three-phase machine system. Compared to the three-phase machine, the mathematical model of a dual three-phase machine exhibits increased

complexity, particularly in the formulation of the machine equations.
As is possible to see in (2.1), the equation employs separate dq reference frames, with one frame aligned to the first three-phase sector and another to the second sector. This decoupled control approach enables independent regulation of each winding set.
The control architecture is composed of four PI controllers, organized as follows:

- Two controllers for sector a, regulating the d_a and q_a axes
- Two controllers for sector b, regulating the d_b and q_b axes

2.2.1 Modular approach

For control tuning purposes, it is essential to express the simplified machine equations in their expanded form. Starting from the compact representation given in (2.10), the following expression can be derived:

$$\underbrace{\begin{bmatrix} v_{da} \\ v_{qa} \\ v_{db} \\ v_{qb} \end{bmatrix} = \mathbf{R} \begin{bmatrix} i_{da} \\ i_{qa} \\ i_{db} \\ i_{qb} \end{bmatrix} + \begin{bmatrix} dL_{da} & dM_{daqa} & dM_{dadb} & dM_{daqb} \\ dM_{qada} & dL_{qa} & dM_{qadb} & dM_{qaqb} \\ dM_{dbda} & dM_{dbqa} & dL_{db} & dM_{dbqb} \\ dM_{qbda} & dM_{qbqa} & dM_{qbdb} & dL_{qb} \end{bmatrix} \begin{bmatrix} di_{da} \\ di_{qa} \\ di_{db} \\ di_{qb} \end{bmatrix}}_{\text{PI}} +$$
$$\underbrace{\omega \begin{bmatrix} 0 & -1 & 0 & 0 \\ 1 & 0 & 0 & 0 \\ 0 & 0 & 0 & -1 \\ 0 & 0 & 1 & 0 \end{bmatrix} \left(\begin{bmatrix} L_{da} & M_{daqa} & M_{dadb} & M_{daqb} \\ M_{qada} & L_{qa} & M_{qadb} & M_{qaqb} \\ M_{dbda} & M_{dbqa} & L_{db} & M_{dbqb} \\ M_{qbda} & M_{qbqa} & M_{qbdb} & L_{qb} \end{bmatrix} \begin{bmatrix} i_{da} \\ i_{qa} \\ i_{db} \\ i_{qb} \end{bmatrix} + \begin{bmatrix} \varphi_{pm,a} \\ 0 \\ \varphi_{pm,b} \\ 0 \end{bmatrix} \right)}_{\text{Feedforward compensation}} \tag{2.37}$$

At this stage, the apparent and incremental inductance matrices are assumed to be constant. To enforce this assumption, the currents i_d and i_q in both operational sectors are fixed to their previously determined rated values, and an average over the electrical angle θ is computed.
Writing only the terms that are necessary for the tuning of the PI:

$$\begin{cases} v_{da} = R_s i_{da} + dL_{da} \frac{di_{da}}{dt} + dM_{daqa} \frac{di_{qa}}{dt} + dM_{dab} \frac{di_{d_b}}{dt} + dM_{daq_b} \frac{di_{qb}}{dt} \\ v_{qa} = R_s i_{qa} + dM_{qada} \frac{di_{da}}{dt} + dL_{qa} \frac{di_{qa}}{dt} + dM_{qab} \frac{di_{d_b}}{dt} + dM_{qaq_b} \frac{di_{qb}}{dt} \\ v_{db} = R_s i_{db} + dM_{dbda} \frac{di_{da}}{dt} + dM_{dbqa} \frac{di_{qa}}{dt} + dL_{db} \frac{di_{db}}{dt} + dM_{dbqb} \frac{di_{qb}}{dt} \\ v_{qb} = R_s i_{qb} + dM_{qbda} \frac{di_{da}}{dt} + dM_{qbqa} \frac{di_{qa}}{dt} + dM_{qbdb} \frac{di_{db}}{dt} + dL_{qb} \frac{di_{qb}}{dt} \end{cases} \tag{2.38}$$

Since it is necessary to obtain a mathematical formulation comparable to that studied for the three-phase motor in section 1.41, developing the machine's equations in a form that allows certain terms to be neglected is useful.

The first approach is to simplify the mutual terms directly form (2.38):

$$\begin{cases} v_{da} = R_s i_{da} + dL_{da} \frac{di_{da}}{dt} \\ v_{qa} = R_s i_{qa} + dL_{qa} \frac{di_{qa}}{dt} \\ v_{db} = R_s i_{db} + dL_{db} \frac{di_{db}}{dt} \\ v_{qb} = R_s i_{qb} + dL_{qb} \frac{di_{qb}}{dt} \end{cases} \tag{2.39}$$

The second approach, since the motor is modeled in Simulink with a voltage source as the input and current as the output, the governing equations can be expressed compactly as:

$$d\bar{i} = \mathbf{dL_{dq}}^{-1} \left(\bar{v} - \mathbf{R}\bar{i} \right) \tag{2.40}$$

Where for simplicity $\mathbf{dL_{dq}}$ is expressed in the following way:

$$\mathbf{dL_{dq}}^{-1} = \boldsymbol{\alpha_{dq}} = \begin{bmatrix} \alpha_{da} & \alpha_{daqa} & \alpha_{dadb} & \alpha_{daqb} \\ \alpha_{qada} & \alpha_{qa} & \alpha_{qadb} & \alpha_{qaqb} \\ \alpha_{dbda} & \alpha_{dbqa} & \alpha_{db} & \alpha_{dbqb} \\ \alpha_{qbda} & \alpha_{qbqa} & \alpha_{qbdb} & \alpha_{qb} \end{bmatrix} \tag{2.41}$$

Due to the properties of matrix inversion, all mutual inductance terms are inherently coupled in this operation:

$$\mathbf{dL_{dq}}^{-1} = \frac{\mathrm{adj}(\mathbf{dL_{dq}})}{\det(\mathbf{dL_{dq}})} \tag{2.42}$$

where $\mathrm{adj}(\mathbf{dL_{dq}})$ denotes the adjugate and $\det(\mathbf{dL_{dq}})$) represents the determinant.

Certain off-diagonal entries of the inverse matrix in (2.42) can be safely neglected only after the full inversion has been carried out, since their relatively small magnitudes only become evident at that stage. For each system under study, this assumption must be verified; under this hypothesis, the machine model reduces to a form analogous to (2.39), and the machine equation simplifies to:

$$\begin{cases} v_{da} = Ri_{d_a} + \frac{1}{\alpha_{da}} \frac{di_{da}}{dt} \\ v_{qa} = Ri_{q_a} + \frac{1}{\alpha_{qa}} \frac{di_{qa}}{dt} \\ v_{db} = Ri_{d_b} + \frac{1}{\alpha_{db}} \frac{di_{db}}{dt} \\ v_{qb} = Ri_{q_b} + \frac{1}{\alpha_{qb}} \frac{di_{qb}}{dt} \end{cases} \tag{2.43}$$

The PI tuning is performed the same way as the three-phase motor seen in equation (1.1.2), but with two reference axes, instead of one. In the following is reported only the gain formulas used for tuning the modified PI with the second method:

d_a axis:

$$\begin{cases} \text{if } \omega_c < R_s \cdot \alpha_{da} & \Rightarrow \begin{cases} K_p = 0 \\ K_i = \omega_c R_s - \frac{\omega_c^2}{\alpha_{da}} \end{cases} \\ \text{if } \omega_c \geq R_s \cdot \alpha_{da} & \Rightarrow \begin{cases} K_p = \frac{2\xi\omega_c}{\alpha_{da}} - R_s \\ K_i = \frac{\omega_c^2}{\alpha_{da}} \end{cases} \end{cases} \tag{2.44}$$

q_a axis:

$$\begin{cases} \text{if } \omega_c < R_s \cdot \alpha_{qa} & \Rightarrow \begin{cases} K_p = 0 \\ K_i = \omega_c R_s - \frac{\omega_c^2}{\alpha_{qa}} \end{cases} \\ \text{if } \omega_c \geq R_s \cdot \alpha_{qa} & \Rightarrow \begin{cases} K_p = \frac{2\xi\omega_c}{\alpha_{qa}} - R_s \\ K_i = \frac{\omega_c^2}{\alpha_{qa}} \end{cases} \end{cases} \tag{2.45}$$

d_b axis:

$$\begin{cases} \text{if } \omega_c < R_s \cdot \alpha_{db} & \Rightarrow \begin{cases} K_p = 0 \\ K_i = \omega_c R_s - \frac{\omega_c^2}{\alpha_{db}} \end{cases} \\ \text{if } \omega_c \geq R_s \cdot \alpha_{db} & \Rightarrow \begin{cases} K_p = \frac{2\xi\omega_c}{\alpha_{db}} - R_s \\ K_i = \frac{\omega_c^2}{\alpha_{db}} \end{cases} \end{cases} \tag{2.46}$$

q_b axis:

$$\begin{cases} \text{if } \omega_c < R_s \cdot \alpha_{qb} & \Rightarrow \begin{cases} K_p = 0 \\ K_i = \omega_c R_s - \frac{\omega_c^2}{\alpha_{qb}} \end{cases} \\ \text{if } \omega_c \geq R_s \cdot \alpha_{qb} & \Rightarrow \begin{cases} K_p = \frac{2\xi\omega_c}{\alpha_{qb}} - R_s \\ K_i = \frac{\omega_c^2}{\alpha_{qb}} \end{cases} \end{cases} \tag{2.47}$$

For the alternative approach presented in (2.39), the same formulas remain applicable by replacing the parameter α with the corresponding inductance values L defined in the following. More specifically, considering equation (2.41) and neglecting the off-diagonal terms, it is possible to obtain the following:

$$\alpha_{\mathbf{dq,simp}} = \begin{bmatrix} \alpha_1 & 0 & 0 & 0 \\ 0 & \alpha_2 & 0 & 0 \\ 0 & 0 & \alpha_3 & 0 \\ 0 & 0 & 0 & \alpha_4 \end{bmatrix}. \tag{2.48}$$

Consequently, the inductance matrix is obtained by inverting $\alpha_{dq,\text{simp}}$, which, being diagonal, leads to the following expression:

$$\mathbf{L_{dq,simp}} = \begin{bmatrix} \frac{1}{\alpha_{da}} & 0 & 0 & 0 \\ 0 & \frac{1}{\alpha_{qa}} & 0 & 0 \\ 0 & 0 & \frac{1}{\alpha_{db}} & 0 \\ 0 & 0 & 0 & \frac{1}{\alpha_{qb}} \end{bmatrix} \tag{2.49}$$

A comparative analysis of the resulting proportional and integral gains across the previously discussed two methods is presented in figure 5.27.

After computing the PI controller is now considered the feedforward contributions that must be added to the PI controller output, organized by axis:

$$\begin{cases} -M_{qada}i_{da} - L_{qa}i_{qa} - M_{qadb}i_{db} - M_{qaqb}i_{qb} \\ +L_{da}i_{d_a} + M_{daqa}i_{qa} + M_{dadb}i_{db} + M_{daqb}i_{qb} + \varphi_{pm,1} \\ -M_{qbda}i_{d_a} - M_{qbqa}i_{q_a} - M_{qbdb}i_{d_b} - L_{qb}i_{q_b} \\ +M_{dbda}i_{d_a} + M_{dbqa}i_{q_a} + L_{db}i_{d_b} + M_{dbqb}i_{q_b} + \varphi_{pm,2} \end{cases} \tag{2.50}$$

2.2.2 Vector space decomposition

Harmonic decomposition

In dual-three-phase machines, the stator is equipped with two independent three-phase windings, displaced by a fixed electrical angle and connected in a star configuration. The six-phase system is thus amenable to harmonic decomposition via the VSD method, which isolates the contributions of different harmonic orders into orthogonal subspaces.
The core idea is that any periodic quantity in a 6-phase system can be expressed as a sum of harmonic components of different orders:

$$i(t) = \sum_{h=1}^{\infty} \left(I_h e^{jh\omega t} + I_h e^{-jh\omega t} \right) \tag{2.51}$$

Each harmonic order h contributes to a distinct vector subspace in the VSD framework. However, not all harmonics lead to independent or physically significant components due to symmetry, phase redundancy, and the connection topology of the stator windings.

Harmonics in a six-phase machine can be classified as follows:

- **Fundamental harmonic ($h = 1$):** this is the main torque-producing component that is represented with the VSD method in the *space 1*;
- **Triplen harmonics ($h = 3, 6, 9, \dots$):** these are zero-sequence harmonics. In a well-balanced star-connected system without a shared neutral, the triple harmonics

generated by the two sets of windings are in phase and oppose each other, resulting in mutual cancellation;

- **Even-order harmonics ($h = 2, 4, 6, 8, \dots$):** even harmonics are eliminated by design due to the physical symmetry of the machine. The spatial distribution of the windings and the construction of the magnetic field inherently reject even-order harmonics, which would otherwise result in asymmetric magnetic forces and acoustic noise;

- **Non-triplen odd harmonics ($h = 5, 7, 11, \dots$):** these harmonics are not zero-sequence and can physically exist in the machine. They are not inherently canceled by symmetry or winding configuration. In particular, the 5^{th} harmonic often appears in practice due to PWM switching and nonlinearities in the machine or drive. It can have adverse effects such as torque ripple, additional losses, and acoustic noise, and is therefore considered in *space 5*.

Mathematically, for a 6-phase system, the resulting harmonics appear only at orders:

$$h \in \{1, 5, 7, 11, 13, \dots\}$$

The most significant ones, which are indeed considered in the VSD method, are:

- **Space 1 ($h = 1$):** this space contains the fundamental harmonic component and plays a central role in torque generation. It is controlled within a rotating reference frame at angular velocity ω, with the d_1 axis aligned with the first harmonic of the magnetic flux induced by the permanent magnets;

- **Space 5 ($h = 5$):** this space corresponds to the lowest-order non-triplen, non-zero-sequence harmonic, which can negatively impact system performance. It is represented in a rotating reference frame mechanically locked to the rotor but rotating in the opposite direction to the main reference frame, i.e., $\omega_5 = -\omega$.

Control system

VSD provides a systematic framework to manage harmonics complexity by reorganizing the machine's dynamic model into independent orthogonal components. In the case of a dual three-phase motor, the system inherently operates in a six-dimensional space due to the presence of six independent stator currents in *abc* frame and four in *dq*. VSD subdivides the total *dq* space into orthogonal subspaces. The main subspace involves the d_1 and q_1 components that are directly responsible for producing electromagnetic torque and controlling the magnetic flux. This first subspace is obtained from these general formulas, where x is a generic quantity [13]:

$$\begin{cases} x_{d1} = \dfrac{x_{da} + x_{db}}{2} \\ x_{q1} = \dfrac{x_{qa} + x_{qb}}{2} \end{cases} \tag{2.52}$$

The secondary subspace, involving the d_5 and q_5 components, does not directly contribute to fundamental torque production. Instead, it represents degrees of freedom that can be leveraged for auxiliary objectives, such as minimizing current harmonics, balancing thermal loads among phases, permitting power sharing, or enabling fault-tolerant operation.
This second subspace is obtained from these general formulas [13]:

$$\begin{cases} x_{d5} = \dfrac{x^*_{da} - x^*_{db}}{2} \\ x_{q5} = \dfrac{x^*_{qa} - x^*_{qb}}{2} \end{cases} \tag{2.53}$$

The symbol * in this case doesn't represent a reference value, but the complex conjugate.

A third set of components, the zero-sequence subspace, theoretically appears when there is a common-mode voltage. In most isolated star-connected systems, such as the one considered in this study, zero-sequence currents are zero since the system is balanced.
The transformation from the original dq quantities to the decomposed subspaces is mathematically represented by a single transformation matrix $\mathbf{T_{vsd}}$, specifically designed to project the dq vector onto the two orthogonal subspaces:

$$\mathbf{T_{vsd}} = \frac{1}{2} \begin{bmatrix} 1 & 0 & 1 & 0 \\ 0 & 1 & 0 & 1 \\ 1 & 0 & -1 & 0 \\ 0 & -1 & 0 & 1 \end{bmatrix} \tag{2.54}$$

Starting from the equation developed previously in (2.10), it is possible to multiply each term by the transformation matrix $\mathbf{T_{vsd}}$:

$$\mathbf{T_{vsd}}\bar{v} = \mathbf{T_{vsd}} \left(\mathbf{R}\bar{i} + \mathbf{dL_{dq}} \frac{d\bar{i}}{dt} + \omega\, \mathbf{T} \left(\mathbf{L_{dq}}\bar{i} + \bar{\varphi}_{pm} \right) \right) \tag{2.55}$$

Developing all the calculations and knowing that $\mathbf{T_{vsd}}^{-1} \cdot \mathbf{T_{vsd}} = 1$ it is possible to obtain:

$$\mathbf{T_{vsd}}\, \bar{v} = \mathbf{T_{vsd}}\, \mathbf{R}\, \bar{i} + \mathbf{T_{vsd}}\, \mathbf{dL_{dq}} \frac{d\bar{i}}{dt} + \omega \mathbf{T_{vsd}}\, \mathbf{T}\, \mathbf{L_{dq}}\, \mathbf{T_{vsd}^{-1}} (\mathbf{T_{vsd}}\, \bar{i}) + \omega \mathbf{T_{vsd}}\, \mathbf{T}\, \bar{\varphi}_{pm} \tag{2.56}$$

To obtain all the terms in VSD contribution, it is necessary to note that these terms are equivalent:

$$\begin{cases} \mathbf{T_{vsd}} \cdot \mathbf{R} = \mathbf{R} \cdot \mathbf{T_{vsd}} \\ \mathbf{T_{vsd}} \cdot \mathbf{T} = \mathbf{T} \cdot \mathbf{T_{vsd}} \end{cases} \tag{2.57}$$

In conclusion the equation(2.55) becomes:

$$\mathbf{T_{vsd}}\,\bar{v} = \mathbf{R}\,\mathbf{T_{vsd}}\,\bar{i} + \mathbf{T_{vsd}}\,\mathbf{dL_{dq}}\,\mathbf{T_{vsd}^{-1}}\left(\mathbf{T_{vsd}}\,\frac{d\bar{i}}{dt}\right) + \omega\mathbf{T}\,\mathbf{T_{vsd}}\,\mathbf{L_{dq}}\,\mathbf{T_{vsd}^{-1}}(\mathbf{T_{vsd}}\,\bar{i}) + \omega\mathbf{T}\,\mathbf{T_{vsd}}\,\bar{\varphi}_{pm} \tag{2.58}$$

Considering the following substitution:

$$\begin{cases} \bar{v}_{vsd} = \mathbf{T_{vsd}} \cdot \bar{v} \\ \bar{i}_{vsd} = \mathbf{T_{vsd}} \cdot \bar{i} \\ \dfrac{d\bar{i}_{vsd}}{dt} = \mathbf{T_{vsd}} \cdot \dfrac{d\bar{i}}{dt} \\ \bar{\varphi}_{vsd} = \mathbf{T_{vsd}} \cdot \bar{\varphi} \\ \dfrac{d\bar{\varphi}_{vsd}}{d\theta} = \mathbf{T_{vsd}} \cdot \dfrac{d\bar{\varphi}}{d\theta} \\ \bar{\varphi}_{pm,vsd} = \mathbf{T_{vsd}} \cdot \bar{\varphi_{pm}} \\ \mathbf{L_{dq,vsd}} = \mathbf{T_{vsd}} \cdot \mathbf{L_{dq}} \cdot \mathbf{T_{vsd}}^{-1} \\ \mathbf{dL_{dq_{vsd}}} = \mathbf{T_{vsd}} \cdot \mathbf{dL_{dq}} \cdot \mathbf{T_{vsd}}^{-1} \end{cases} \tag{2.59}$$

Finally is possible to write the machine equation in VSD terms:

$$\bar{v}_{vsd} = \mathbf{R}\bar{i}_{vsd} + \mathbf{dL_{dq_{vsd}}}\frac{d\bar{i}_{vsd}}{dt} + \omega\mathbf{T}(\mathbf{L_{dq_{vsd}}}\bar{i}_{vsd} + \bar{\varphi}_{pm,vsd}) \tag{2.60}$$

The primary advantage of the VSD approach lies in its ability to simplify the original system of equations by theoretically diagonalizing the inductance matrix through linear algebra techniques. This diagonalization is essential for formulating effective control strategies, as it allows for independent control of each axis.
Since the control system relies on the incremental inductance, the following analysis focuses on these matrices to provide insight into proper control tuning:

$$\mathbf{dL_{dq,vsd}} = \begin{bmatrix} dL_{d1} & dM_{d1q1} & dM_{d1d2} & dM_{d1q2} \\ dM_{q1d1} & dL_{q1} & dM_{q1d2} & dM_{q1q2} \\ dM_{d2d1} & dM_{d2q1} & dL_{d2} & dM_{d2q2} \\ dM_{q2d1} & dM_{q2q1} & dM_{q2d2} & dL_{q2} \end{bmatrix} \tag{2.61}$$

The component elements are obtained as follows:

$$\frac{1}{2}\begin{bmatrix} dL_{da} + dL_{db} + dM_{dadb} + dM_{dbda} & dM_{daqa} + dM_{daqb} + dM_{dbqa} + dM_{dbqb} \\ dM_{qada} + dM_{qadb} + dM_{qbda} + dM_{qbdb} & dL_{qa} + dL_{qb} + dM_{qaqb} + dM_{qbqa} \\ dL_{da} - dL_{db} + dM_{dadb} - dM_{dbda} & dM_{daqa} + dM_{daqb} - dM_{dbqa} - dM_{dbqb} \\ dM_{qada} + dM_{qadb} - dM_{qbda} - dM_{qbdb} & dL_{qa} - dL_{qb} + dM_{qaqb} - dM_{qbqa} \end{bmatrix} \tag{2.62}$$

$$\begin{bmatrix} dL_{da} - dL_{db} - dM_{dadb} + dM_{dbda} & dM_{daqa} - dM_{daqb} + dM_{dbqa} - dM_{dbqb} \\ dM_{qada} - dM_{qadb} + dM_{qbda} - dM_{qbdb} & dL_{qa} - dL_{qb} - dM_{qaqb} + dM_{qbqa} \\ dL_{da} + dL_{db} - dM_{dadb} - dM_{dbda} & dM_{daqa} - dM_{daqb} - dM_{dbqa} + dM_{dbqb} \\ dM_{qada} - dM_{qadb} - dM_{qbda} + dM_{qbdb} & dL_{qa} + dL_{qb} - dM_{qaqb} - dM_{qbqa} \end{bmatrix}$$

To calculate the K_p and K_i gain, it is possible to use the same formulas presented in the modular approach, where the inductances are the ones presented in equations (2.61) and (2.62). Another important thing to develop is the feedforward compensation that is possible to obtain by developing the terms $\omega \cdot \mathbf{T} \cdot (\mathbf{L_{dq_{vsd}}} \bar{i}_{vsd} + \bar{\varphi}_{pm,vsd})$ present in the equation (2.60). The results are the following:

$$\begin{aligned} EMF_{d1} =& -\omega\Big(i_{qa}\Big(\frac{L_{qa}}{2} + \frac{L_{qb}}{2} - \frac{M_{qaqb}}{2} - \frac{M_{qbqa}}{2}\Big) \\ &+ i_{qb}\Big(\frac{L_{qa}}{2} - \frac{L_{qb}}{2} + \frac{M_{qaqb}}{2} - \frac{M_{qbqa}}{2}\Big) \\ &+ i_{da}\Big(\frac{M_{qada}}{2} + \frac{M_{qadb}}{2} - \frac{M_{qbda}}{2} - \frac{M_{qbdb}}{2}\Big) \\ &+ i_{db}\Big(\frac{M_{qada}}{2} - \frac{M_{qadb}}{2} - \frac{M_{qbda}}{2} + \frac{M_{qbdb}}{2}\Big)\Big) \end{aligned} \tag{2.63}$$

$$\begin{aligned} EMF_{q1} =& \omega\Big(\frac{\varphi_{pm_a}}{2} + \frac{\varphi_{pm_b}}{2} + i_{da}\Big(\frac{L_{da}}{2} + \frac{L_{db}}{2} + \frac{M_{dadb}}{2} + \frac{M_{bdad}}{2}\Big) \\ &+ i_{db}\Big(\frac{L_{da}}{2} - \frac{L_{db}}{2} - \frac{M_{dadb}}{2} + \frac{M_{bdad}}{2}\Big) \\ &+ i_{qa}\Big(\frac{M_{daqa}}{2} - \frac{M_{daqb}}{2} + \frac{M_{dbqa}}{2} - \frac{M_{dbqb}}{2}\Big) \\ &+ i_{qb}\Big(\frac{M_{daqa}}{2} + \frac{M_{daqb}}{2} + \frac{M_{dbqa}}{2} + \frac{M_{dbqb}}{2}\Big)\Big) \end{aligned} \tag{2.64}$$

$$\begin{aligned} EMF_{d2} =& -\omega\Big(i_{qa}\Big(\frac{L_{qa}}{2} - \frac{L_{qb}}{2} - \frac{M_{qaqb}}{2} + \frac{M_{qbqa}}{2}\Big) \\ &+ i_{qb}\Big(\frac{L_{qa}}{2} + \frac{L_{qb}}{2} + \frac{M_{qaqb}}{2} + \frac{M_{qbqa}}{2}\Big) \\ &+ i_{da}\Big(\frac{M_{qada}}{2} + \frac{M_{qadb}}{2} + \frac{M_{qbda}}{2} + \frac{M_{qbdb}}{2}\Big) \\ &+ i_{db}\Big(\frac{M_{qada}}{2} - \frac{M_{qadb}}{2} + \frac{M_{qbda}}{2} - \frac{M_{qbdb}}{2}\Big)\Big) \end{aligned} \tag{2.65}$$

$$
\begin{aligned}
EMF_{q2} = &\omega\Bigg(\frac{\varphi_{pm_a}}{2} - \frac{\varphi_{pm_b}}{2} + i_{da}\Bigg(\frac{L_{da}}{2} - \frac{L_{db}}{2} + \frac{M_{dadb}}{2} - \frac{M_{bdad}}{2}\Bigg) \\
&+ i_{db}\Bigg(\frac{L_{da}}{2} + \frac{L_{db}}{2} - \frac{M_{dadb}}{2} - \frac{M_{bdad}}{2}\Bigg) \\
&+ i_{qa}\Bigg(\frac{M_{daqa}}{2} - \frac{M_{daqb}}{2} - \frac{M_{dbqa}}{2} + \frac{M_{dbqb}}{2}\Bigg) \\
&+ i_{qb}\Bigg(\frac{M_{daqa}}{2} + \frac{M_{daqb}}{2} - \frac{M_{dbqa}}{2} - \frac{M_{dbqb}}{2}\Bigg)\Bigg) \qquad (2.66)
\end{aligned}
$$

The final scheme that describes the system with the controller developed in VSD is the following:

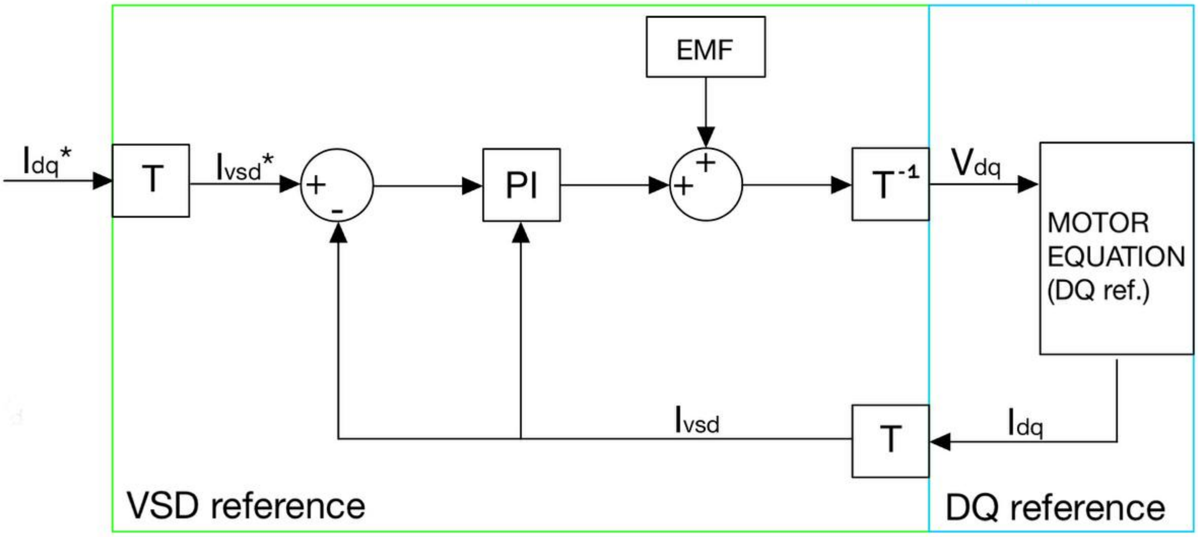

Figure 2.3: VSD control scheme

2.2.3 Novel matrix transformation

In this subsection, an alternative control strategy for a dual-three-phase machine is briefly analyzed. The focus is on highlighting the main differences introduced by adopting a VSD approach. Although the two methods are structurally similar in their Simulink implementations, they differ in the transformation matrix.

According to the formulation presented in [14], and considering that the motor under study is a dual-three-phase systems ($n = 2$), is possible obtain u from the following expression: $1 \leq u \leq n - 1$. The transformation matrix component is given by:

$$Y_u = (n - u) \cdot X_u \quad \text{where} \quad X_u = x_u \cdot I_{2x2} \qquad (2.67)$$

Where the scalar x_u is defined as:

$$x_u = \sqrt{\frac{n}{(n-u)^2 + (n-u)}} = 1 \qquad (2.68)$$

Building upon the results derived from the previous formulas, is now considered the general form of the Novel matrix transformation:

$$\mathbf{T}_{\mathrm{dms}} = \frac{1}{n} \cdot \begin{bmatrix} I_{2\times2} & I_{2\times2} & I_{2\times2} & I_{2\times2} & \cdots & I_{2\times2} \\ Y_1 & -X_1 & -X_1 & -X_1 & \cdots & -X_1 \\ 0_{2\times2} & Y_2 & -X_2 & -X_2 & \cdots & -X_2 \\ 0_{2\times2} & 0_{2\times2} & Y_3 & -X_3 & \cdots & -X_3 \\ 0_{2\times2} & 0_{2\times2} & 0_{2\times2} & \ddots & \ddots & \vdots \\ \vdots & \vdots & \vdots & \ddots & \ddots & -X_{n-2} \\ 0_{2\times2} & 0_{2\times2} & 0_{2\times2} & \cdots & Y_{n-1} & X_{n-1} \end{bmatrix} \tag{2.69}$$

Finally is possible to obtain the matrix for a dual three-phase motor:

$$\mathbf{T}_{\mathrm{dms}} = \frac{1}{2} \begin{bmatrix} 1 & 0 & 1 & 0 \\ 0 & 1 & 0 & 1 \\ 1 & 0 & -1 & 0 \\ 0 & 1 & 0 & -1 \end{bmatrix} \tag{2.70}$$

This approach is well suited to control of a machine in which unequal power/torque sharing is desirable (as the case may be in future electric vehicles with multiple electric energy sources or microgrids with interconnection through a wind generator), as well as to the control of machines with a nonstandard stator winding structure, which is neither symmetrical nor asymmetrical [14].

2.2.4 Real-time PI controller autotuning

The implemented autotuning algorithm enables real-time tuning of PI controllers without requiring prior knowledge of machine parameters. This adaptive capability is especially advantageous in systems where the plant dynamics are subject to change or exhibit nonlinear behavior, such as real SPM and IPM motors. The magnetic saturation of the motor depends on the operating point; therefore, the plant's transfer function can vary significantly. Consequently, a tuning strategy that adapts to the system's operating point is required. To facilitate automatic tuning, the proposed autotuning block introduces frequency harmonic perturbations into the control loop. These frequency harmonic signals enable the identification of the closed-loop transfer function at the current operating point. The injection frequencies are centered around the target crossover pulsation ω_c, and are defined relative to it as follows: $\left\{\frac{1}{10}\omega_c,\ \frac{1}{3}\omega_c,\ \omega_c,\ 3\omega_c,\ 10\omega_c\right\}$.

A significant advantage of the proposed autotuning method is its independence from machine parameters, such inductances. This characteristic makes the method straightforward deployment across various motor types without requiring reconfiguration or parameter retuning. Moreover, the approach ensures consistent control performance over a broad range of operating conditions while significantly reducing the complexity and effort associated with manual tuning procedures. This is particularly beneficial in applications characterized by nonlinear or time-varying dynamics.

2.2.5 Direct flux vector control

In this subsection, a different control method for the machine is analyzed, one that is not based on current, unlike all the previously discussed methods, but rather on the flux.

The most general form of the equation for a dual-three-phase machine is given in (2.5). The current can be expressed as a function of the flux:

$$\bar{\varphi} = \mathbf{L_{dq}}\bar{i} + \bar{\varphi}_{pm} \quad \Rightarrow \quad \bar{i} = \mathbf{L_{dq}}^{-1}(\bar{\varphi} - \bar{\varphi}_{pm}) \tag{2.71}$$

where $\mathbf{L_{dq}}^{-1}$ is the inverse of the apparent inductance matrix obtained in nominal condition. Hereinafter the inverse of the apparent matrix will be defined as:

$$\mathbf{L_{dq}}^{-1} = \beta_{\mathbf{dq}} = \begin{bmatrix} \beta_{d1} & \beta_{d1q1} & \beta_{d1d2} & \beta_{d1q2} \\ \beta_{q1d1} & \beta_{q1} & \beta_{q1d2} & \beta_{q1q2} \\ \beta_{d2d1} & \beta_{d2q1} & \beta_{d2} & \beta_{d2q2} \\ \beta_{q2d1} & \beta_{q2q1} & \beta_{q2d2} & \beta_{q2} \end{bmatrix} \tag{2.72}$$

The derivative of the flux with respect to the time will be defined as:

$$\dot{\bar{\varphi}} = \frac{d\bar{\varphi}}{dt} \tag{2.73}$$

Substituting equation (2.71) in equation (2.5) is possible to obtain:

$$\bar{v} = \mathbf{R}\left(\mathbf{L_{dq}^{-1}}(\bar{\varphi} - \bar{\varphi}_{pm})\right) + \dot{\bar{\varphi}} + \omega T\bar{\varphi} \tag{2.74}$$

Equation (2.74) can now be expressed in terms of the derivative:

$$\dot{\bar{\varphi}} = \bar{v} - \mathbf{R}\left(\mathbf{L_{dq}^{-1}}(\bar{\varphi} - \bar{\varphi}_{pm})\right) - \omega\mathbf{T}\bar{\varphi} \tag{2.75}$$

Collecting $\bar{\varphi}$:

$$\dot{\bar{\varphi}} = -\left(\mathbf{R}\mathbf{L_{dq}^{-1}} + \omega\mathbf{T}\right)\bar{\varphi} + \bar{v} + \mathbf{R}\mathbf{L_{dq}^{-1}}\bar{\varphi}_{pm} \tag{2.76}$$

The state equations are introduced here in their general form and will be formally derived in the next chapter:

$$\begin{cases} \dot{\bar{x}} &= \mathbf{A}\bar{x} + \mathbf{B}\bar{u} + \mathbf{C} \\ \bar{y} &= \mathbf{D}\bar{x} + \mathbf{E}\bar{u} + \mathbf{F} \end{cases} \tag{2.77}$$

where $\mathbf{B} = 1$ and $\mathbf{F} = 0$.
It is possible to express the state equations of the system under study as follows:

$$\begin{cases} \dot{\bar{\varphi}} & = -\left(\mathbf{R}\mathbf{L}_{\mathbf{dq}}^{-1} + \omega\mathbf{S}\right)\bar{\varphi} + \bar{v} + \mathbf{R}\mathbf{L}_{\mathbf{dq}}^{-1}\bar{\varphi}_{pm} \\ \bar{i} & = \mathbf{L}_{\mathbf{dq}}^{-1}\bar{\varphi} - \mathbf{L}_{\mathbf{dq}}^{-1}\bar{\varphi}_{pm} \end{cases} \tag{2.78}$$

Within the scope of this control strategy, it is possible to establish a relationship between torque and fluxes:

$$T_r = f(\bar{\varphi}) \tag{2.79}$$

Such relationship can be exploited in the control architecture shown in figure 2.4.

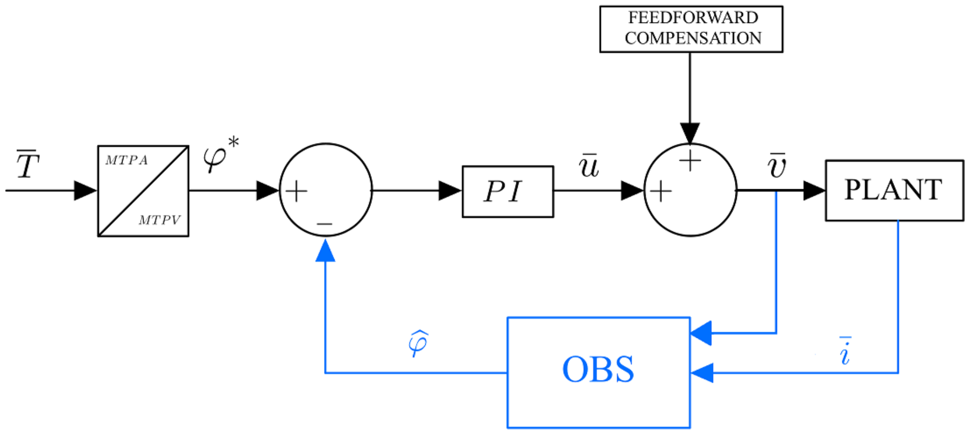

Figure 2.4: Direct flux control

The architecture is similar to that proposed by Pellegrino [15], as illustrated in figure 3.

Going into more detail compared to figure 2.4, here is analyzed the observer using the state-space equation defined in (2.77) and expanded in (2.78):

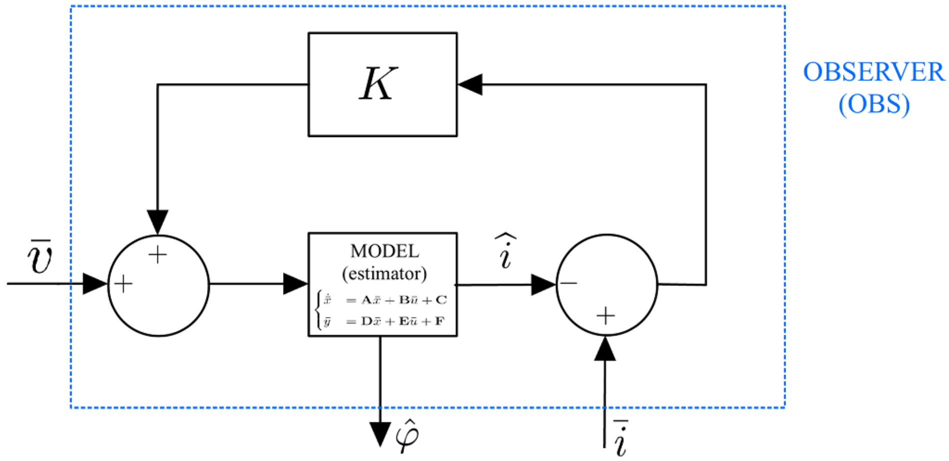

Figure 2.5: Luenberger state space observer

To guarantee the system's asymptotic stability, an error signal is formed by comparing the estimated current with the actual current, which is then used in a feedback loop.

Within the framework of a Kalman filter, the Luenberger gain K adapts dynamically based on the system's noise characteristics. Proper tuning of K ensures asymptotic stability and convergence of the observer's estimates to the real system states in steady state. When optimized, the observer can react faster than the physical system, making it particularly effective for feedback control applications.

Due to its rapid response and asymptotic accuracy, the Luenberger observer's dynamics can be considered negligible in the PI controller tuning process. Specifically, its transfer function can be approximated by a diagonal matrix of ones. From control theory, this implies that if the observer is correctly designed, the observer path (highlighted in blue in (2.4)) can be treated equivalently to an actual measurement and thus omitted from the PI tuning equations.

Expanding equation (2.76) it results:

$$\dot{\bar{\varphi}} = -\mathbf{R}\mathbf{L}_{\mathbf{dq}}^{\mathbf{-1}}\bar{\varphi} - \omega\mathbf{T}\bar{\varphi} + \bar{v} + \mathbf{R}\mathbf{L}_{\mathbf{dq}}^{\mathbf{-1}}\bar{\varphi}_{pm} \tag{2.80}$$

It is now possible to solve the equations for each axis:

$$\begin{aligned} \dot{\varphi}_{da} = v_{da} + \varphi_{qa}(\omega - \beta_{daqa}R_s) + \beta_{da}R_s\varphi_{pm,a} + \beta_{dadb}R_s\varphi_{pm,b} \\ - \beta_{da}R_s\varphi_{da} - \beta_{dadb}R_s\varphi_{db} - \beta_{daqb}R_s\varphi_{qb} \end{aligned} \tag{2.81}$$

$$\begin{aligned} \dot{\varphi}_{qa} = v_{qa} - \varphi_{da}(\omega + \beta_{qada}R_s) + \beta_{qada}R_s\varphi_{pm,a} + \beta_{qadb}R_s\varphi_{pm,b} \\ - \beta_{qa}R_s\varphi_{qa} - \beta_{qadb}R_s\varphi_{db} - \beta_{qaqb}R_s\varphi_{qb} \end{aligned} \tag{2.82}$$

$$\begin{aligned} \dot{\varphi}_{db} = v_{db} + \varphi_{qb}(\omega - \beta_{dbqb}R_s) + \beta_{db}R_s\varphi_{pm,b} + \beta_{dbda}R_s\varphi_{pm,a} \\ - \beta_{db}R_s\varphi_{db} - \beta_{dbda}R_s\varphi_{da} - \beta_{dbqa}R_s\varphi_{qa} \end{aligned} \tag{2.83}$$

$$\begin{aligned} \dot{\varphi}_{qb} = v_{qb} - \varphi_{db}(\omega + \beta_{qbdb}R_s) + \beta_{qbda}R_s\varphi_{pm,a} + \beta_{qbdb}R_s\varphi_{pm,b} \\ - \beta_{qb}R_s\varphi_{qb} - \beta_{qbda}R_s\varphi_{da} - \beta_{qbqa}R_s\varphi_{qa} \end{aligned} \tag{2.84}$$

Now it is possible to obtain the values of the vector $\bar{u}$ for the tuning of the PI:

$$\begin{cases} u_{da} &= \dot{\varphi}_{da} + R_s L_{da}^{-1} \varphi_{da} \\ u_{qa} &= \dot{\varphi}_{qa} + R_s L_{qa}^{-1} \varphi_{qa} \\ u_{db} &= \dot{\varphi}_{db} + R_s L_{db}^{-1} \varphi_{db} \\ u_{qb} &= \dot{\varphi}_{qb} + R_s L_{qb}^{-1} \varphi_{qb} \end{cases} \tag{2.85}$$

All the other terms neglected will be compensated via feedforward after the PI.

Equation for PI tuning

The transfer function for a generic axis of the observer can be written as:

$$\frac{\varphi}{u} = \frac{\varphi}{\dot{\varphi} + R_s L_{dq}^{-1} \varphi} \tag{2.86}$$

which in the Laplace domain, since $\dot{\varphi} = s\varphi$, it results:

$$G(s) = \frac{1}{s + R_s L_{dq}^{-1}} \tag{2.87}$$

The PI equation in Laplace domain is:

$$U(s) = \left(K_p + \frac{K_i}{s}\right)(\varphi^* - \hat{\varphi}) \tag{2.88}$$

2.3 Efficiency and power factor analysis

In electric drive systems, particularly those used in electric vehicles, maximizing motor efficiency across the entire operating range is essential for extending driving range and maintaining effective thermal management.

Efficiency map

An efficiency map provides a visual representation of how effectively a system operates under varying conditions, typically depicted through contour lines or color gradients. The map's axes represent two fundamental operational parameters: motor speed and torque. In this study, the nominal operating conditions are defined as the maximum allowable values for both speed and torque. As such, the first step involves determining these nominal values, which then serve as the boundaries for constructing the efficiency map.

To assess the motor's performance, the system is simulated over a defined grid of speed and torque values:

$$\omega_m \in [\omega_{\min}, \omega_{\max}], \quad T_m \in [T_{\min}, T_{\max}]$$

For this work, the limits are specified as follows:

$$\omega_{\min} = 0\,\text{rpm}, \quad \omega_{\max} = 4500\,\text{rpm}, \quad T_{\min} = 0\,\text{Nm}, \quad T_{\max} = 75\,\text{Nm}$$

At each defined operating point, the model is simulated, and relevant electrical and mechanical quantities are recorded. Motor losses are then computed using a combination of simulation results and model-based assumptions:

- **Copper losses**:

$$\begin{gathered} P_{\text{cu1}} = 3R_s(i_{da}^2 + i_{qa}^2), \quad P_{\text{cu2}} = 3R_s(i_{db}^2 + i_{qb}^2) \\ P_{\text{cu}} = P_{\text{cu1}} + P_{\text{cu2}} \end{gathered} \tag{2.89}$$

- **Iron losses**:

$$P_{\text{iron}} = k_{\text{iron}} \cdot \omega_m^2 \tag{2.90}$$

- **Mechanical losses**:

$$P_{\text{mech\_loss}} = k_{\text{mech}} \cdot \omega_m^2 \tag{2.91}$$

The estimated values of the total losses can be obtained by summing equations (2.89), (2.90), and (2.91):

$$P_{\text{loss}} = P_{\text{cu}} + P_{\text{iron}} + P_{\text{mech\_loss}} \tag{2.92}$$

Finally, the **efficiency** is:

$$\eta = \frac{P_{\text{mech}}}{P_{\text{in}}} = \frac{P_{\text{mech}}}{P_{\text{mech}} + P_{\text{loss}}} \tag{2.93}$$

Where:
The **mechanical output power** is calculated as:

$$P_{\text{mech}} = \omega_m \cdot T_{\text{em}} \tag{2.94}$$

The **electrical input power** is:

$$P_{\text{in}} = P_{\text{mech}} + P_{\text{loss}} \tag{2.95}$$

The simulation process iterates over speed and torque points, computing:

$$\eta(i, j) = \text{efficiency at torque index } i \text{ and speed index } j$$

This results in a 2D efficiency map in the speed-torque domain. It reveals high efficiency regions, and helps identify operating zones to avoid due to poor energy conversion or thermal stress.

Power factor

To determine the power factor of a motor, it is first necessary to calculate the **active** and **reactive** power:

$$P = \frac{3}{2}\left(v_{da}i_{da} + v_{qa}i_{qa} + v_{db}i_{db} + v_{qb}i_{qb}\right) \tag{2.96}$$

$$Q = \frac{3}{2}\left(v_{qa}i_{da} - v_{da}i_{qa} + v_{qb}i_{db} - v_{db}i_{qb}\right) \tag{2.97}$$

The **apparent power** is:

$$S = \sqrt{P^2 + Q^2} \tag{2.98}$$

From these, the **power factor** is computed as:

$$\cos\Phi = \left|\frac{P}{S}\right| \tag{2.99}$$

Chapter 3

System stability

3.1 SISO and MIMO systems

In the field of control systems and communications, Single Input Single Output (SISO) and Multiple Input Multiple Output (MIMO) represent two fundamental system architectures. Their distinction lies in the number of input and output signals that the system processes.

Single input single output

A SISO system is characterized by a single input and a single output, representing the most fundamental structure of a dynamic system. Due to their simplicity, SISO systems are widely used in introductory control theory to demonstrate essential concepts such as system stability and dynamic response. Their behavior is typically modeled using transfer functions, which provide a convenient mathematical framework for analysis. Due to their simplicity, SISO systems allow for straightforward design and analysis using classical control techniques such as Bode plots and Nyquist criteria.
Mathematically, a SISO system can be represented as:

$$y(t) = G(s) \cdot u(t) \tag{3.1}$$

Despite their simplicity, SISO models are often inadequate for capturing the complexity of real-world systems, which typically involve interactions among multiple variables. In this thesis, the only subsystem that can be accurately modeled as a SISO system is the speed control loop. In an electric motor, this loop consists of a PI controller that compares the reference speed with the measured speed, producing a reference for the i_q and i_d current components. These current components directly influence the electromagnetic torque generated by the motor.

Multiple input multiple output

In contrast, a MIMO system involves multiple inputs and multiple outputs. This configu-

ration is more representative of complex engineering systems like the current control of a dual three-phase motor that presents as input 4 voltages and as output 4 currents.
A typical state-space representation for a MIMO system is:

$$\begin{cases} \dot{\bar{x}}(t) = \mathbf{A}\bar{x}(t) + \mathbf{B}\bar{u}(t) \\ \bar{y}(t) = \mathbf{C}\bar{x}(t) + \mathbf{D}\bar{u}(t) \end{cases} \tag{3.2}$$

where $\bar{x}(t) \in \mathbb{R}^n$, $\bar{u}(t) \in \mathbb{R}^m$, and $\bar{y}(t) \in \mathbb{R}^p$, with $m, p > 1$ for MIMO configurations.

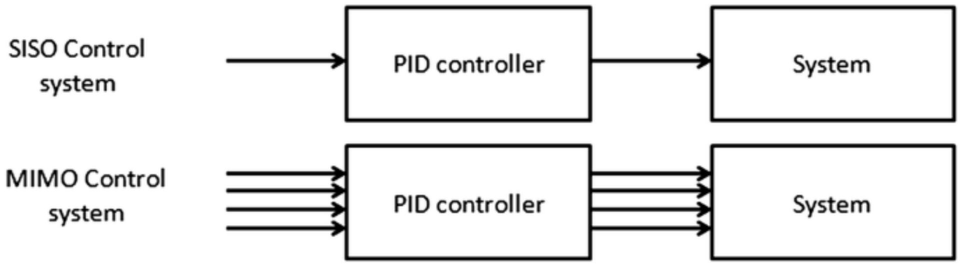

Figure 3.1: SISO and MIMO

3.2 Bode and Nyquist plots

In this section, the behavior of the motor control system is analyzed using frequency-domain techniques, specifically the **Bode plot** and the **Nyquist plot**. These analytical tools are essential for assessing system stability, bandwidth, and overall control performance, especially in feedback-controlled systems.
The first step in applying these tools involves determining the forward loop transfer function, denoted as $G(s)$, and the feedback path transfer function, denoted as $H(s)$. Using these, the closed-loop transfer function $G_t(s)$ can be expressed as:

$$G_t(s) = \frac{G(s)}{1 + G(s)H(s)} \tag{3.3}$$

To analyze the stability of the closed-loop system, it is necessary to examine the poles of $G_t(s)$, which are obtained by solving for the values of s that satisfy the equation:

$$1 + G(s)H(s) = 0 \tag{3.4}$$

The roots of this equation, i.e., the zeros of $1 + G(s)H(s)$, correspond to the poles of the closed-loop system and are critical for determining its stability.

Considering the closed-loop state-space representation presented in equation (1.42), and recognizing that equation (3.3) provides the general formulation for computing the closed-loop state-space model from the transfer functions $G(s)$ and $H(s)$, as illustrated in figure 1.3, the analysis is carried out using Matlab symbolic tools. Given that the forward path transfer function is defined as

$$G(s) = \left(K_p + \frac{K_i}{s}\right) \cdot \frac{1}{Js + B} \tag{3.5}$$

which corresponds to the combination of the PI controller and the plant, it follows that $H(s) = 1$. This indicates that the feedback path is unity, and thus does not modify the feedback response.

Bode Diagram

The Bode diagram consists of two plots: the magnitude (in dB) and the phase (in degrees) of the system's transfer function as functions of frequency. This representation provides direct insight into how the system responds to sinusoidal inputs at various frequencies. Key characteristics that can be extracted from the Bode diagram include:

- **Gain crossover frequency**: the frequency at which the magnitude crosses 0 dB;
- **Phase crossover frequency**: the frequency at which the phase crosses $-180°$;
- **Phase margin**: the additional phase lag required to bring the system to the verge of instability. A phase margin of 60–75° is typically desired;
- **Gain margin**: the increase in gain required to make the system unstable. This is often expressed in dB and should be at least 3 dB;
- **Low-frequency gain**: the low-frequency behavior of the Bode magnitude plot, particularly the gain near 0 Hz, provides critical information about the system's steady-state performance;
- **Resonance peaks**: resonance peaks appear in the Bode magnitude plot as sharp increases in gain at specific frequencies, often close to the system's natural frequency. These peaks are indicative of low damping in the system and can result in oscillatory or even unstable behavior in response to disturbances or setpoint changes.

Nyquist diagram

The Nyquist diagram represents the frequency response of a system by plotting the open-loop transfer function $G(j\omega)H(j\omega)$ on the complex plane as the frequency ω varies continuously from $-\infty$ to $+\infty$. This graphical representation provides a comprehensive characterization of the system's behavior under sinusoidal excitation. Furthermore, the Nyquist plot constitutes a fundamental tool for analyzing the stability of closed-loop feedback systems via the Nyquist stability criterion.

A key element of this criterion is the **encirclement of the critical point $-1 + j0$** in the complex plane. Specifically, the closed-loop stability is determined by the number of clockwise encirclements of the point $(-1, 0)$ combined with the count of open-loop poles located in the right half of the complex s-plane. This relationship is formally expressed by the following equation:

$$Z = N + P \tag{3.6}$$

Where:

- Z denotes the number of zeros of equation G(s) in the right half-plane, corresponding to the unstable poles of the closed-loop transfer function;
- N represents the number of clockwise encirclements of the point $(-1, 0)$ by the Nyquist plot of $L_i = G(j\omega)H(j\omega)$.

In practice, the net encirclements N can be computed numerically by:

$$N = \sum_{i=1}^{n-1} \begin{cases} 1 & \text{if } \begin{cases} \Big(\mathrm{Re}(L_i) + 1\Big) \cdot (\mathrm{Re}(L_{i+1}) + 1\Big) < 0 \\ \mathrm{Im}(L_i) \cdot \mathrm{Im}(L_{i+1}) < 0 \\ \mathrm{Im}(L_{i+1}) < 0 \end{cases} \\ 0 & \text{otherwise} \end{cases} \tag{3.7}$$

Where:

- $\Big(\mathrm{Re}(L_i) + 1\Big)\Big(\mathrm{Re}(L_{i+1}) + 1\Big) < 0$: detects a crossing of the vertical line $\mathrm{Re}(s) = -1$;
- $\mathrm{Im}(L_i) \cdot \mathrm{Im}(L_{i+1}) < 0$: indicates a crossing of the real axis;
- $\mathrm{Im}(L_{i+1}) < 0$: ensures that the crossing occurs from the upper half-plane to the lower half-plane, corresponding to a clockwise encirclement.
  The sum counts the number of such clockwise crossings, which approximates the number of encirclements of the critical point $(-1, 0)$ by the Nyquist plot.

P is the number of open-loop poles of $G(s)H(s)$ that lie in the right half of the complex plane. The number P of unstable open-loop poles is given by:

$$P = \sum_{\text{poles } p_i} \mathbf{1}_{\{\mathrm{Re}(p_i) > 0\}}. \tag{3.8}$$

The Nyquist criterion states that a system is stable if and only if Z=0, meaning that all poles of the closed-loop transfer function lie in the left half of the complex plane.

The formulas analyzed in this chapter apply to a three-phase speed control system. They can also be used for dual three-phase motors, provided that both sections have identical characteristics and share a common shaft.

3.3 State space representation

3.3.1 Input-state-output form

In the analysis and control of dynamic systems, the state-space representation offers a comprehensive framework that describes a system's behavior through a set of first-order differential equations. This formulation is centered around three key components:

- **Input**: denoted by $\bar{u}(t)$, refers to the external signals that are applied to the system. These inputs are typically known functions of time:

$$\bar{u}(t) \in \mathbb{R}^m$$

- **State**: denoted by $\bar{x}(t)$, embodies the internal status of the system at any given time. It captures all the information necessary to describe the future behavior of the system when combined with the input:

$$\bar{x}(t) \in \mathbb{R}^n$$

- **Output**: denoted by $\bar{y}(t)$, represents the set of measurable quantities derived from the internal states and inputs of the system. These are the variable measurements and are often the quantities of interest for control purposes:

$$\bar{y}(t) \in \mathbb{R}^p$$

Linearization of nonlinear systems

For nonlinear systems, this representation must often be linearized around a specific operating point to enable control design and analysis using easier methods.

General nonlinear formulation

The nonlinear continuous-time system is typically represented as:

$$\begin{cases} \dfrac{d\bar{x}(t)}{dt} = f(\bar{x}(t), \bar{u}(t), t) \\ \bar{y}(t) = g(\bar{x}(t), \bar{u}(t), t) \end{cases} \tag{3.9}$$

To simplify control synthesis, it is often beneficial to linearize the nonlinear system around an equilibrium point $(\bar{x}_e, \bar{u}_e)$ that in this thesis is the nominal condition of the motor. This process assumes small deviations $\delta\bar{x}(t)$ and $\delta\bar{u}(t)$ from the equilibrium, where:

$$\bar{x}(t) = \bar{x}_e + \delta\bar{x}(t), \quad \bar{u}(t) = \bar{u}_e + \delta\bar{u}(t) \tag{3.10}$$

First order linearization via Taylor expansion

The criterion of small deviations refers to perturbations of sufficiently limited magnitude such that the Taylor series expansion can be truncated after the first-order terms while maintaining acceptable approximation accuracy:

$$f(\bar{\mathbf{x}}, \bar{u}) \approx f(\bar{x}_e, \bar{u}_e) + \left.\frac{\partial f}{\partial \bar{x}}\right|_{(\bar{x}_e, \bar{u}_e)} \delta\bar{x} + \left.\frac{\partial f}{\partial \bar{u}}\right|_{(\bar{x}_e, \bar{u}_e)} \delta\bar{u} \tag{3.11}$$

Given that $f(\bar{x}_e, \bar{u}_e) = 0$ at equilibrium, it is possible to rewrite the first equation of the (3.9) in the following way:

$$\frac{d}{dt}\delta\bar{x}(t) \approx \mathbf{A}(t)\delta\bar{\mathbf{x}}(t) + \mathbf{B}(t)\delta\bar{u}(t) \tag{3.12}$$

where:

$$\mathbf{A}(t) \equiv \left.\frac{\partial f}{\partial \bar{x}}\right|_{(\bar{x}_e, \bar{u}_e)}, \quad \mathbf{B}(t) \equiv \left.\frac{\partial f}{\partial \bar{u}}\right|_{(\bar{x}_e, \bar{u}_e)} \tag{3.13}$$

These matrices are known as the Jacobian matrices of the system, evaluated at the equilibrium point. Specifically:

$$\mathbf{A}(t) = \begin{bmatrix} \frac{\partial f_1}{\partial x_1} & \cdots & \frac{\partial f_1}{\partial x_n} \\ \vdots & \ddots & \vdots \\ \frac{\partial f_n}{\partial x_1} & \cdots & \frac{\partial f_n}{\partial x_n} \end{bmatrix}_{(\bar{x}_e, \bar{u}_e)}, \quad \mathbf{B}(t) = \begin{bmatrix} \frac{\partial f_1}{\partial u_1} & \cdots & \frac{\partial f_1}{\partial u_m} \\ \vdots & \ddots & \vdots \\ \frac{\partial f_n}{\partial u_1} & \cdots & \frac{\partial f_n}{\partial u_m} \end{bmatrix}_{(\bar{x}_e, \bar{u}_e)} \tag{3.14}$$

This linearization is valid in a neighborhood around the equilibrium, under the assumption that deviations are small enough to neglect higher-order terms.
In the following, other assumptions and approximations are introduced:

1. **Linearization around an equilibrium point:**
   The nonlinear system $\dot{x} = f(x, u)$ is linearized around a constant operating point $(\bar{x}_e, \bar{u}_e)$ such that:

$$\mathbf{A}(t) \equiv \left.\frac{\partial f}{\partial \bar{x}}\right|_{(\bar{x}_e, \bar{u}_e)} = const \quad \mathbf{B}(t) \equiv \left.\frac{\partial f}{\partial \bar{u}}\right|_{(\bar{x}_e, \bar{u}_e)} = const \tag{3.15}$$

   This simplifies the Jacobian matrices to constant values. It is possible to pass from $\mathbf{A}(t)$ and $\mathbf{B}(t)$ to $\mathbf{A}$ and $\mathbf{B}$ respectively.

2. **Simplification of notation:**
   Once the system is expressed in terms of deviations $\delta x(t)$, $\delta u(t)$, and linearized around a constant point, it is common engineering practice to drop the δ notation for readability. Variables are thus redefined with respect to the equilibrium, leading to the compact LTI representation.

The expression (3.12) can be rewritten with the addition of a constant term $\mathbf{C}$:

$$\dot{\bar{x}}(t) = \mathbf{A}\bar{x}(t) + \mathbf{B}\bar{u}(t) + \mathbf{C} \tag{3.16}$$

For the second equation presented in (3.9), the calculations are very similar to those obtained in the first one:

$$\bar{y}(t) \approx \mathbf{D}(t)\delta\bar{x}(t) + \mathbf{E}(t)\delta\bar{u}(t) \tag{3.17}$$

with:

$$\mathbf{D(t)} = \left.\frac{\partial g}{\partial \bar{x}}\right|_{(\bar{\mathbf{x}}_e, \bar{\mathbf{u}}_e)}, \quad \mathbf{E(t)} = \left.\frac{\partial g}{\partial \bar{u}}\right|_{(\bar{\mathbf{x}}_e, \bar{\mathbf{u}}_e)} \tag{3.18}$$

These are the Jacobian matrices of the output function $g(\bar{x}, \bar{u}, t)$ evaluated at the operating point, and describe how small deviations in state and input affect the output.
The final linearized model, derived under the same assumptions as the first formulation, yields the following representation:

$$\bar{y}(t) = \mathbf{C}(t)\bar{x}(t) + \mathbf{D}(t)\bar{u}(t) \tag{3.19}$$

In compact form, the state space equation that is used in the following are:

$$\begin{cases} \dot{\bar{x}}(t) = \mathbf{A}\bar{x}(t) + \mathbf{B}\bar{u}(t) + \mathbf{C} \\ \bar{y}(t) = \mathbf{D}\bar{x}(t) + \mathbf{E}\bar{u}(t) \end{cases} \tag{3.20}$$

3.3.2 Open loop state space equation

After analyzing the general structure of the state-space equations, the formulation is adapted for the specific case in which the state and the output correspond to the currents, while the input is the applied voltage. Accordingly, the first equation in (3.20) can be rewritten as:

$$\dot{\bar{i}}(t) = \mathbf{A_{ol}}\bar{i}(t) + \mathbf{B_{ol}}\bar{v}(t) + \mathbf{C_{ol}} \tag{3.21}$$

By taking the machine equation presented in (2.10) and rearranging its terms, it is possible to express it in a form compatible with the state-space representation:

$$\frac{d\bar{i}}{dt} = -\mathbf{dL_{dq}}^{-1}\left(\mathbf{R} + \omega\mathbf{T}\mathbf{L_{dq}}\right)\bar{i} + \mathbf{dL_{dq}}^{-1}\bar{v} - \mathbf{dL_{dq}}^{-1}\omega\mathbf{T}\bar{\varphi}_{pm} \tag{3.22}$$

From this expression, considering $\omega = const$, the system matrices can be identified as follows:

$$\begin{cases} \mathbf{A_{ol}} = -\mathbf{dL_{dq}}^{-1}\left(\mathbf{R} + \omega \mathbf{T} \mathbf{L_{dq}}\right) \\ \mathbf{B_{ol}} = \mathbf{dL_{dq}}^{-1} \\ \mathbf{C_{ol}} = -\mathbf{dL_{dq}}^{-1} \omega \mathbf{T} \bar{\varphi}_{pm} \end{cases} \tag{3.23}$$

3.3.3 Closed loop state space

Modified PI without feedforward compensation

To ensure accurate current regulation and reference tracking of the desired current a PI controller is employed. The voltage reference vector $\bar{v}$ is determined by the following control law:

$$\bar{v} = \mathbf{K_i} \cdot \bar{z} - \mathbf{K_p} \cdot \bar{i} \tag{3.24}$$

Where:

$$\begin{cases} \mathbf{K_p} = \mathrm{diag}(K_{p,da},\ K_{p,qa},\ K_{p,db},\ K_{p,qb}) \\ \mathbf{K_i} = \mathrm{diag}(K_{i,da},\ K_{i,qa},\ K_{i,db},\ K_{i,qb}) \\ \bar{z} = \frac{1}{s}(\bar{i}^* - \bar{i}) \Rightarrow \dot{\bar{z}} = \mathbf{I_4} \cdot \bar{i}^* - \mathbf{I_4} \cdot \bar{i} \end{cases} \tag{3.25}$$

Combining the equations (3.22) and (3.24), it is possible to write the closed-loop system:

$$\frac{d\bar{i}}{dt} = \mathbf{dL_{dq}}^{-1} \mathbf{K_i} \cdot \bar{z} - \mathbf{dL_{dq}}^{-1}\left(\mathbf{K_p} + \mathbf{R} + \omega \mathbf{T} \mathbf{L_{dq}}\right) \bar{i} - \mathbf{dL_{dq}}^{-1} \omega \mathbf{T} \bar{\varphi}_{pm} \tag{3.26}$$

From this expression, considering $\omega = const$, the system matrices can be identified as follows:

$$\begin{cases} \mathbf{A_{cl}} = \mathbf{K_p} + \mathbf{R} + \omega \mathbf{T} \mathbf{L_{dq}} \\ \mathbf{B_{cl}} = \mathbf{dL_{dq}}^{-1} \mathbf{K_i} \bar{z} \\ \mathbf{C_{cl}} = \mathbf{dL_{dq}}^{-1} \omega \mathbf{T} \bar{\varphi}_{pm} \end{cases} \tag{3.27}$$

The overall closed-loop system can be rewritten as a matrix combining the (3.25) and the (3.26) for obtain the following expression:

$$\begin{bmatrix} \dot{\bar{i}} \\ \dot{\bar{z}} \end{bmatrix} = \begin{bmatrix} \mathbf{A_{cl}} & \mathbf{B_{cl}} \\ -\mathbf{I_4} & 0 \end{bmatrix} \begin{bmatrix} \bar{i} \\ \bar{z} \end{bmatrix} + \begin{bmatrix} \mathbf{C_{cl}} & 0 \\ 0 & \mathbf{I_4} \end{bmatrix} \begin{bmatrix} 1 \\ \bar{i}^* \end{bmatrix} \tag{3.28}$$

Modify PI with feedforward compensation

To improve dynamic response, feedforward compensation is added:

$$\bar{v}_{ff} = \omega \mathbf{T}(\mathbf{L_{dq}} \cdot \bar{i} + \bar{\varphi}_{pm}) \tag{3.29}$$

Thus, the total voltage output becomes combining (3.24) and (3.29):

$$\bar{v} = \bar{v}_{in} + \bar{v}_{ff} = +\mathbf{K_i}\bar{z} - \mathbf{K_p}\bar{i} + \omega\mathbf{T}\mathbf{L_{dq}}\bar{i} + \omega\mathbf{T}\bar{\varphi}_{pm} \tag{3.30}$$

Beginning with the open-loop state-space representation (3.22) and substituting the voltage equation given in (3.30), the resulting system becomes:

$$\begin{bmatrix} \dot{\bar{i}} \\ \dot{\bar{z}} \end{bmatrix} = \mathbf{A_{cl,ff}} \begin{bmatrix} \bar{i} \\ \bar{z} \end{bmatrix} + \mathbf{B_{cl,ff}} \begin{bmatrix} 1 \\ \bar{i}^* \end{bmatrix} \tag{3.31}$$

Where:

$$\mathbf{A_{cl,ff}} = \begin{bmatrix} -\mathbf{dL_{dq}^{-1}}(\mathbf{R_s} + \omega\mathbf{T}\mathbf{L_{dq}} + \mathbf{K_p}) & \mathbf{dL_{dq}^{-1}}\mathbf{K_i} \\ -\mathbf{I_4} & 0 \end{bmatrix} \tag{3.32}$$

$$\mathbf{B_{cl,ff}} = \begin{bmatrix} 0 & 0 \\ 0 & \mathbf{I_4} \end{bmatrix} \tag{3.33}$$

Classic PI without feedforward compensation

To simplify the control system tuning process, Simulink provides an automated procedure for PI controller adjustment. This feature allows the user to specify the desired bandwidth [rad/s] and phase margin [deg]. Based on these inputs, Simulink internally computes suitable values for proportional and integral gains, ensuring a balance between responsiveness and stability.
The classical PI controller can be represented by the following transfer function:

$$\bar{v} = \mathbf{K_p}(\bar{i}^* - \bar{i}) + \frac{\mathbf{K_i}}{s}(\bar{i}^* - \bar{i}) \tag{3.34}$$

To facilitate further analysis, the auxiliary variables are introduced:

$$\bar{z} = \frac{\bar{i}^* - \bar{i}}{s} \quad \Rightarrow \quad \dot{\bar{z}} = \bar{i}^* - \bar{i} \tag{3.35}$$

$$\bar{x} = \frac{\mathbf{K_i}}{s}\bar{z} \tag{3.36}$$

Using these definitions, equation (3.34) can be equivalently expressed as:

$$\bar{v} = \bar{x} + \mathbf{K_p}\dot{\bar{z}} \tag{3.37}$$

By combining equations (3.22) and (3.37), the closed-loop system can be expressed as:

$$\frac{d\bar{i}}{dt} = \mathbf{dL_{dq}}^{-1}\left[-\left(\mathbf{R} + \omega\mathbf{T}\mathbf{L_{dq}} + \mathbf{K_p}\right)\bar{i} + \mathbf{K_p}\bar{i}^* + \frac{\mathbf{K_i}}{s}\bar{z} - \omega\mathbf{T}\bar{\varphi}_{pm}\right] \tag{3.38}$$

Classic PI with feedforward compensation

To improve dynamic response, feedforward compensation is added with the same way presented in (3.29). Thus, the total voltage output becomes combining (3.34) and (3.29):

$$\bar{v} = \bar{v}_{in} + \bar{v}_{ff} = \mathbf{K_p}\dot{\bar{z}} + K_i\bar{z} + \omega\mathbf{T}\mathbf{L_{dq}}\bar{i} + \omega\mathbf{T}\bar{\varphi}_{pm} \tag{3.39}$$

Beginning with the open-loop state-space representation (3.22) and substituting the voltage equation given in (3.39), the resulting system becomes:

$$\begin{bmatrix}\dot{\bar{i}}\\ \dot{\bar{z}}\end{bmatrix} = \mathbf{A_{cl,ff}}\begin{bmatrix}\bar{i}\\ \bar{z}\end{bmatrix} + \mathbf{B_{cl,ff}}\begin{bmatrix}1\\ \bar{i}^*\end{bmatrix} \tag{3.40}$$

Where:

$$\mathbf{A_{cl,ff}} = \begin{bmatrix}-\mathbf{dL_{dq}^{-1}}(\mathbf{R_s} + \omega\mathbf{T}\mathbf{L_{dq}} + \mathbf{K_p}) & \mathbf{dL_{dq}^{-1}K_i}\\ -\mathbf{I_4} & 0\end{bmatrix} \tag{3.41}$$

$$\mathbf{B_{cl,ff}} = \begin{bmatrix}0 & \mathbf{dL_{dq}^{-1}K_p}\\ 0 & \mathbf{I_4}\end{bmatrix} \tag{3.42}$$

This analysis serves to demonstrate that the matrix $\mathbf{A_{cl,ff}}$ obtained in (3.32) and (3.41) contains exactly the same terms. Consequently, the eigenvalue computation presented in the next chapter will yield identical results. The only distinction lies in the matrix $\mathbf{B_{cl,ff}}$.

3.3.4 Eigenvalues

Consider a LTI system described in state-space form, as defined in equation (3.20). Applying the Laplace transform under the assumption of zero initial conditions yields:

$$\begin{cases} s\bar{x}(s) = \mathbf{A}\bar{x}(s) + \mathbf{B}\bar{u}(s) + \mathcal{L}\{\mathbf{C}\}\\ \bar{y}(s) = \mathbf{D}\bar{x}(s) + \mathbf{E}\bar{u}(s)\end{cases} \tag{3.43}$$

Since $\mathbf{C}$ is constant with respect to time, its Laplace transform is:

$$\mathcal{L}\{\mathbf{C}\} = \frac{\mathbf{C}}{s} \tag{3.44}$$

Therefore, the first equation becomes:

$$(sI - \mathbf{A})\bar{x}(s) = \mathbf{B}\bar{u}(s) + \frac{\mathbf{C}}{s} \tag{3.45}$$

Solving for $\bar{x}(s)$:

$$\bar{x}(s) = (sI - \mathbf{A})^{-1}\mathbf{B}\bar{u}(s) + (sI - \mathbf{A})^{-1}\frac{\mathbf{C}}{s} \tag{3.46}$$

Substituting into the second equation:

$$\begin{aligned}\bar{y}(s) &= \mathbf{D}\bar{x}(s) + \mathbf{E}\bar{u}(s) \\ &= \mathbf{D}(sI - \mathbf{A})^{-1}\mathbf{B}\bar{u}(s) + \mathbf{E}\bar{u}(s) + \mathbf{D}(sI - \mathbf{A})^{-1}\frac{\mathbf{C}}{s}\end{aligned} \tag{3.47}$$

Hence, the output consists of two parts:

- Where the transfer function $\bar{y}(s)/\bar{u}(s)$ is:

$$\frac{\bar{y}(s)}{\bar{u}(s)} = \mathbf{D}(sI - \mathbf{A})^{-1}\mathbf{B} + \mathbf{E} \tag{3.48}$$

- An additional term caused by the constant input:

$$Y_{\text{offset}}(s) = \mathbf{D}(sI - \mathbf{A})^{-1}\frac{\mathbf{C}}{s} \tag{3.49}$$

This offset term does not affect the transfer function, which is defined as the ratio $\bar{y}(s)/\bar{u}(s)$ and depends solely on the linear input-output relationship under zero input bias. The constant term contributes to the steady-state behavior but is not part of the system's transfer function.
In control theory, the poles of a transfer function are defined as the complex values of s for which the denominator becomes zero. For a system represented in state-space form, the poles correspond to the values of s for which the matrix $(sI - \mathbf{A})$ is not invertible. This occurs when:

$$\det(sI - \mathbf{A}) = 0 \tag{3.50}$$

This equation defines the *characteristic polynomial* of $\mathbf{A}$, and its roots are precisely the *eigenvalues* of A. Thus, the poles of the system coincide with the eigenvalues of the $\mathbf{A}$.

To find the eigenvalues, it is first necessary to compute the characteristic polynomial, which can be generally expressed as [16]:

$$p(\lambda) \;=\; a_0\lambda^n + a_1\lambda^{n-1} + ...a_n = 0 \tag{3.51}$$

Where:

$$\begin{aligned} a_0 &= (-1)^n = \sum_{i=1}^{n} a_{ii} = \operatorname{tr}(A_{cl}) \\ a_1 &= (-1)^{n-1}\sum_{i=1}^{n} a_{ii} \\ &\vdots \\ a_n &= \det(A_{cl}) \end{aligned} \tag{3.52}$$

For a 8×8 matrix A_{cl} ($n = 8$), the characteristic polynomial can be written as:

$$p(\lambda) = \lambda^8 - a_1\lambda^7 + a_2\lambda^6 - a_3\lambda^5 + a_4\lambda^4 - a_5\lambda^3 + a_6\lambda^2 - a_7\lambda + a_8 \tag{3.53}$$

The eigenvalues $\{\lambda_i\}_{i=1}^{8}$ are the roots of the characteristic polynomial $p(\lambda)$, obtained using Matlab. Each eigenvalue λ is, in general, a complex number and can be interpreted through its real and imaginary components [17]. These components allow the computation of the natural frequency as follows:

$$\omega_n = \sqrt{\mathrm{Re}^2(\lambda) + \mathrm{Im}^2(\lambda)} \tag{3.54}$$

And the calculation of the damping ratio [18]:

$$\zeta = \frac{-\,\mathrm{Re}(\lambda)}{\sqrt{\mathrm{Re}(\lambda)^2 + \omega_n^2}} \tag{3.55}$$

The magnitude of the real part of the eigenvalue, normalized by the natural frequency, indicates the speed of decay (or divergence) of the oscillation [18]. For this reason, greater attention should be given to the eigenvalues located closer to the imaginary axis, provided that their real parts remain negative. This condition is necessary to satisfy the system's stability criterion:

$$\mathrm{Re}(\lambda_i) < 0 \quad \text{for all } i = 1, \ldots, 8. \tag{3.56}$$

3.3.5 Mechanical subsystem and torque model

Although this study primarily focuses on the electrical domain, the rotor dynamics must also be considered. They are governed by Newton's second law:

$$J \cdot \frac{d\omega}{dt} = T_e - T_L - B \cdot \omega \tag{3.57}$$

The electromagnetic torque for a dual three-phase machine is given by:

$$T_e = \frac{3}{2} P \left(\varphi_{da} i_{qa} - \varphi_{qa} i_{da} + \varphi_{db} i_{qb} - \varphi_{qb} i_{db}\right) \tag{3.58}$$

Combining equations (3.57) and (3.58), it is possible to obtain the derivative of the angular velocity with respect to the speed:

$$\dot{\omega} = J^{-1} \cdot \left(\frac{3}{2} P \left(\varphi_{da} i_{qa} - \varphi_{qa} i_{da} + \varphi_{db} i_{qb} - \varphi_{qb} i_{db}\right) - T_L - B \cdot \omega\right) \tag{3.59}$$

It is possible to define the mechanical equation applied in state space:

$$\frac{d\omega}{dt} = \mathbf{A} \cdot \omega + \mathbf{B} \cdot T_L + \mathbf{C} \tag{3.60}$$

Where:

$$\begin{cases} \mathbf{A} = -J^{-1}B \\ \mathbf{B} = -J^{-1} \\ \mathbf{C} = \dfrac{3}{2}PJ^{-1}\left(\varphi_{da}i_{qa} - \varphi_{qa}i_{da} + \varphi_{db}i_{qb} - \varphi_{qb}i_{db}\right) \end{cases} \tag{3.61}$$

The coupled electromechanical system can, in principle, be integrated with the electrical subsystem described by the matrix formulation presented in equation (3.28). Such integration would result in an augmented state-space representation, thereby increasing both the dimensionality of the system matrix and the overall complexity of the mathematical model. The inclusion of mechanical dynamics introduces additional differential equations corresponding to mechanical states.

Nevertheless, for the scope of this study, the mechanical subsystem has been deliberately excluded from the numerical simulations. This modeling simplification is based on two primary considerations. First, the mechanical dynamics typically evolve on a much slower time scale compared to the fast transients observed in the electrical components of the system. Second, the mechanical part is generally stable and does not exhibit behaviors that critically influence the transient or steady-state performance of the electrical system.

Chapter 4

Model parameters of the machine

In this chapter, the main characteristics of the dual-three-phase machine under study are analyzed. The first part describes all the geometric dimensions of the machine, followed by an analysis of the inductances as functions of the current for each machine.

4.1 Case study parameters

Description	**Symbol**	**Numerical Value**	**Unit of Measure**
Number of pole pairs	P	4	–
Number of slots	N_s	48	–
Nominal voltage	V_{DC}	400	V
Nominal current	i_{nom}	71.25	A_{pk}
Stator resistance	R	1.3	Ω
Motor inertia	J	0.005	kg·m^2
Internal stator diameter	D	0.138	m
External stator diameter	D_{ext}	0.203	m
Internal rotor diameter	D_{int}	0.04	m
Slot area	S_{slot}	1.58×10^{-4}	m^2
Sector shift	α	30	rad/s
Active length	L	0.108	m
Rotor and stator material	M250-35A	–	–
Magnet material	N28UH	–	–

Table 4.1: Dual-three-phase parameters valid for both SPM and IPM [5]

These parameters, which include both electromagnetic and geometric specifications, define the fundamental characteristics of the motor's architecture and performance. The dimensional parameters, in particular, are geometrically referenced to the machine cross-section shown in figure 4.1:

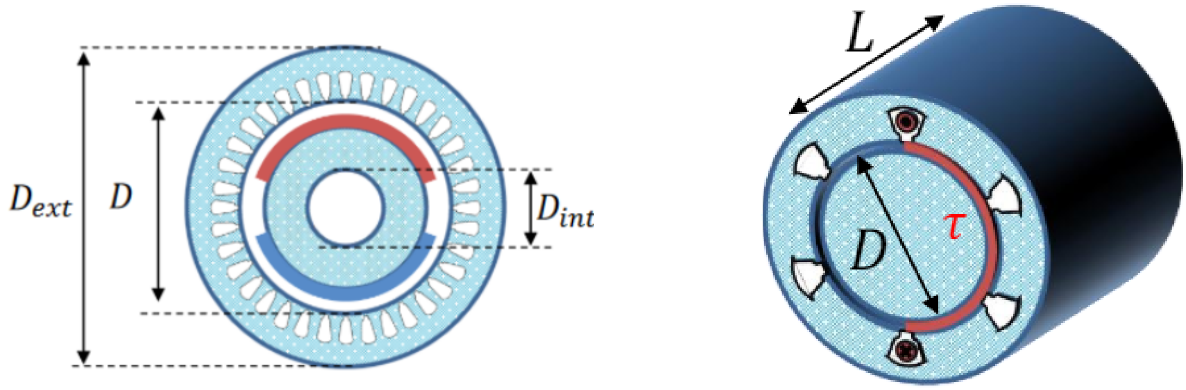

Figure 4.1: Motor dimensions

The parameters listed in table 4.1 constitute the fundamental design specifications of the machine, while a more extensive set of parameters was implemented within the FEMM environment for detailed electromagnetic analysis. FEMM is an industry-standard finite element analysis tool specifically developed for solving 2D simulations under steady-state conditions through the numerical solution of Maxwell's equations. In this thesis, particular attention was devoted to properly modeling the nonlinear B-H characteristics of the M250-35A electrical steel used in both the stator and rotor cores.

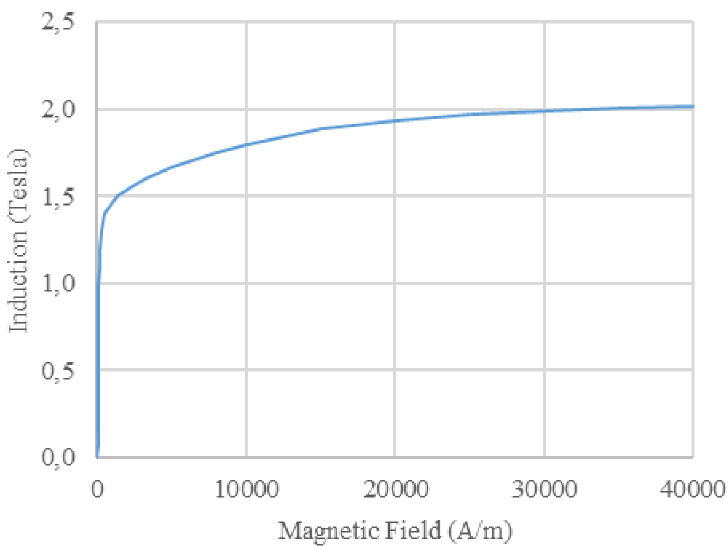

Figure 4.2: M250-35A BH curve for stator and rotor lamination [9]

The development of the FEMM model required careful consideration of magnetic non-linearities, making the principle of superposition inapplicable for this analysis. This nonlinear behavior significantly influences the machine's performance characteristics, particularly under saturated operating conditions. The software enables to capture these interactions by directly solving the field equations while accounting for the material's nonlinear permeability, allowing for accurate prediction of flux density distributions and local saturation.

Nominal current

In this thesis, no distinction is made between sectors 1 and 2 regarding the current reference; thus, the same target values are applied, i.e., $i_{da} = i_{db}$ and $i_{qa} = i_{qb}$. A Matlab script was developed to compute the intersection between the MTPA trajectory and the current circle. This intersection yields the exact values of the direct and quadrature current components under rated conditions. The resulting values correspond to the nominal operating point: $i_{d,\text{rat}} = -42.32\,\text{A}$ and $i_{q,\text{rat}} = 57.32\,\text{A}$.

Nominal speed

The dynamic equations of a three-phase motor in the dq reference frame are given in (1.33). Since in a dual-three-phase motor, the rotor is only one, it is easier to consider only one sector. Under steady-state conditions, the time derivatives of the fluxes can be neglected:

$$\frac{d\varphi_d}{dt} \approx 0, \quad \frac{d\varphi_q}{dt} \approx 0 \tag{4.1}$$

The (1.33) is now possible to write as:

$$\begin{cases} v_d = R_s \cdot i_d - \omega\varphi_q \\ v_q = R_s \cdot i_q + \omega\varphi_d \end{cases} \tag{4.2}$$

Solving for ω :

$$\omega = \frac{v_d - R_s i_d}{\varphi_q} = \frac{v_q - R_s i_q}{\varphi_d} \tag{4.3}$$

However, when the individual components v_d and v_q are unknown, but the magnitude of the voltage vector V_phase is known, is necessary to find an expression for ω in terms of V_phase and known parameters.
The magnitude of the voltage vector is given by:

$$\begin{gathered} V_\text{lim} = \frac{V_{DC}}{\sqrt{3}} \cdot 0.9 \\ V_\text{phase} = \sqrt{v_d^2 + v_q^2} \leq V_\text{lim} \end{gathered} \tag{4.4}$$

V_lim accounts for the inverter's modulation capability, as expressed in formula (1.71), typically 90% of the linear region of a sinusoidal PWM inverter.

Substituting v_d and v_q:

$$V_{\text{phase}}^2 = (R_s i_d - \omega\varphi_q)^2 + (R_s i_q + \omega\varphi_d)^2 \tag{4.5}$$

Expanding the squares:

$$V_{\text{phase}}^2 = (R_s i_d)^2 - 2R_s i_d \omega\varphi_q + \omega^2\varphi_q^2 + (R_s i_q)^2 + 2R_s i_q \omega\varphi_d + \omega^2\varphi_d^2 \tag{4.6}$$

Group terms by powers of ω:

$$V_{\text{phase}}^2 = R_s^2(i_d^2 + i_q^2) + \omega^2(\varphi_q^2 + \varphi_d^2) + 2\omega R_s(i_q\varphi_d - i_d\varphi_q) \tag{4.7}$$

Rearrange as a quadratic equation in ω:

$$\omega^2(\varphi_q^2 + \varphi_d^2) + 2\omega R_s(i_q\varphi_d - i_d\varphi_q) + R_s^2(i_d^2 + i_q^2) - V_{\text{phase}}^2 = 0 \tag{4.8}$$

Define coefficients:

$$\begin{aligned} a &= \varphi_q^2 + \varphi_d^2 \\ b &= 2R_s(i_q\varphi_d - i_d\varphi_q) \\ c &= R_s^2(i_d^2 + i_q^2) - V_{\text{phase}}^2 \end{aligned} \tag{4.9}$$

The solutions for ω are given by the quadratic formula, explicitly:

$$\omega = \frac{-2R_s(i_q\varphi_d - i_d\varphi_q) \pm \sqrt{[2R_s(i_q\varphi_d - i_d\varphi_q)]^2 - 4(\varphi_q^2 + \varphi_d^2)\left[R_s^2(i_d^2 + i_q^2) - V_{\text{phase}}^2\right]}}{2(\varphi_q^2 + \varphi_d^2)} \tag{4.10}$$

The physically meaningful solution is the positive root. Subsequently, the electrical angular speed must be converted into mechanical speed, resulting in a nominal operating condition of approximately 4464.7 rpm.

Nominal torque

Considering the torque expression derived for three-phase motors in equation (1.63), and noting that a dual three-phase motor effectively doubles the contribution, the resulting torque is exactly twice 72.31 Nm.

4.2 Inductance matrix of IPM motors and PI parameters

To understand the simplifications that can be applied in motor control, it is first necessary to analyze all inductance values present in equation (2.10). For this purpose, 3D plots are generated as a function of the currents i_d and i_q.
The first type of inductance examined in this thesis is the differential inductance matrix, which plays a critical role in the PI gain calculation, as presented in chapter 2. The corresponding formulas are valid under the assumption that the off-diagonal elements are negligible compared to the diagonal ones. Based on this assumption, several matrix manipulation techniques are applied. Ultimately, the apparent inductances are introduced for application in feedforward compensation.

Incremental inductances

The following presents the differential inductances obtained directly from the post-processing of the FEMM analysis, without applying any method aimed at diagonalizing the matrix.

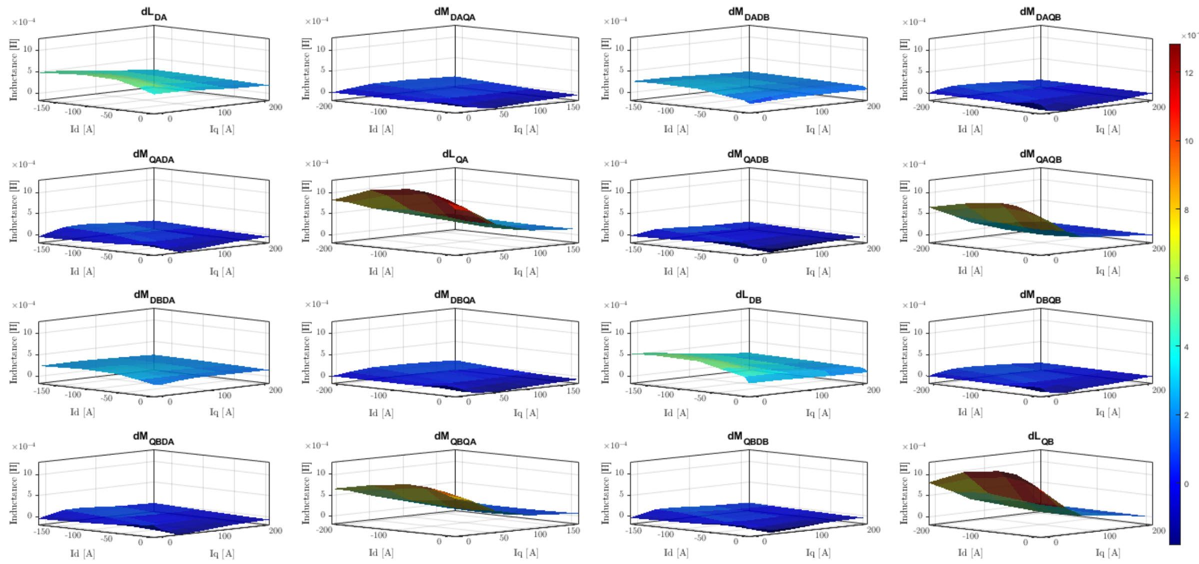

Figure 4.3: IPM - incremental inductances

The figure clearly shows that mutual inductance terms cannot be neglected, as the magnitudes of the self and mutual inductances are comparable. As a result, any model simplification that disregards mutual inductance contributions will lead to significant inaccuracies. This implies that it is not possible to simplify the model into the form presented in (2.43), which is typically employed to ease the calculation of the PI gains.
Another important observation is that the inductance values corresponding to the same axis L_{didj} or L_{qiqj} are significantly higher than those observed between different axes L_{diqj}

or L_{qidj}. Inductances measured along the same axis represent the direct magnetic coupling between coils aligned and excited in the same magnetic direction. In such configurations, the magnetic flux generated by one winding is effectively channeled and linked with the corresponding winding on the same axis due to favorable magnetic alignment. This results in stronger mutual coupling and, consequently, higher inductance values. On the other hand, inductances between different axes exhibit significantly weaker coupling. This is due to the orthogonal spatial separation of these axes by 90 electrical degrees, which causes their associated magnetic flux paths to intersect minimally. As a result, the mutual flux linkage between windings on different axes is greatly reduced, leading to much smaller inductance values in the cross-axis.

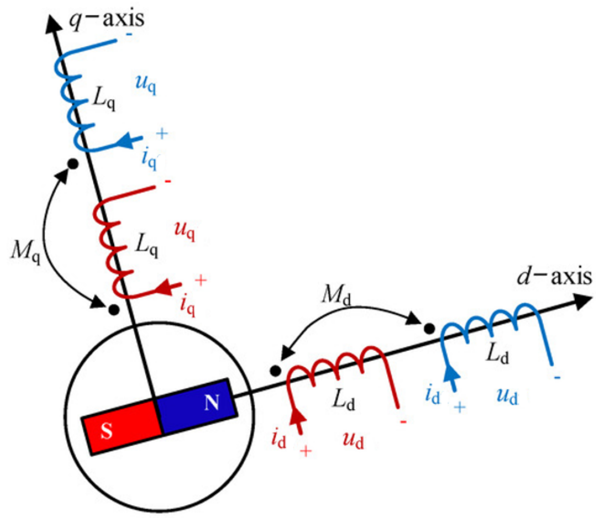

Figure 4.4: DQ axis for a dual-three-phase motor

Based on the inductance values presented in figure 4.14, and taking into account the nominal operating conditions of the machine, the relevant inductance parameters have been accurately determined. These values serve as the foundation for the subsequent tuning of the PI controller gains.

To evaluate and compare the effectiveness of two different tuning approaches, both methods were applied sequentially. The first method is based on the analytical formulation given by equation (2.39), while the second utilizes the alternative expression provided in equation (2.43).

Following the application of these methods, the corresponding proportional and integral gains were computed for each approach. The results are compiled and presented in the table below, enabling a clear comparison of the two proposed tuning strategies and highlighting their respective differences.

Parameters	**From** dL_{dq}	**From** dL_{dq}^{-1}
$dL_{d,a}$ [mH]	0.352	0.216
$dL_{q,a}$ [mH]	0.437	0.255
$dL_{d,b}$ [mH]	0.352	0.216
$dL_{q,b}$ [mH]	0.437	0.255
$K_{p,da}$	1.65	0.96
$K_{p,qa}$	2.07	1.16
$K_{p,db}$	1.65	0.96
$K_{p,qb}$	2.07	1.16
$K_{i,da}$	2227.29	1368.98
$K_{i,qa}$	2763.19	1610.92
$K_{i,qa}$	2225.62	1367.33
$K_{i,qb}$	2761.11	1611.66

Table 4.2: IPM - proportional and integral gains

Significant differences can be observed in both K_p and K_i values obtained through the two methods. A detailed simulation and performance analysis of each approach is presented in chapter 5, in order to determine which method yields superior control performance.

To have a better understanding of the inverse inductance matrix and to analyze the variation of the self-inductances terms, the inverse of the incremental inductance matrix is also plotted:

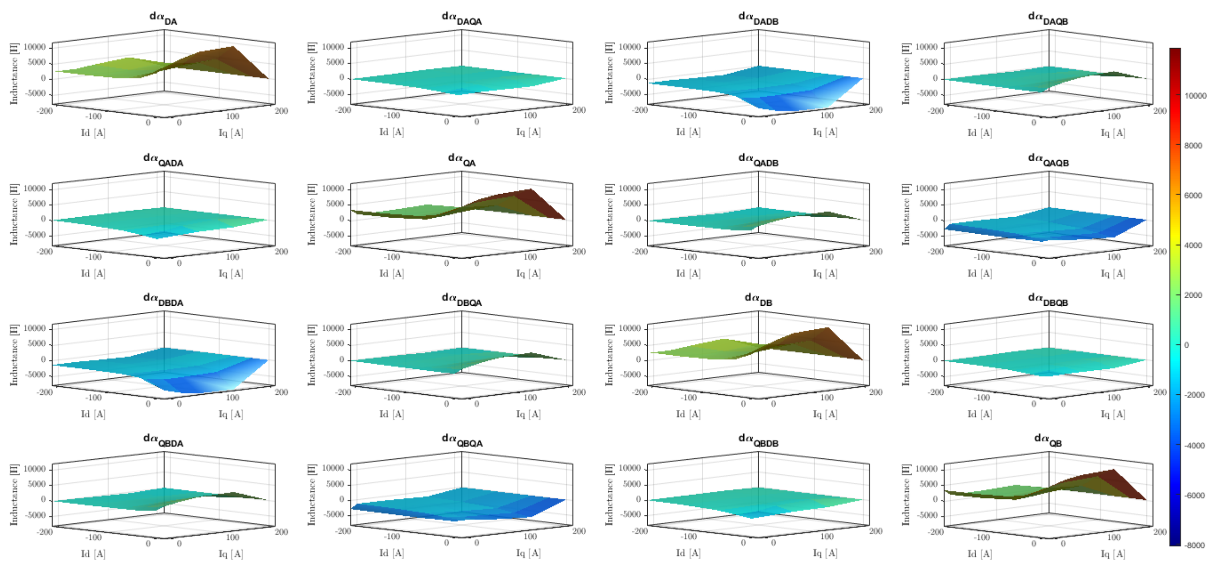

Figure 4.5: IPM - inverse incremental inductances

It is now the turn of the VSD method to analyze the differences. As discussed in the previous chapter, the machine equations within the VSD framework retain the same general form as presented in equation (2.60). The main difference lies in the structure of the inductance matrices:

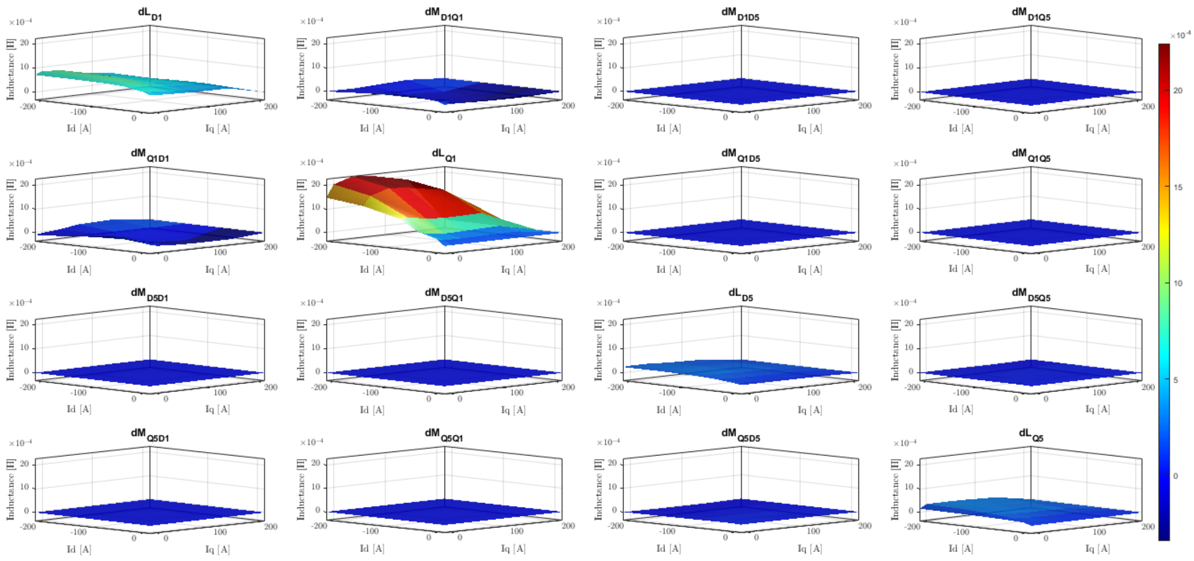

Figure 4.6: IPM - incremental inductances in VSD

In figure 4.6, it can be seen that the matrix is more diagonal compared to cases presented in figure 4.14 and 4.5, where the matrix element in plane 1 was significantly larger than that in plane 5. Consequently, the approximation used with the VSD method is more accurate.

A similar comparison to that proposed in the modular approach is also carried out using the VSD method:

Parameters	**From** dL_{vsd}	**From** dL_{vsd}^{-1}
$dL_{d,1}$ [mH]	0.563	0.514
$dL_{q,1}$ [mH]	0.710	0.649
$dL_{d,5}$ [mH]	0.141	0.137
$dL_{q,5}$ [mH]	0.164	0.158
$K_{p,d1}$	2.71	2.46
$K_{p,q1}$	3.45	3.14
$K_{p,d5}$	0.59	0.56
$K_{p,q5}$	0.70	0.67
$K_{i,d1}$	3556.94	3250.61
$K_{i,q1}$	4487.48	4101.05
$K_{i,d5}$	895.97	866.41
$K_{i,q5}$	1036.83	1002.60

Table 4.3: IPM - proportional and integral gains in VSD

In this table, it can be observed that the proportional and integral gains calculated using the two different methodologies are closer to each other compared to the case seen in the modular approach. This is because the inductance matrix is more diagonal, and therefore, the contribution of its inverse is less significant.

Apparent inductances

Apparent inductance plays a key role in implementing a feedforward compensation scheme. Ideally, all inductance terms should be taken into account to achieve the most accurate results. However, including this level of detail greatly increases the complexity of the control algorithm. It requires substantial memory to store detailed lookup tables and places heavy real-time computational demands. In practice, it is more efficient to include only those mutual inductance terms whose magnitudes are comparable to the self-inductances. If no mutual inductance terms meet this criterion, it is preferable to consider only the self-inductances.

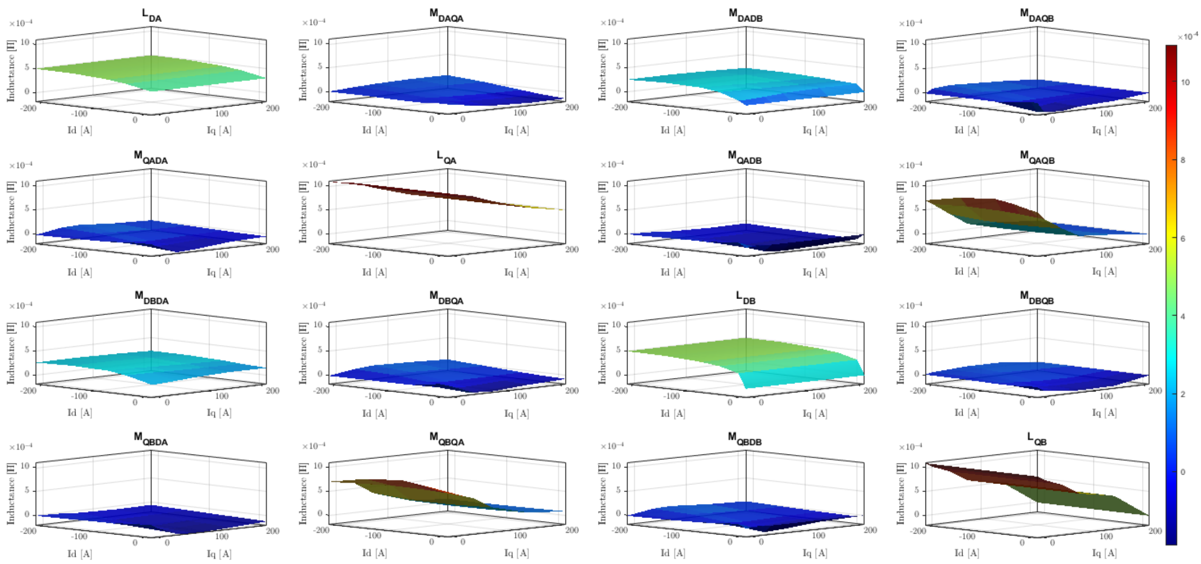

Figure 4.7: IPM - apparent inductance

As can be observed in the inductance maps, the mutual inductances, particularly those along the same axis, exhibit magnitudes comparable to the self-inductances. Therefore, for more effective feedforward compensation, it is essential to include at least the terms M_{QBQA} and M_{QAQB}.

Considering the application of the VSD approach to the feedforward scheme as well, the following differences can be observed:

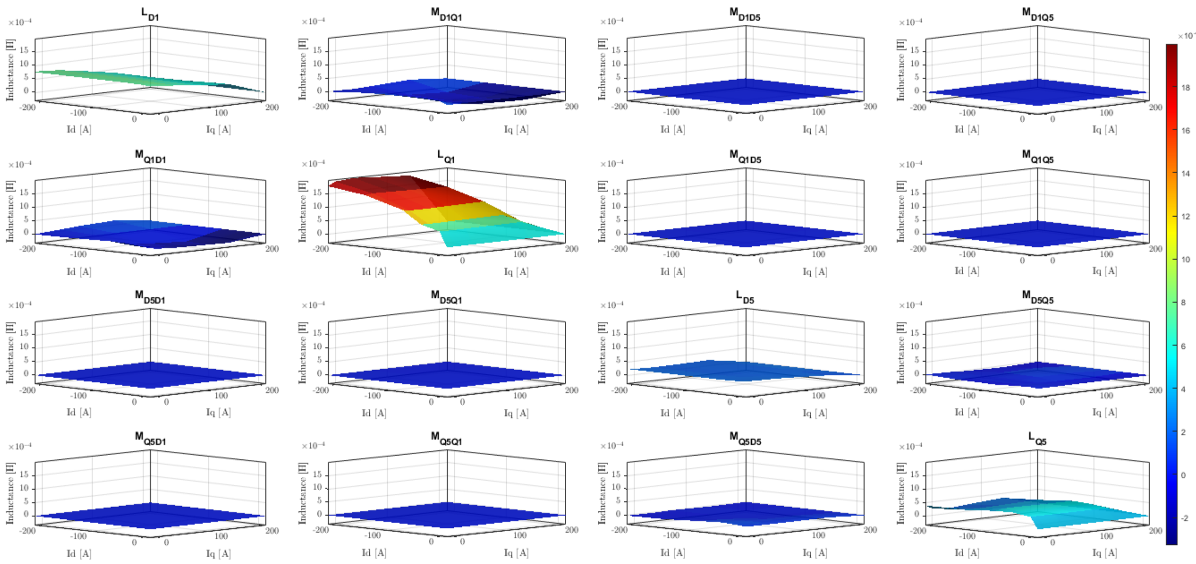

Figure 4.8: IPM - apparent inductances in VSD

In this case, the self-inductances are dominant compared to the mutual inductances, particularly L_{D1} and L_{Q1}. Therefore, the feedforward implementation using the VSD approach can be effectively carried out using only these two self-inductances, resulting in a fast system with minimal memory requirements.

Novel matrix transformation

As shown in (2.70), the only difference respect VSD lies in the sign change of the last row. Consequently, the variations in the inductance matrix are absent and minimal in the terms M_{D5Q5} and M_{Q5D5}. The graphs presented in the previous subsection are not reported again, as the results closely resemble those obtained using the VSD approach.

4.3 Inductance matrix of SPM motors with a linear B-H curve

In this section, an analysis of the inductances of an SPM machine is presented. The machine is considered under the assumption of a linear magnetic behavior, which provides a simplified foundation for the investigation of inductance characteristics.
The use of a linear B-H curve is motivated by several important considerations. First, it allows for a clear and intuitive understanding of the inductance behavior without the complexities introduced by nonlinear saturation. This simplification is especially valuable

in early-stage analysis, where the focus is on capturing the essential behavior of the machine. Second, in many practical scenarios, especially at low load conditions, the magnetic materials within an SPM machine operate in the linear region. Thirst, the computational time to simulate the FEA of the motor is reduced.

Apparent and incremental inductances

When linear magnetic behavior is assumed, the difference between apparent and incremental inductance becomes negligible. Both types of inductance exhibit nearly identical trends due to the linear dependence of the magnetic flux on the current.

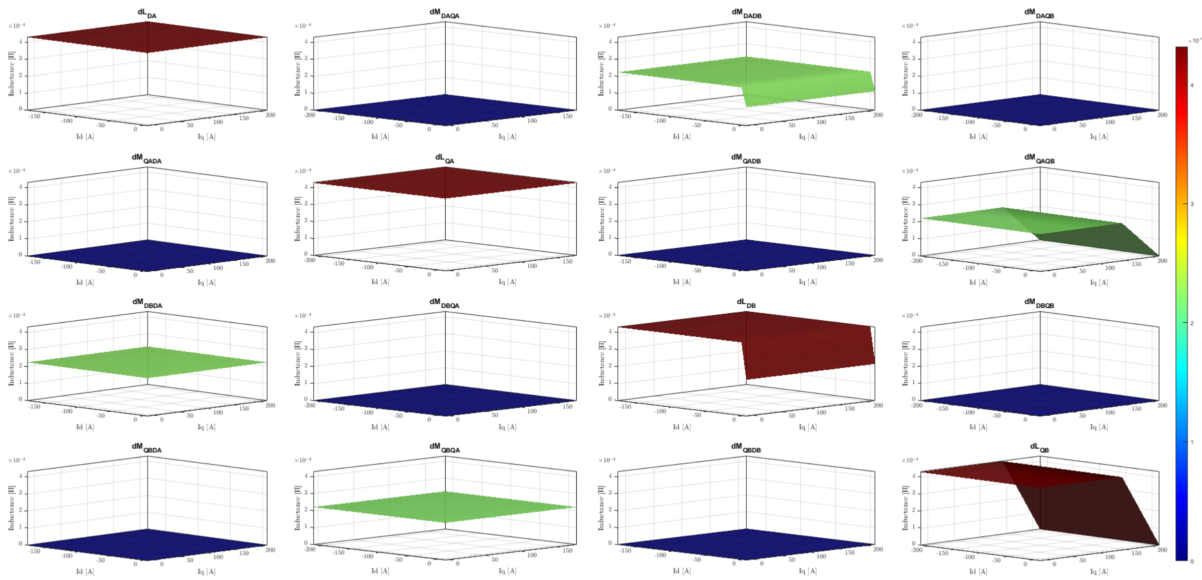

Figure 4.9: SPM linear BH curve - incremental inductances

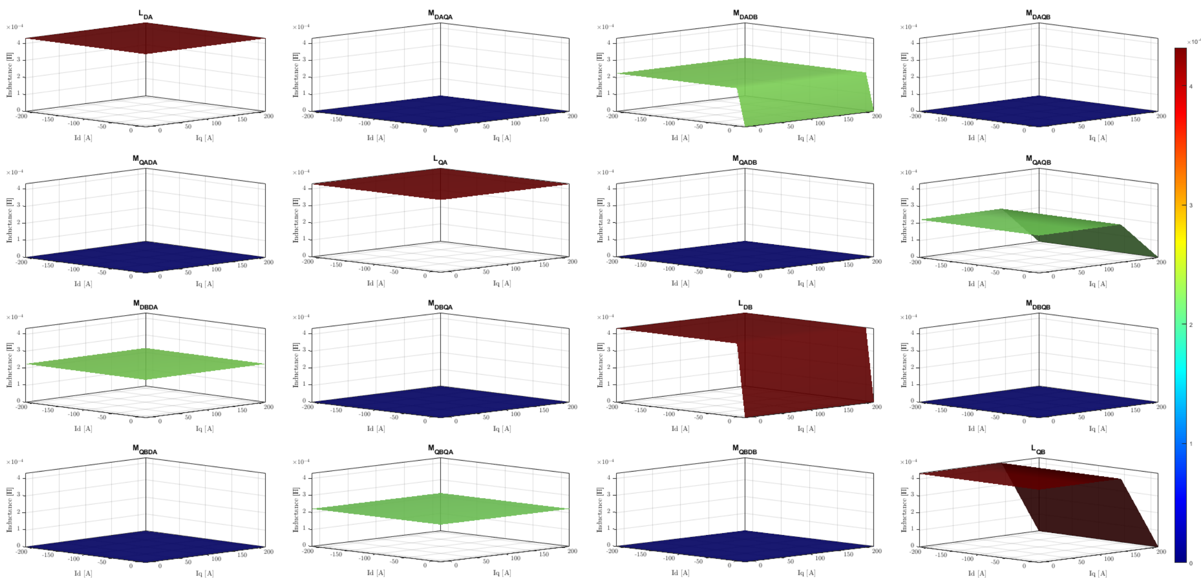

Figure 4.10: SPM linear BH curve - apparent inductances

Since the modeling of the linear system is presented only as a preliminary study, the following section is dedicated to the analysis of the nonlinear mapping. The inductance matrix shown here is used solely to highlight the differences between linear and nonlinear material mappings.

4.4 Inductance matrix of SPM motors with a non-linear B-H curve and PI parameters

After analyzing the motor assuming a linear magnetic material model, the study now progresses to incorporate a nonlinear *B-H* curve. This nonlinear characterization is particularly important when considering high current densities, as it allows for a more accurate understanding of magnetic saturation effects within the laminated materials.

Incremental inductances

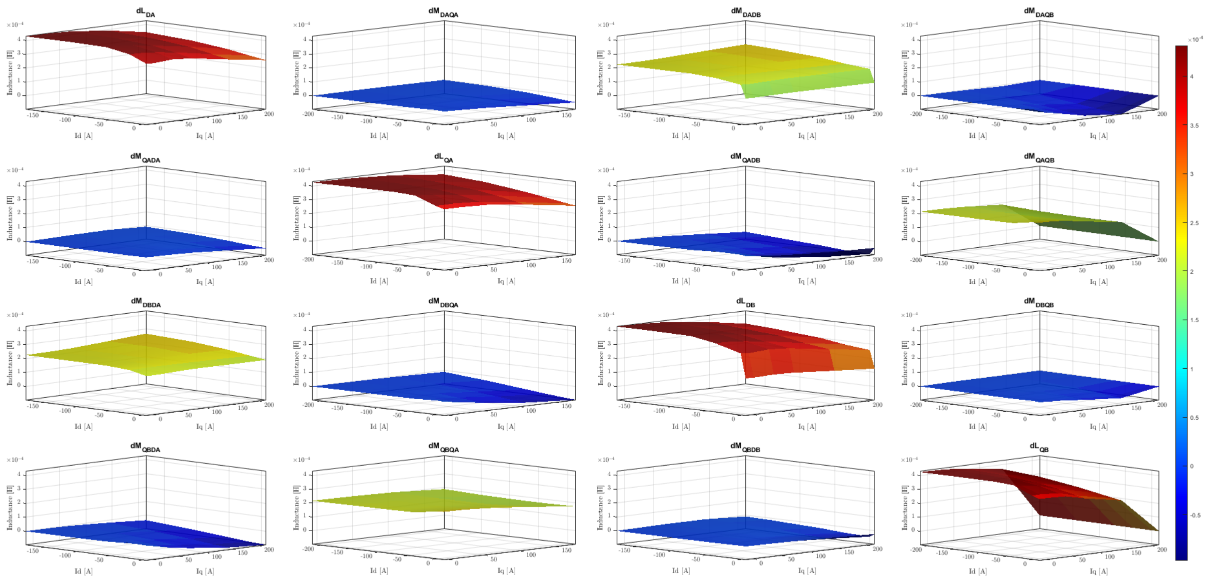

Figure 4.11: SPM non linear BH curve - incremental inductances

The figure shows that the mutual-inductance terms are smaller than the self-inductance terms. Furthermore, the difference between self and mutual inductances in the IPM motor is less pronounced compared to the larger disparity observed in the SPM motor. Another important observation is that the inductance values corresponding to the same axis, such as $L_{d_i d_j}$ or $L_{q_i q_j}$, are considerably higher than those between different axes, such as $L_{d_i q_j}$ or $L_{q_i d_j}$, a behavior also observed in the IPM motor.

Considering the nominal operating conditions of the machine, the inductances are obtained. By applying the two methods for calculating the PI gains, first using (2.39), and then (2.43), it is possible to summarize the parameters in the following table:

Parameters	From dL_{dq}	From dL_{dq}^{-1}
$dL_{d,a}$ [mH]	0.356	0.228
$dL_{q,a}$ [mH]	0.353	0.187
$dL_{d,b}$ [mH]	0.356	0.228
$dL_{q,b}$ [mH]	0.353	0.187
$K_{p,da}$	1.67	1.03
$K_{p,qa}$	1.65	0.82
$K_{p,db}$	1.67	1.02
$K_{p,qb}$	1.65	0.82
$K_{i,da}$	2251.84	1445.81
$K_{i,qa}$	2231.65	1182.46
$K_{i,db}$	2249.85	1444.19
$K_{i,qb}$	2232.59	1183.11

Table 4.4: SPM non linear BH curve - proportional and integral gains

Significant differences can be observed in both K_p and K_i values obtained through the two methods. A detailed simulation and performance analysis of each approach is presented in chapter 5, in order to determine which method yields superior control performance.

To have a better understanding of the inverse inductance matrix and to analyze the variation of the self-inductance terms, the inverse of the incremental inductance matrix is also plotted. This allows for a better comparison between different approaches presented in table 4.4.

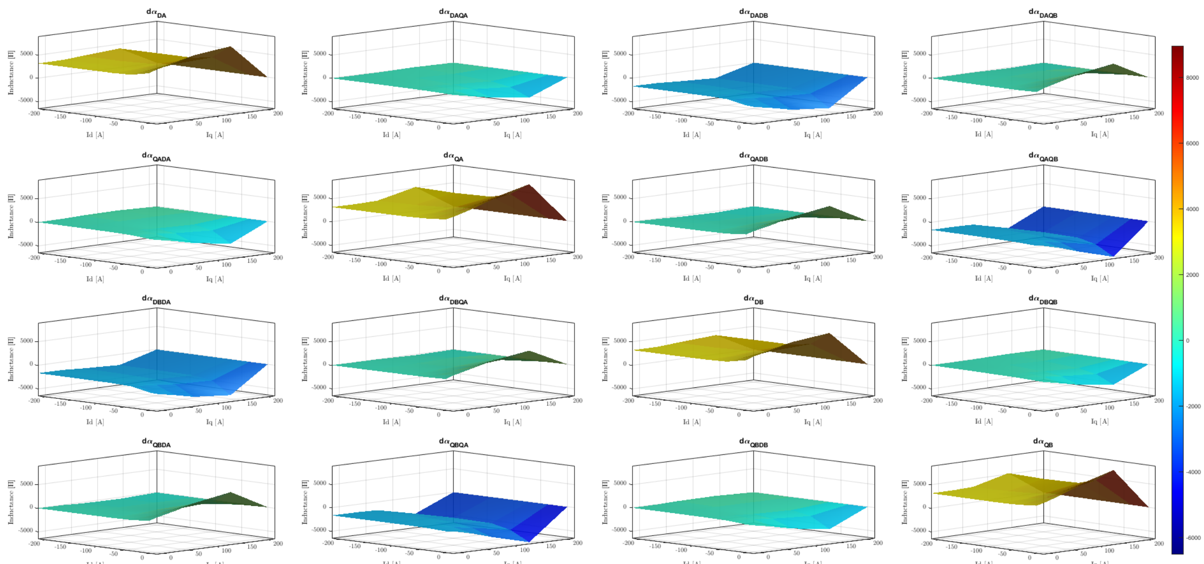

Figure 4.12: SPM non linear BH curve - inverse incremental inductances

It is now the turn of the VSD method to analyze the differences. As discussed in the previous chapter, the machine equations within the VSD framework retain the same general form as presented in equation (2.60). The main difference lies in the structure of the inductance matrices:

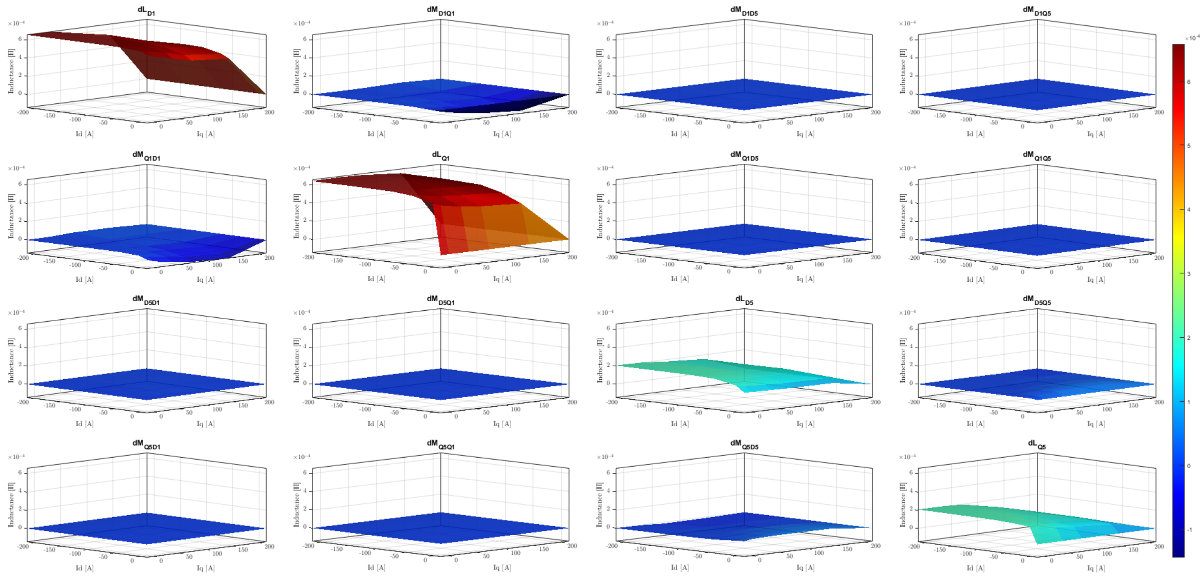

Figure 4.13: SPM non linear BH curve - incremental inductances in VSD

In the last figure, it can be seen that the matrix is more diagonal compared to the previous case, where the matrix element in plane 1 was significantly larger than that in plane 5. Consequently, the approximation used with the VSD method is also more accurate than the behavior presented in IPM motor.

A similar comparison to that proposed in the modular approach is also carried out using the VSD method:

Parameters	**"From"** dL_{vsd}	**"From"** dL_{vsd}^{-1}
$dL_{d,1}$ [mH]	0.563	0.554
$dL_{q,1}$ [mH]	0.595	0.585
$dL_{d,5}$ [mH]	0.153	0.143
$dL_{q,5}$ [mH]	0.122	0.113
$K_{p,d1}$	2.69	2.66
$K_{p,q1}$	2.84	2.81
$K_{p,d5}$	0.63	0.60
$K_{p,q5}$	0.48	0.44
$K_{i,d1}$	3537.30	3501.20
$K_{i,q1}$	3726.80	3683.00
$K_{i,d5}$	947.48	910.36
$K_{i,q5}$	757.99	704.52

Table 4.5: SPM non linear BH curve - proportional and integral gains in VSD

In this table, it can be observed that the proportional and integral gains calculated using the two different methodologies are closer to each other compared to the case seen in the modular approach. This is because the inductance matrix is more diagonal, and therefore, the contribution of its inverse is less significant.

Apparent inductances

Apparent inductance plays a key role in implementing a feedforward compensation scheme. Ideally, all inductance terms should be taken into account to achieve the most accurate results. However, including this level of detail greatly increases the complexity of the control algorithm, so in practice, it is more efficient to include only those mutual inductance terms whose magnitudes are comparable to the self-inductances.

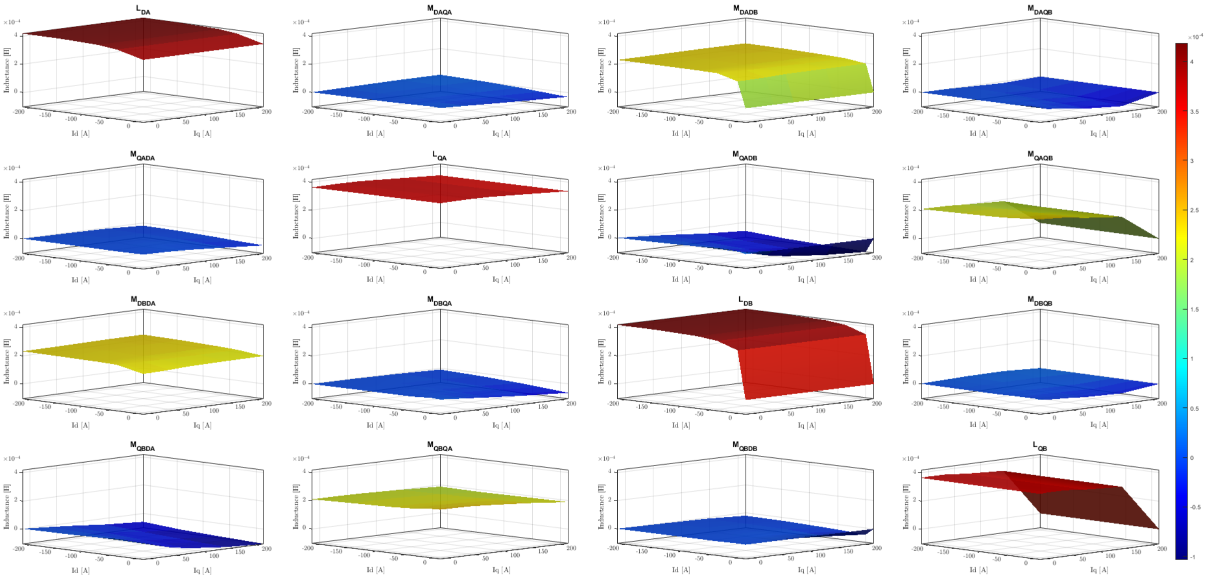

Figure 4.14: SPM non linear BH curve - apparent inductances

As can be observed in the inductance maps, the mutual inductances, particularly those along the same axis, exhibit magnitudes comparable to the self-inductances. Therefore, for more effective feedforward compensation, it is essential to include at least the terms M_{QBQA},M_{QAQB},M_{DADB} and M_{DBDA}.

Considering the application of the VSD approach to the feedforward scheme as well, the following differences can be observed:

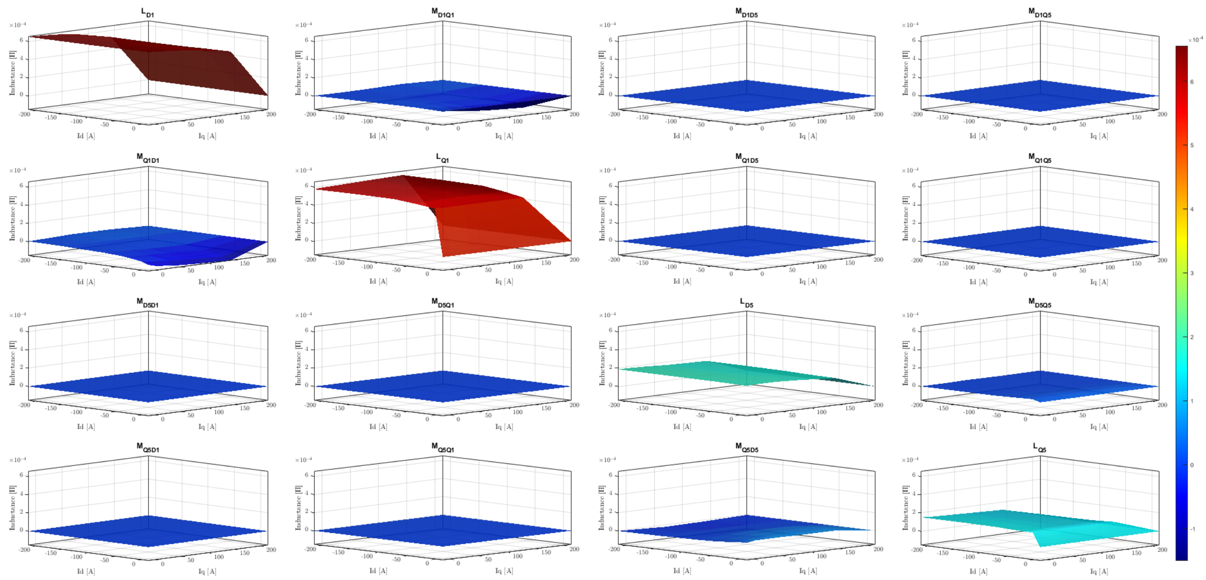

Figure 4.15: SPM non linear BH curve - apparent inductances in VSD

In this case, the self-inductances are dominant compared to the mutual inductances, particularly L_{D1} and L_{Q1}. Therefore, the feedforward implementation using the VSD approach can be effectively carried out using only these two self-inductances, resulting in a fast system with minimal memory requirements.

Chapter 5

Simulink model

Throughout this thesis, the work is developed progressively in stages. It begins with the most comprehensive model, the IPM motor, where all relevant aspects described in the previous chapters are considered. The next stage involves a SPM motor, allowing for a comparison and better understanding of the differences. The simulation scheme for all the motor models remains the same, with the only variation being the mapping output obtained from FEMM.

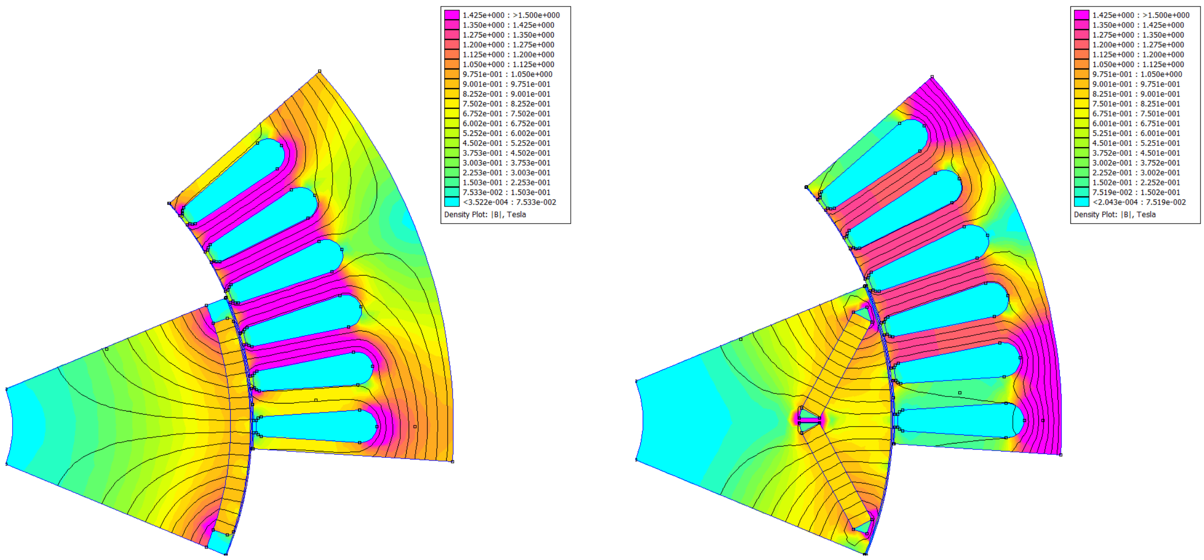

Figure 5.1: Comparison of flux density saturation in SPM and IPM

Both motors use the same materials and geometry, except for the stator yoke. In the SPM motor, the stator yoke is larger because the material tends to saturate more easily compared to the IPM design. Another difference lies in the magnet position: by definition, the magnet is placed on the surface in the SPM motor, while it is embedded in the IPM motor. The magnet thickness and area are maintained the same in both configurations to allow for a consistent and meaningful comparison between the two motors.

5.1 General scheme

The reference current used in the current control loop comes from two possible sources: the nominal current or the output of the speed controller (figure 5.2). The speed controller operates by comparing the measured speed with the reference speed to determine the required torque. Alternatively, the torque demand can be directly defined within a selected torque interval. In all the scenarios, the resulting torque is fed into a LUT that implements the MTPA strategy.

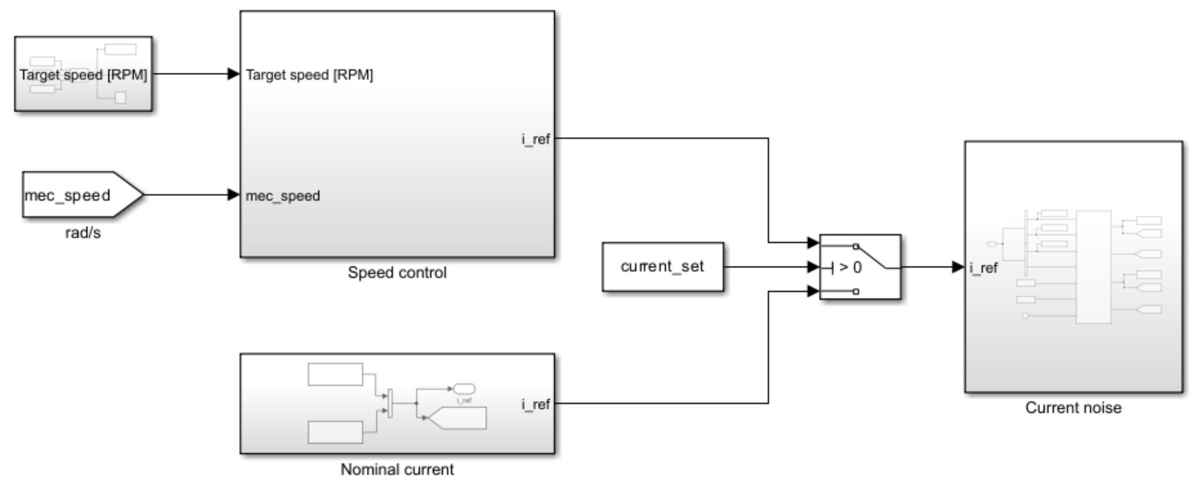

Figure 5.2: Selection of the reference current

A closer examination of the speed control subsystem reveals a block diagram that represents the equation discussed in chapter 1.1.3:

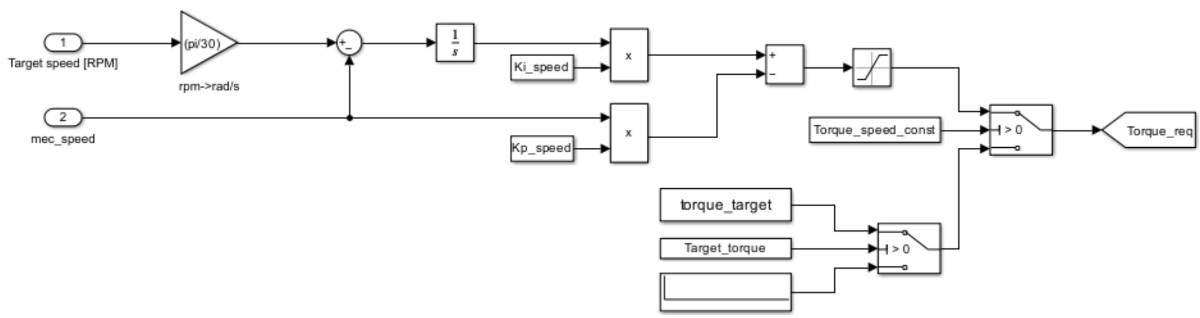

Figure 5.3: Speed control scheme

The output of the speed control is a torque request, which is converted into reference current, supposing that the two sectors have exactly the same characteristics:

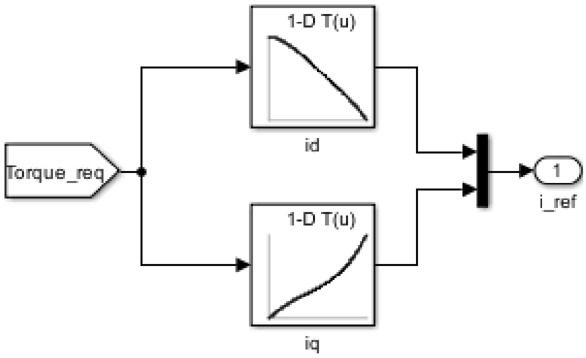

Figure 5.4: LUTs with torque request as input and current under MTPA as output

With the reference current now established for all sectors, a Matlab function is introduced to inject a current disturbance into the d-axis current. This function allows for the selective application of the disturbance, either in a single sector or across both sectors. The purpose of this disturbance is to evaluate the system's response to such variations.

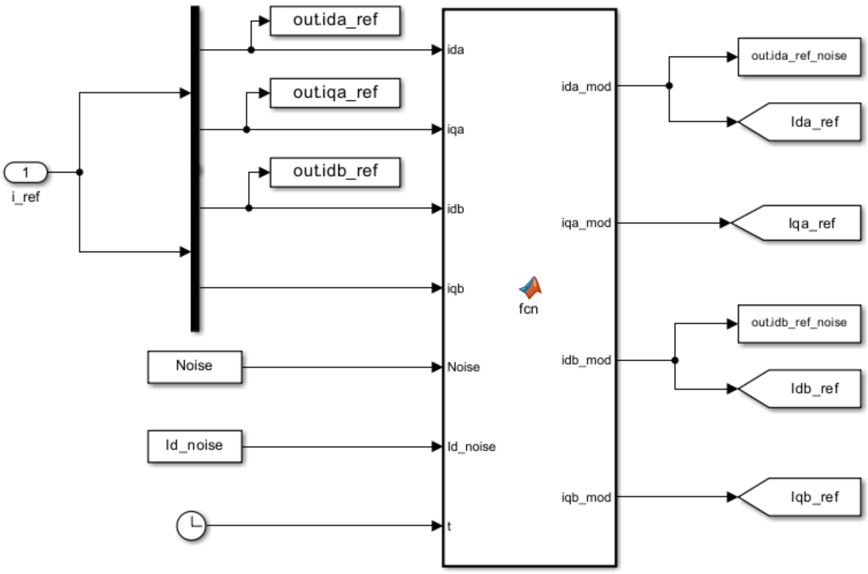

Figure 5.5: Current noise

After identifying the source of the reference current, the next step is to analyze the key subsystem that encompasses current control, machine model, and motor outputs. This last subsystem provides access to important values such as electromagnetic torque, flux components, and stator currents, represented in both the dq and abc reference frames.

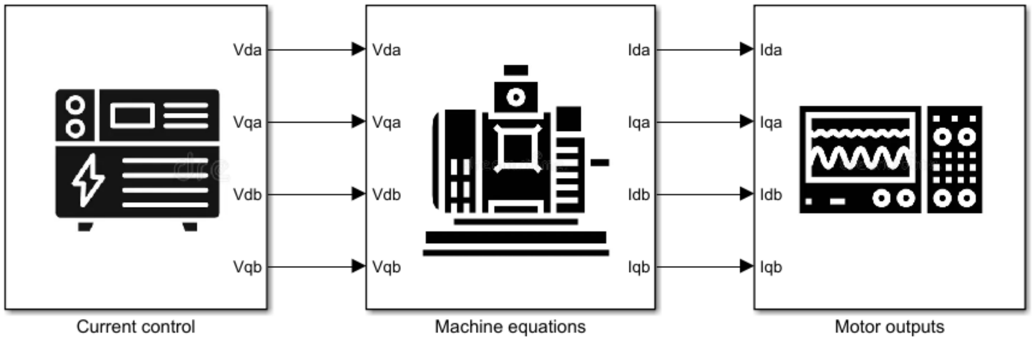

Figure 5.6: Overall system

Referring to figure 5.6, the analysis begins with the current control loop. Based on the equations developed in chapter 2.2.1, the control algorithm is implemented in the simulation environment, employing two different methods for extracting the diagonal elements used in the computation of the control gains.

The differential inductance matrix, which for each term represents a five-dimensional tensor $(i_{da}, i_{qa}, i_{db}, i_{qb}, \theta)$, is implemented in Simulink using LUTs. Since the angular position dependency can be neglected, a Matlab script is used to average each term of the differential inductance tensor over the fifth dimension. As a result, the LUTs accept the target current for each sector and a generic angular position as input, which is necessary to fulfill the fifth input dimension but remains constant due to the averaging process.

All differential inductances are processed within a Matlab function that calculates the inductances, which are then used to determine the proportional and integral gains. This function includes two separate path: one that directly extracts the diagonal elements of the matrix **dLdq**, and another that first computes the inverse of **dLdq** and then extracts the diagonal elements from the resulting matrix. In this second method, the reciprocal of each diagonal term is taken to calculate the PI gains.

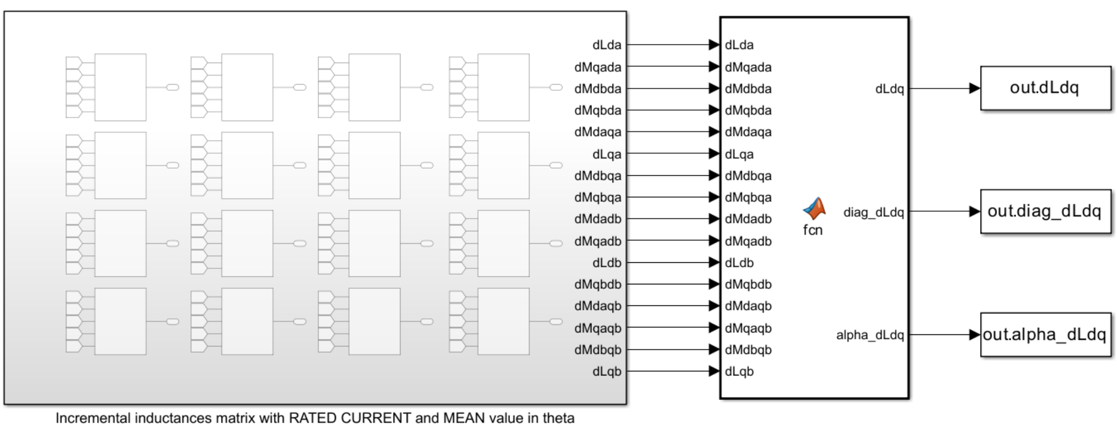

Figure 5.7: Simulink scheme for obtain $\mathbf{dL_{dq}}$ and $\boldsymbol{\alpha_{dq}}$

This Simulink presented runs before the main model, as the parameters K_p and K_i must be initialized prior to the start of the simulation. This setup is essential because this thesis also analyzes the control behavior under different tuning conditions, which vary depending on the motor current.

The next step, referring to the figure 5.8, consists of analyzing the current control loop, which represents the inner layer of the hierarchical control architecture. In the initial stage of this work, a modified PI controller is designed. This controller also incorporates a feedforward compensation mechanism that accounts for all mutual inductance terms. This feature can be optionally enabled or disabled to evaluate its impact on the system's performance.

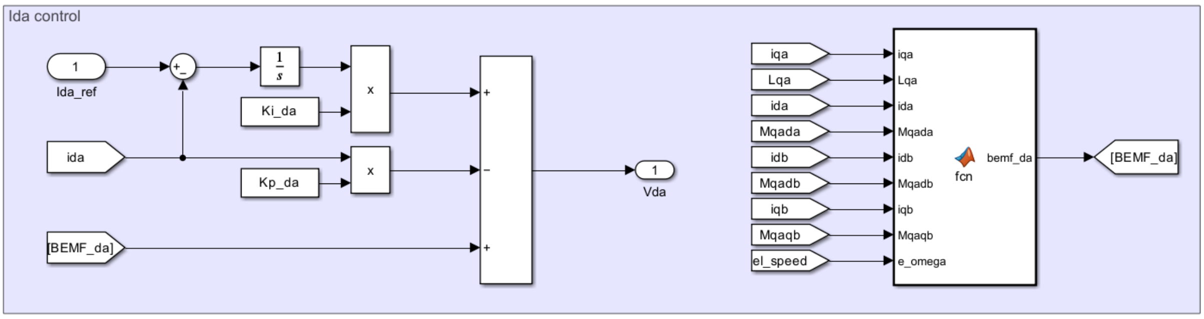

Figure 5.8: Current control for i_{da} axis

The tuning of the PI controller is carried out based on the desired control bandwidth, which is defined as follows:

$$\omega_c = \frac{2\pi f_{sw}}{D_f} \tag{5.1}$$

where $f_{sw} = 10000$ Hz denotes the switching frequency of the power converter.
A key reason for dividing by D_f rather than using only the numerator value lies in the separation of dynamic responses between the controller and the system. By selecting a control frequency significantly lower than the fundamental frequency of the system, the controller is designed to operate on a much slower time scale. This ensures that the PI controller does not attempt to react to fast dynamics. As a result, the risk of interacting with high-frequency components or creating undesired oscillations is minimized. This conservative tuning approach contributes to system stability and improves robustness against measurement noise and unmodeled high-frequency dynamics, also because the phase margin depends on this parameter.

In the following, the system is tested under minimum operating conditions using the modified PI controller with the IPM machine. The results obtained by using $D_f = 50$ as the denominator in equation (5.1) are presented below:

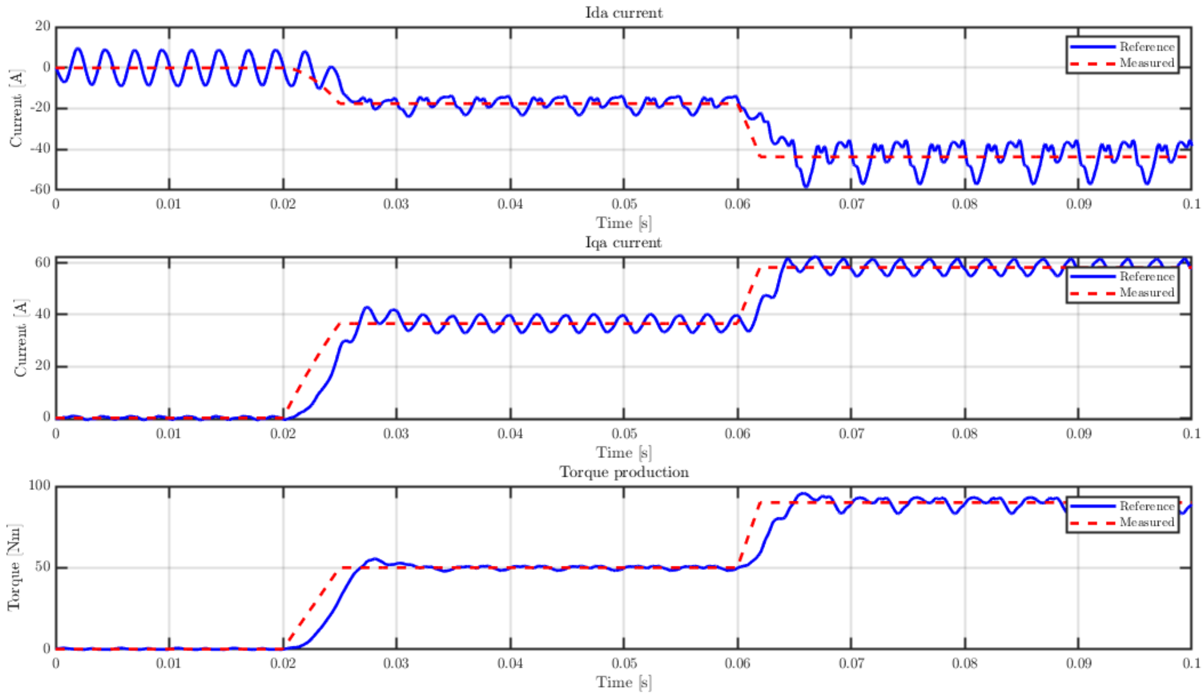

Figure 5.9: Division factor of 50

An increase in ω_c, which corresponds to a decrease in the denominator constant, results in a faster system response. However, if the selected value is too small, the proportional and integral gains become excessively large, potentially causing numerical instability and simulation failure.

The following test is performed with $D_f = 25$:

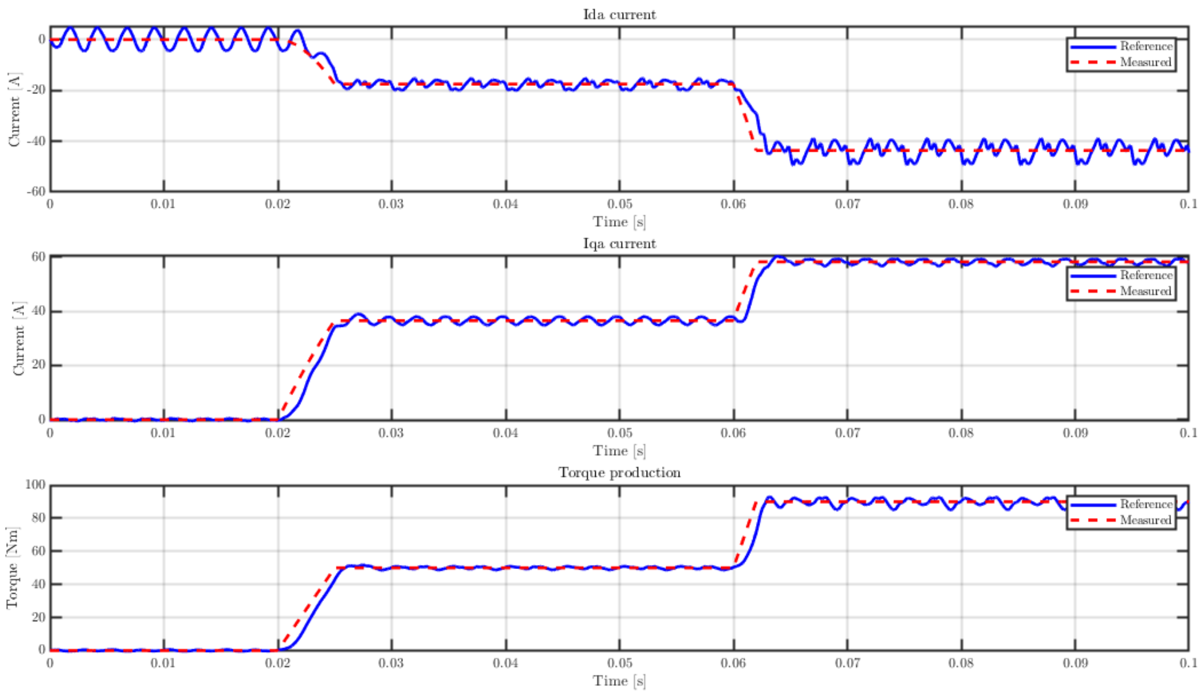

Figure 5.10: Division factor of 25

A comparison of figures 5.9 and 5.10 clearly shows that the second configuration delivers a faster dynamic response for both current and torque. Furthermore, it significantly reduces oscillations, making this second dominant factor the preferred choice.

The scheme shown in figure 5.8 is also implemented using a Matlab function, and the results are compared to verify the correctness of the system neglecting in this first part the feedforward compensation. This validation is particularly important because the same control strategy is used in the open-loop implementation of the state-space model and for VSD control.

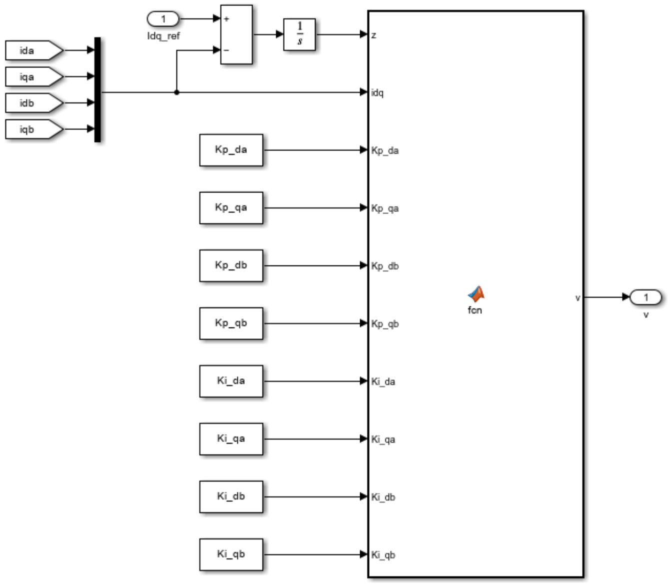

Figure 5.11: Current control using Matlab function

By using the control scheme implemented in figure 5.11, adapting the system to employ a VSD method becomes straightforward. This requires only updating the K_p and K_i parameters and introducing three Matlab functions to perform the transformations T_{vsd} between the dq and VSD reference frames.

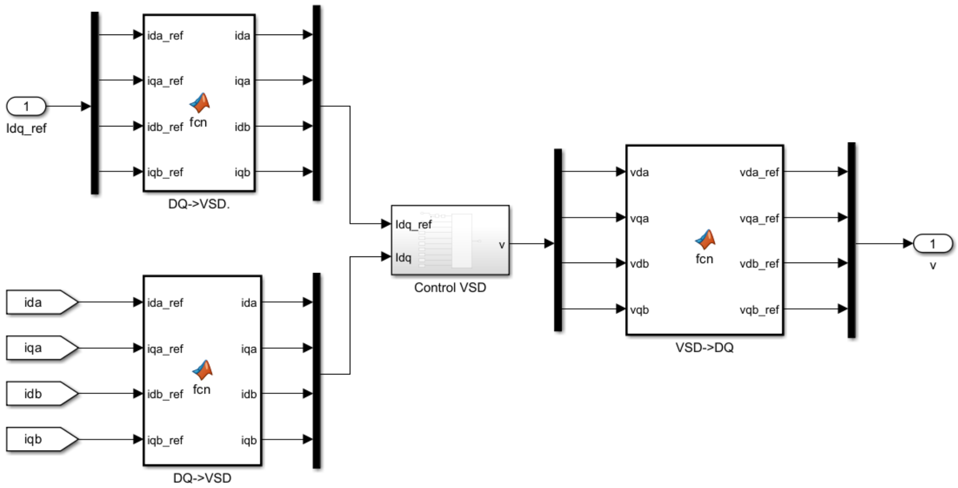

Figure 5.12: Current control using VSD

In the modeling and simulation of motor control systems, two distinct approaches can be adopted depending on the level of fidelity and the simulation objectives:

- **Ideal voltage injection:**
  This approach directly applies the reference voltages obtained from the control algorithm to the motor model, bypassing the physical modeling of the inverter and the PWM generation. However, this method does not account for switching effects, voltage ripple, or hardware-induced delays, and therefore may lead to overly optimistic results when compared to physical implementation;

- **Realistic switching model:**
  In this configuration, the inverter is modeled using switching devices controlled by a PWM signal generated from the reference voltages.

Since the primary objective of this thesis is to analyze the control strategy, the PWM generator and inverter are not modeled. As a result, the voltage outputs from the control blocks (5.8) and (5.12) are applied directly to the motor model. Within this setup, it is possible to choose between using a continuous or discrete PI controller for current regulation:

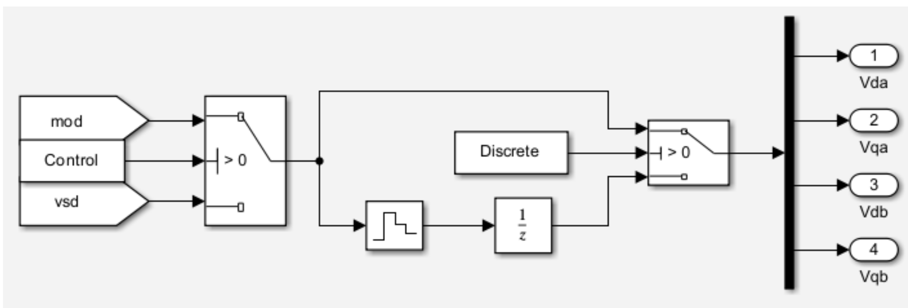

Figure 5.13: Continuous or discrete control

The motor is modeled according to equation (2.37), where the derivative of the current is explicitly isolated and then integrated. This approach is preferred over directly isolating the current itself because numerical integration is more stable and reliable than differentiation. As can be observed from the machine equations, current terms appear both as derivatives and algebraic variables. Therefore, the first step is to obtain the current derivatives, then integrate them, and use the resulting current values as inputs for the subsequent simulation step. In the initial iteration, the current is assumed to be zero; however, this does not pose an issue since the resistance R$_s islowandthecurrentincreasesgraduallywhenthemotorstartsfromrest.$
$Forsimplicityandimprovedaccuracy, sincethebehavioroftheflux with respect to the angular position isw$

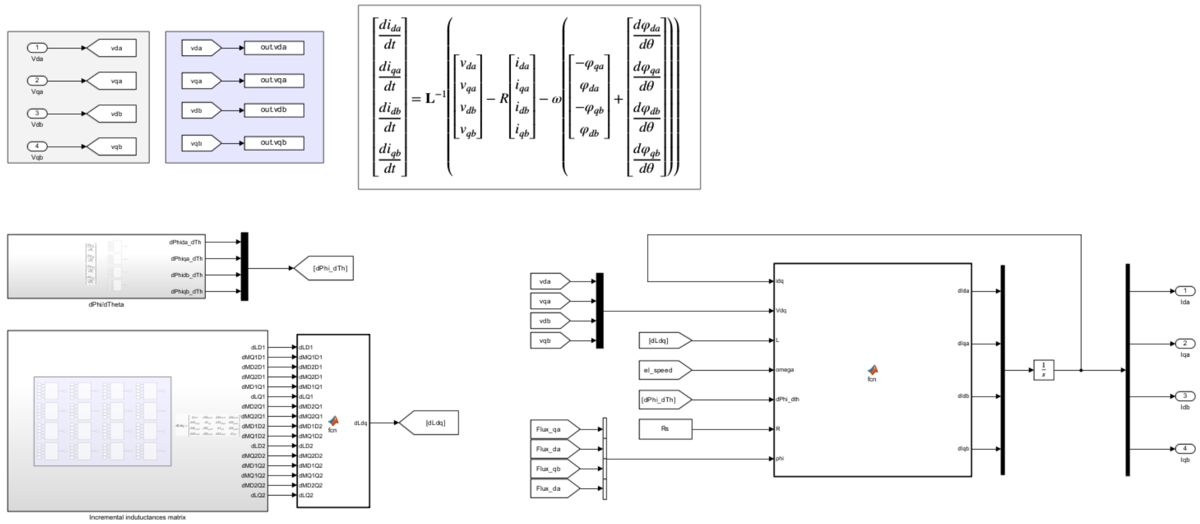

Figure 5.14: Machine equation

The current output from this block is fed into the motor output (figure 5.6), which internally computes all parameters derived from FEMM analysis and post-processing calculations. To evaluate the torque, two approaches are employed based on the following:

- Mathematical formula:

$$T_e = \frac{3}{2}P\left[(\varphi_{d1}i_{q1} - \varphi_{q1}i_{d1}) + (\varphi_{d2}i_{q2} - \varphi_{q2}i_{d2})\right] \tag{5.2}$$

  Where the fluxes come directly from the FEMM output. These data are inserted inside LUT, as can be seen in the following:

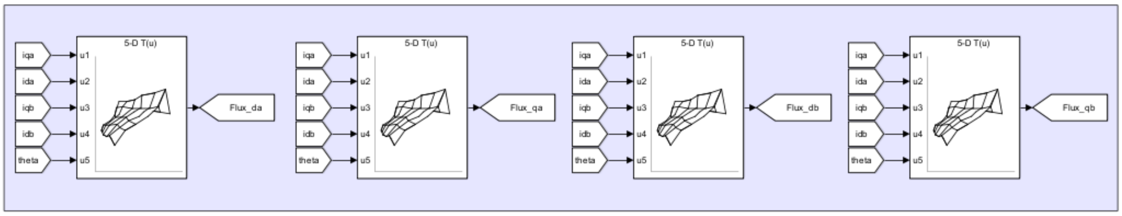

Figure 5.15: Flux from LUT

- The other method that is used is to extract the torque directly from the FEMM:

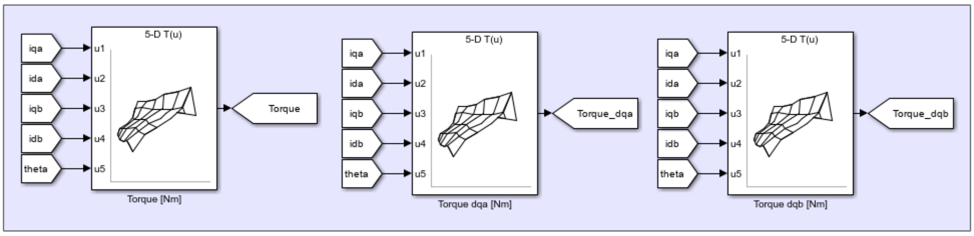

Figure 5.16: Torque from LUT

The first method exhibits reduced torque oscillations compared to those obtained from FEMM simulations, as it limits electromagnetic irregularities by producing a smoother current waveform through the motor controller. Therefore, it is more appropriate to consider the torque derived from post-processing the data obtained from FEMM.

To determine the position and velocity of the motor, the torque equation is employed, given that the moment of inertia is known. The motor's position is then obtained by integrating the velocity over time.
This scheme also allows for the application of an external load, which can be either constant or time-varying (e.g., an impulse) to test the velocity control. Furthermore, it can simulate a fixed rotational speed, similar to conditions found in a bench test.

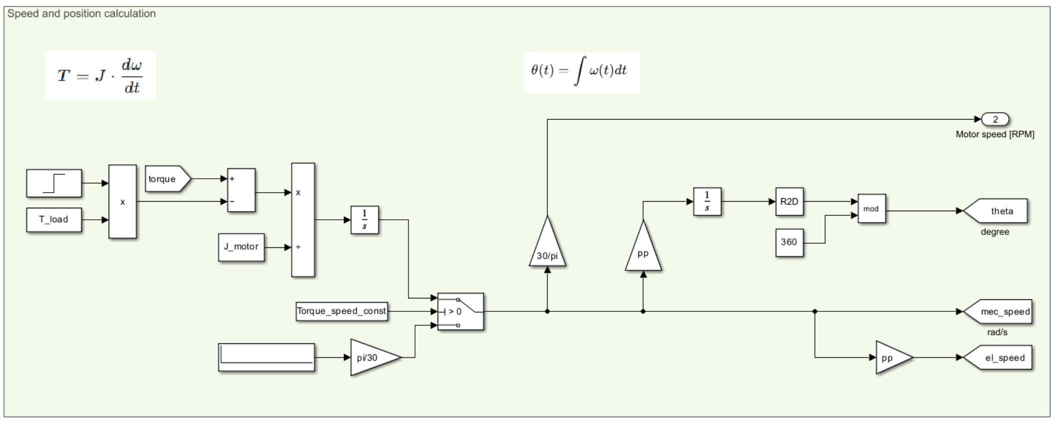

Figure 5.17: Speed and position of the rotor

5.2 State space

To understand the stability of a MIMO system, it is necessary to use a state-space representation. In the simulations presented in this chapter, the motor speed is set to 100 rpm in order to reduce the frequency of the current ripple. This choice facilitates a clearer analysis of the system's response, particularly in terms of control speed and overshoot.

5.2.1 Open loop

In this subsection, the current control system and the plant, as previously introduced, are described in an open-loop state-space configuration, as presented in section 3.3.2. Particular emphasis is placed on highlighting the differences between the previously discussed method and the current approach. This configuration serves as the foundational setup for implementing various feedforward compensation strategies and testing different PI controller configurations.

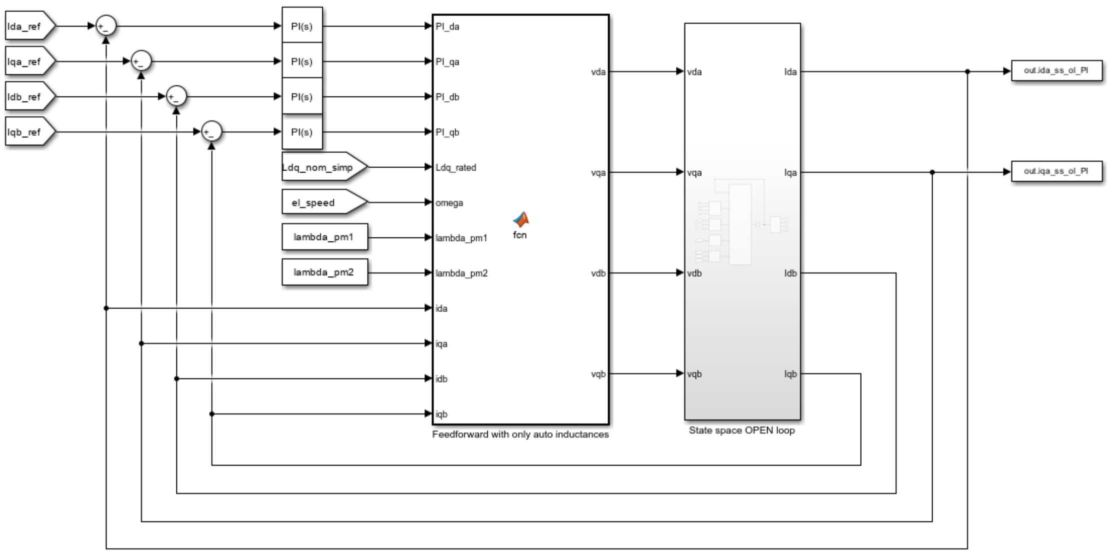

Figure 5.18: Motor model with feedforward compensation (only self-inductances) and modified PI

The classical PI controller is tuned using the same bandwidth of 2513 rad/s as that used for the modified PI, with a phase margin set to 75°.

The open-loop state-space model of the motor, presented in figure 5.18, is implemented using a Matlab function that encodes the equations described in (3.3.2):

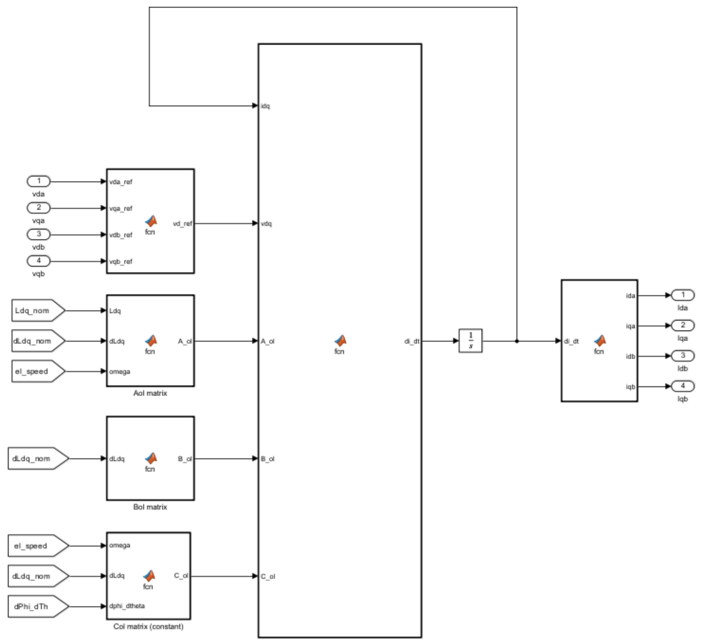

Figure 5.19: State space present in figure 5.18

The model presented in figure 5.18 serves as the primary framework. After generating a copy of this model, different feedforward compensation strategies are simulated: (1) no feedforward compensation, (2) compensation using only self-inductances selected at nominal current, (3) compensation with self-inductances selected with the motor current, and (4) feedforward incorporating both self and mutual inductances at nominal current. Subsequently, this comparison is extended to evaluate different current control strategies: the conventional PI controller, the modified PI controller, and the autotuning PI controller.

Real time PI controller auto tuning

The auto-tuning process used in Simulink consists of the following steps:

1. **Initial setup:** the PI controller is initialized with fixed gain values, which are stored in memory;

2. **Tuning activation:** when the signal entering the start/stop port is 1, the autotuning algorithm initiates the tuning procedure;

3. **System excitation:** the block injects small-amplitude sinusoidal signals into the plant, exciting the system dynamics across the chosen frequency range;

4. **System identification:** the plant's output response is analyzed to estimate a simplified model of the system;

5. **PI parameter computation:** based on the identified plant model and predefined control objectives (e.g., desired bandwidth and phase margin), the autotuner computes proportional and integral gains;

6. **Controller update:** the newly computed gains are saved in memory and are then applied to the PI controller.

The Simulink scheme that allows for auto-tuning of the PI is illustrated in the following:

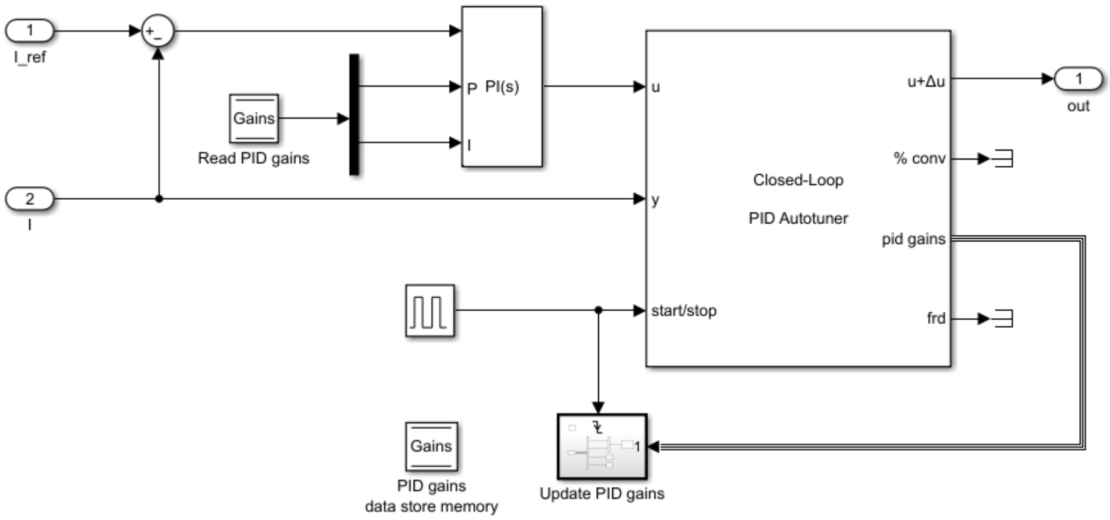

Figure 5.20: PI autotuner scheme

After analyzing how the autotuner scheme operates, the following image provides a visual representation of its main parameters and workflow. The process begins with the injection of a disturbance signal, which is triggered when the input to the start/stop control is set to 1. This action initiates the autotuning sequence, during which harmonic signals are injected into the system to evaluate its dynamic response.

Once the excitation phase is complete, indicated by the transition of the start/stop signal from 1 to 0, the autotuner processes the system's response to compute appropriate values for the proportional (K_p) and integral (K_i) gains. These calculated parameters are then automatically updated and stored in memory, allowing the controller to adapt to the system's characteristics without manual tuning.

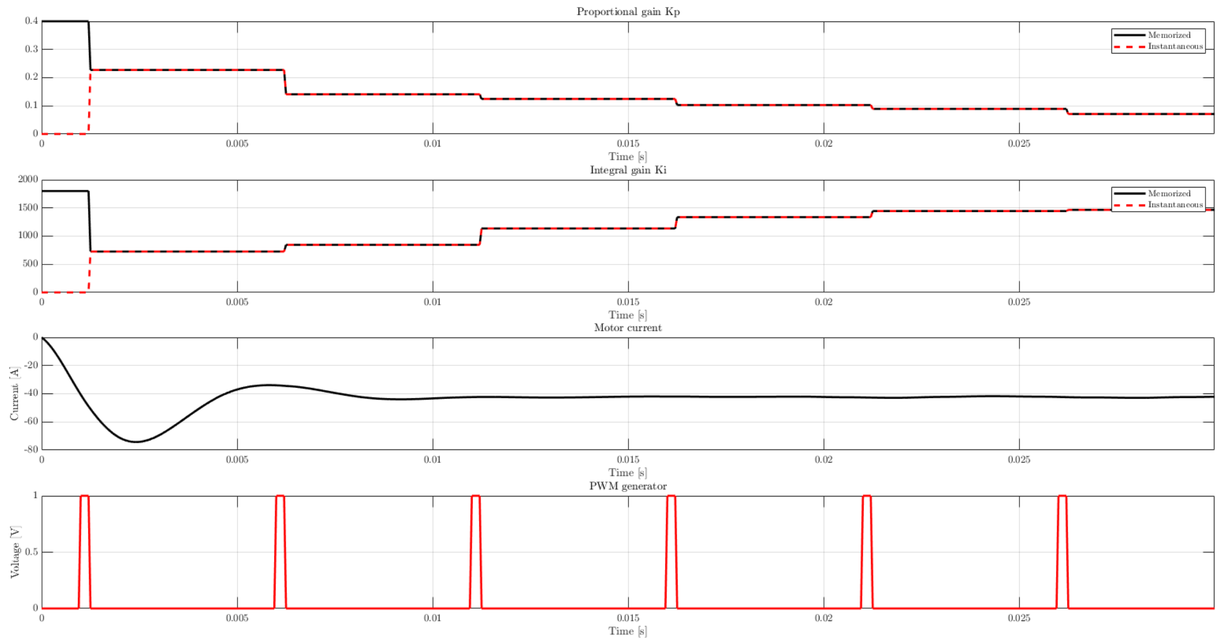

Figure 5.21: Main parameters used in PI autotuner for the d_a axis

5.2.2 Closed loop

The closed-loop state-space model described in subsection 3.3.3 is implemented here using a Simulink schematic:

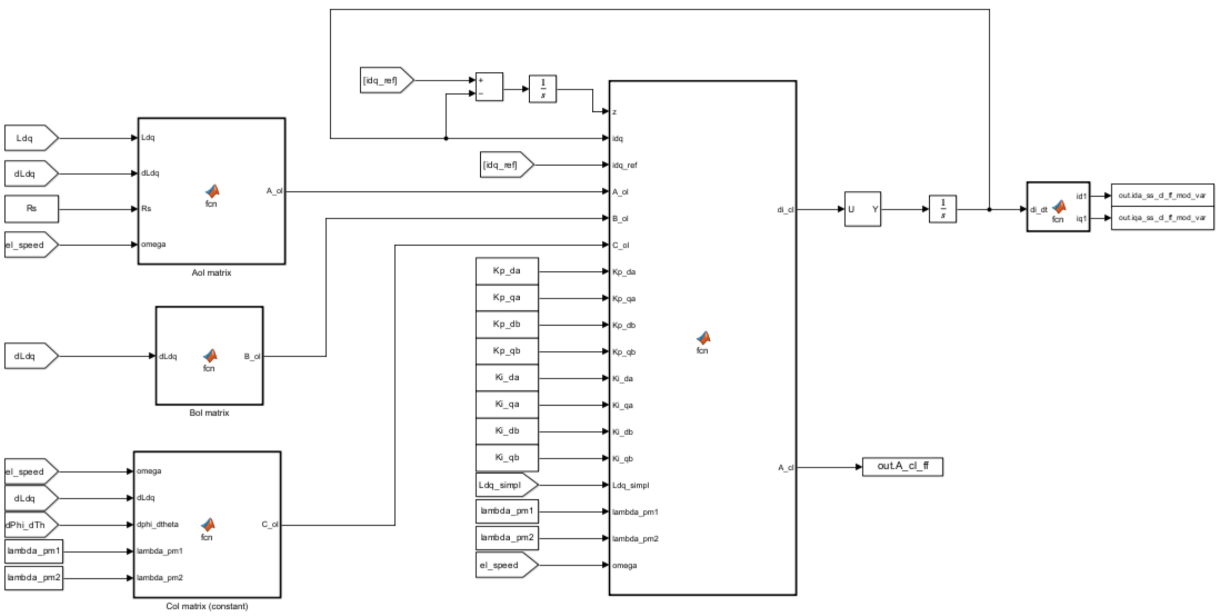

Figure 5.22: State-space closed-loop scheme

5.3 Simulation of IPM motor

The following figure illustrates the incremental inductances as a function of the angular position, obtained directly from the magnetic fluxes. From a control perspective, the oscillations in the inductance values are not taken into account, particularly during the tuning of the PI gains.

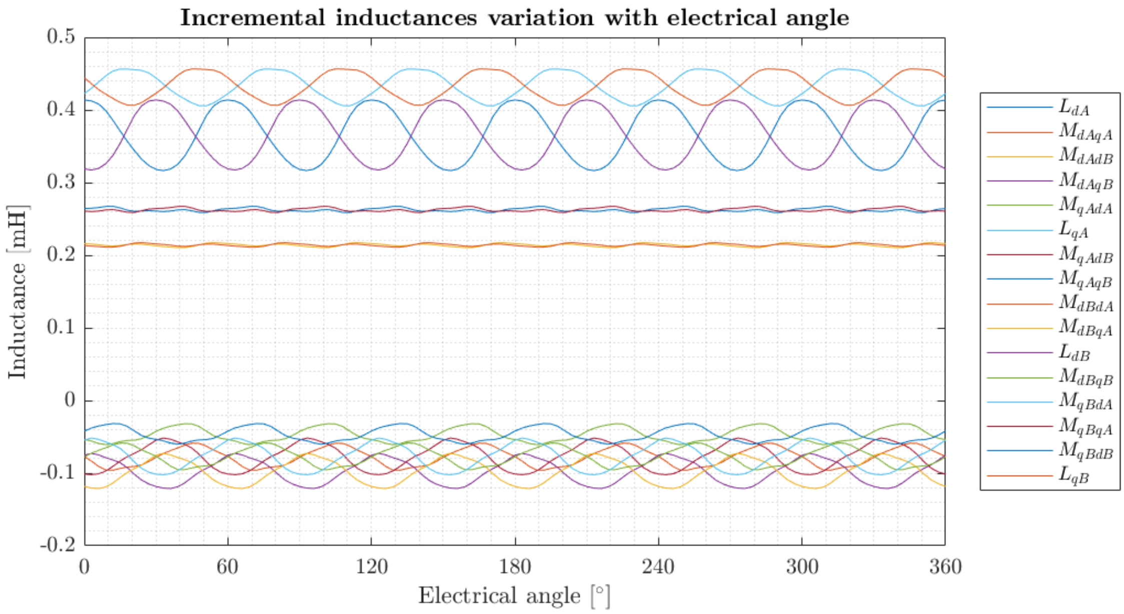

Figure 5.23: IPM - incremental inductance variation with respect to the angle

5.3.1 Comparative analysis

In the following, the torque behavior is evaluated by computing the two methods presented in section 5.1. The test imposes the nominal speed and a load torque of 50 Nm, which is applied at $t = 0.25$ s, once the system reaches steady-state operation at no load.

The results show that the velocity controller, and consequently the inner current control loop, function effectively. The system quickly reaches the reference speed before $t = 0.25$ s, demonstrating fast dynamic response without overshoot. Upon the application of the load, a transient response is observed, and the system settles back to steady-state conditions within approximately 0.20 s.

A comparison of the torque obtained using the LUT and the analytical formula (5.2) shows good agreement with the reference values. The primary difference lies in the oscillatory behavior: when using the analytical formula, the PI controller tends to attenuate the current variation, resulting in reduced oscillations in the torque output.

Torque ripple arises from several factors related to both electromagnetic and mechanical aspects of motor design. One major contributor is cogging torque, which results from the interaction between the permanent magnets on the rotor and the stator slots, causing periodic torque variations even in the absence of current. Additionally, the intrinsic saliency of IPM motors introduces a component of reluctance torque, which varies with rotor position and further contributes to the total torque ripple.

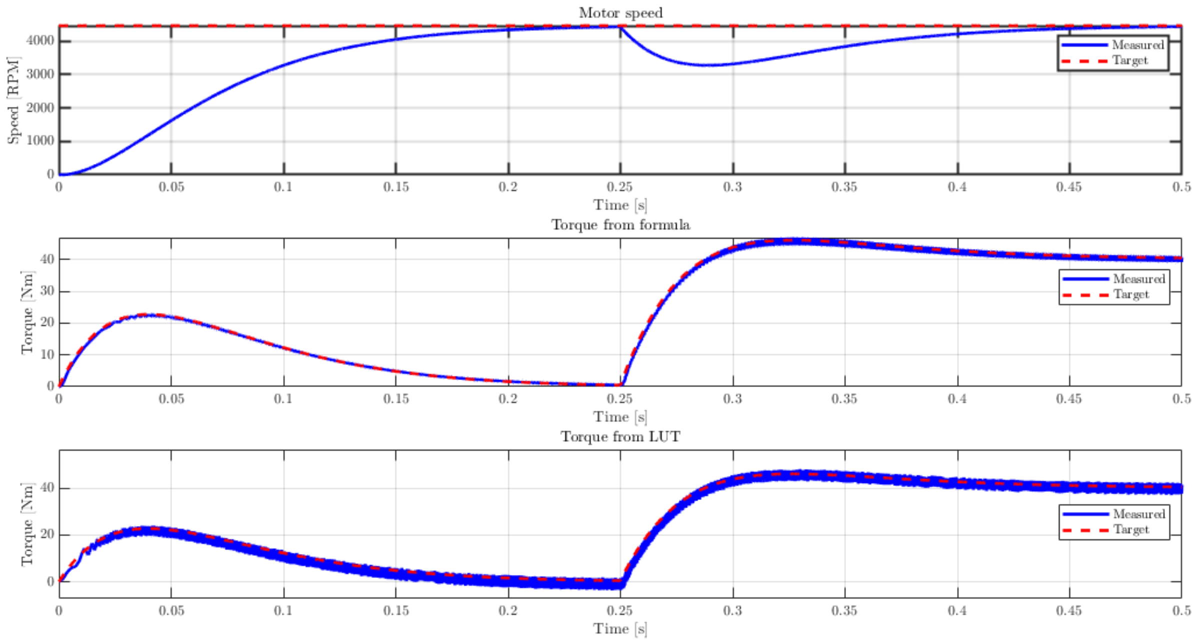

Figure 5.24: IPM - torque comparison at different speeds

PI control

This section presents a comparison between the classic PI controller, a modified PI, and an autotuning PI. The analysis focuses on the transient response observed at system startup for both the d and q axes. For the sake of brevity, only sector a is analyzed, as sector b exhibits similar behavior.

In the following tests, a speed of 100 RPM is used instead of the nominal value, as it provides a clearer response with fewer oscillations. This is justified by the fact that the values of K_p and K_i depend solely on the current and not on the speed, since the inductances are modeled as functions of current. The torque request remains unchanged, while the motor speed is simply reduced.

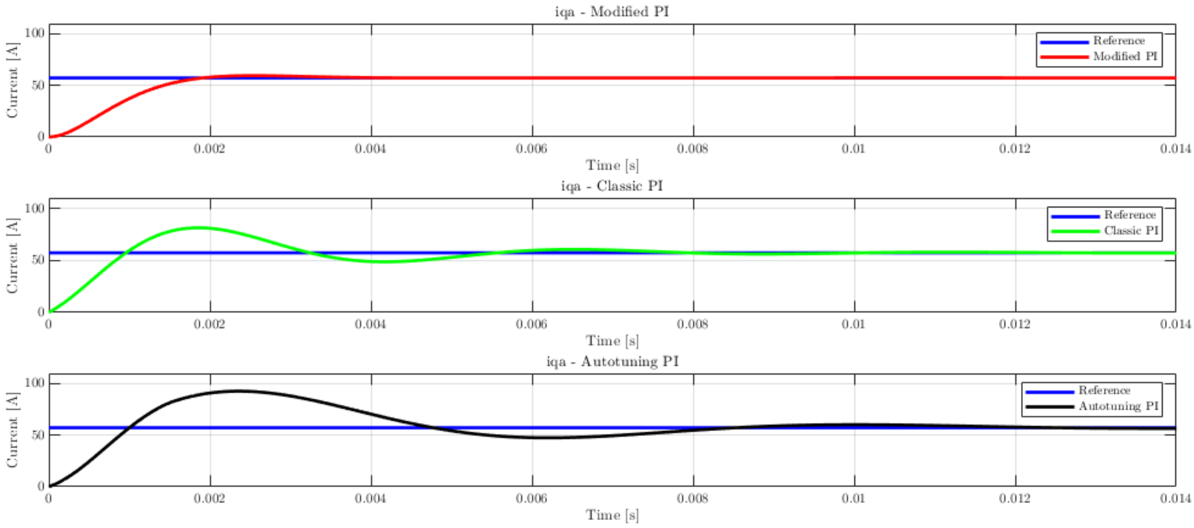

Figure 5.25: IPM - comparison of classic PI, modified PI, and autotuning PI in q axis

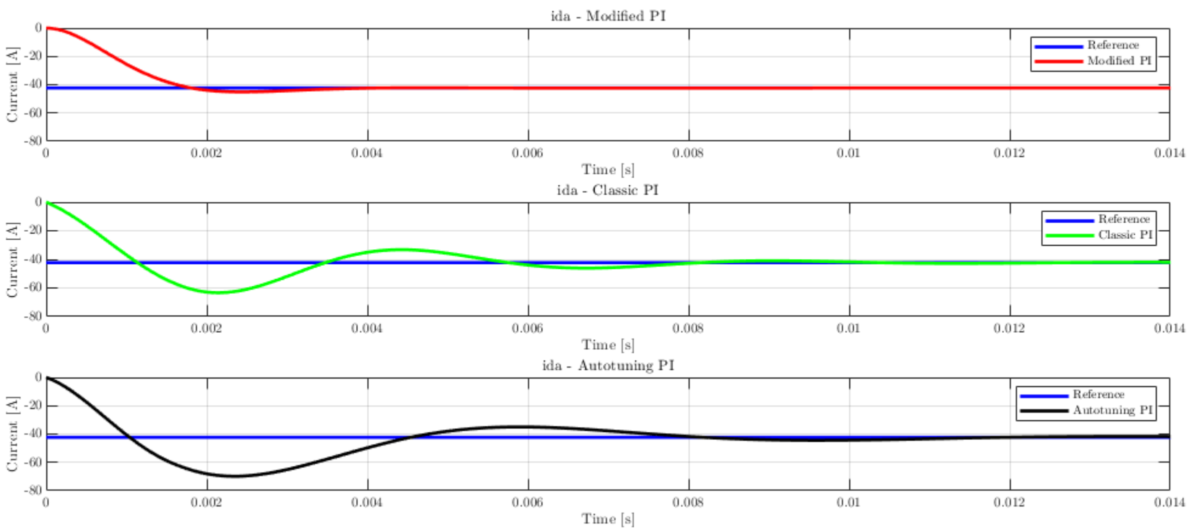

Figure 5.26: IPM - comparison of classic PI, modified PI, and autotuning PI in d axis

The figures show that the modified PI controller performs best, exhibiting minimal oscillation, a short settling time, and a very small overshoot. In contrast, the classic PI controller reaches the desired current with noticeable transient behavior, characterized by a high overshoot and prolonged oscillations. The autotuning PI controller demonstrates an initial response speed similar to the classic PI, but with a significantly higher overshoot and the longest oscillation duration before reaching steady state.

In the following, the current differences between the control based on equation (2.39) and the one presented in equation (2.43) are illustrated:

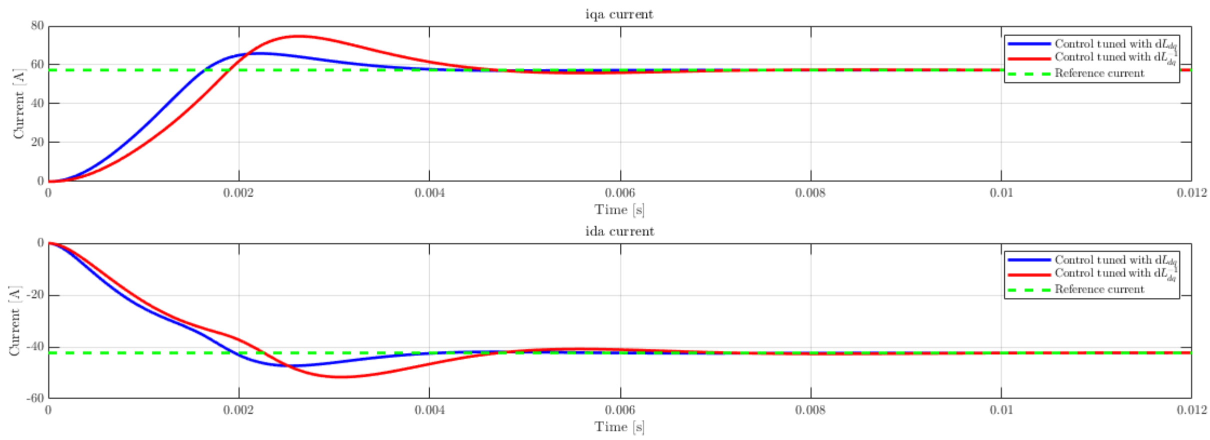

Figure 5.27: IPM - comparison modified PI with different K_p and K_i

As presented in the current response graph, the PI controller gains tuned using the matrix dL_{dq} result in significantly improved dynamic performance compared to those obtained using its inverse, dL_{dq}^{-1}. Specifically, the use of dL_{dq} leads to a faster transient response and a noticeable reduction in overshoot along both the direct and quadrature axes.
For this reason, the next simulation is performed with the first tuning method.

Feedforward compensation

Another important aspect in motor control is feedforward compensation, which plays a significant role primarily during transients, as it helps reduce both delay time and overshoot. In the following analysis, different cases are compared: (i) absence of feedforward compensation, (ii) compensation using fixed self-inductance values calculated at nominal conditions, (iii) compensation with self-inductance varying as a function of current, and (iv) compensation using both self and mutual inductances fixed at nominal conditions.
The analysis is carried out at nominal speed, since feedforward compensation becomes significant only at high speeds.

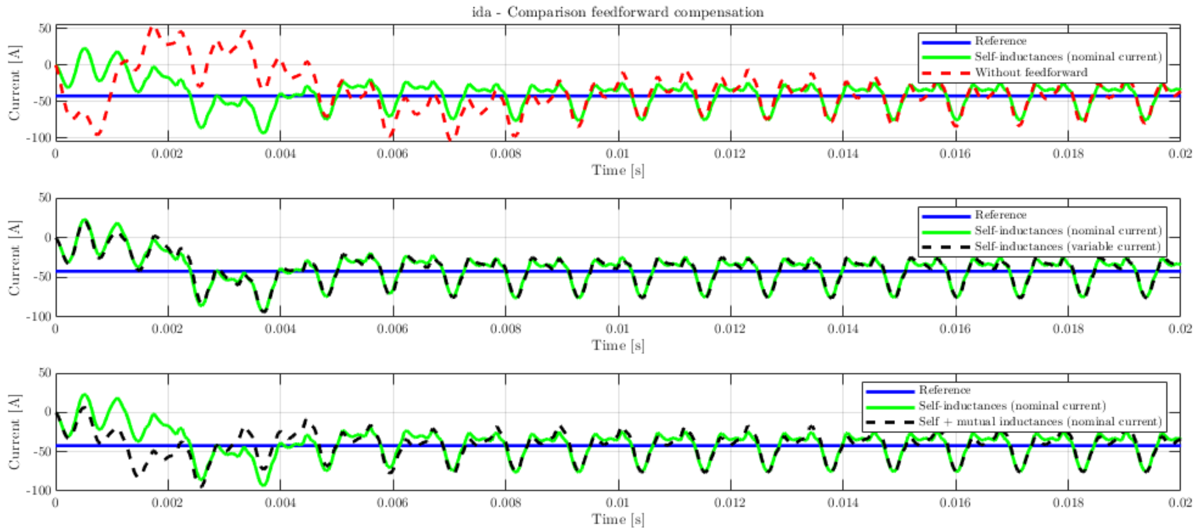

Figure 5.28: IPM - comparison feedforward compensation in d axis

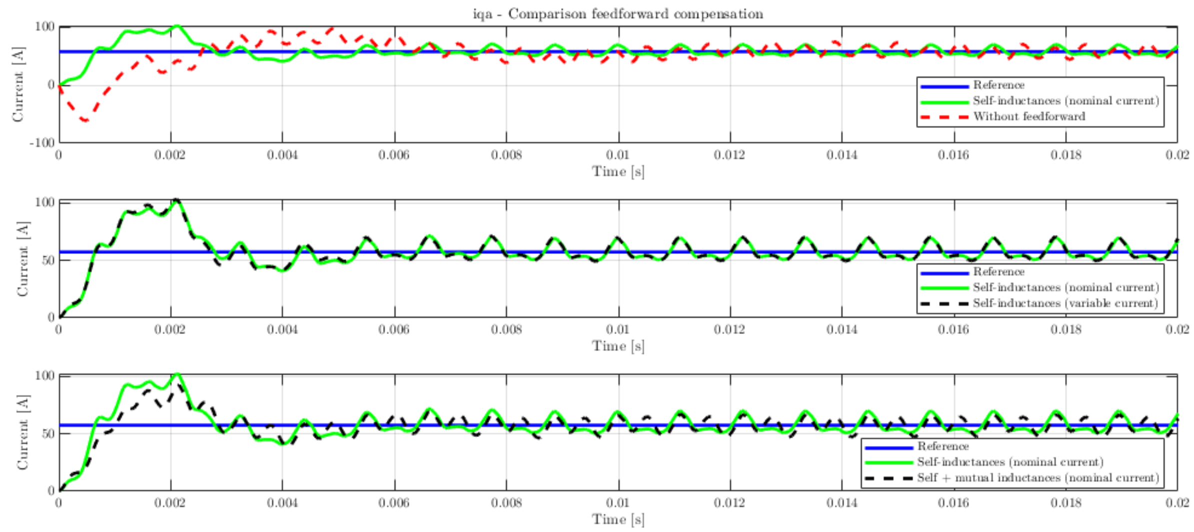

Figure 5.29: IPM - comparison feedforward compensation in q axis

A longer time scale is chosen compared to the previous plots to emphasize that, after a certain period, the self-inductances (at nominal current) in all cases converge and align with the behavior observed in the previously described configuration. This confirms that the feedforward action is effective only during the transient phase; once the transient has passed, the PI controller, acting on the measured error, governs and corrects the behavior.

When no feedforward is applied, or when feedforward uses only the self-inductances evaluated at nominal current, the transient response exhibits a less favorable behavior, in particular, larger deviations appear on both axes during the initial response. By contrast, comparing results obtained with inductances fixed at nominal current versus inductances updated according to the actual current drawn by the machine reveals only minor differences, especially in the initial phase; this is expected since the system is being tested under nominal operating conditions. Finally, considering both self-inductances and mutual inductances fixed at the nominal current yields results very similar to the fixed current case with only self-inductances. However, the first configuration has the advantage of a simpler implementation.

In chapter 4, it is noted that it may be advantageous to include only the self-inductances together with the dominant mutual terms. No further tests are conducted for this configuration, as the difference between using all inductances and using only the self-inductances with the largest mutual couplings is negligible, making additional validation unnecessary.

Machine equation and state space with modular approach

For the comparative analysis, three modeling approaches are considered:

1. Machine equations developed in Simulink as presented in figure 5.6;
2. Separate open-loop state-space representations are used to analyze the motor model and the controller;
3. A closed-loop state-space formulation that integrates the controller into the system dynamics as presented in figure 5.22.

In all cases, a modified PI controller without feedforward compensation is employed, and the inductance values vary as functions of the phase current. It is possible to notice that all three methods used are equivalent.

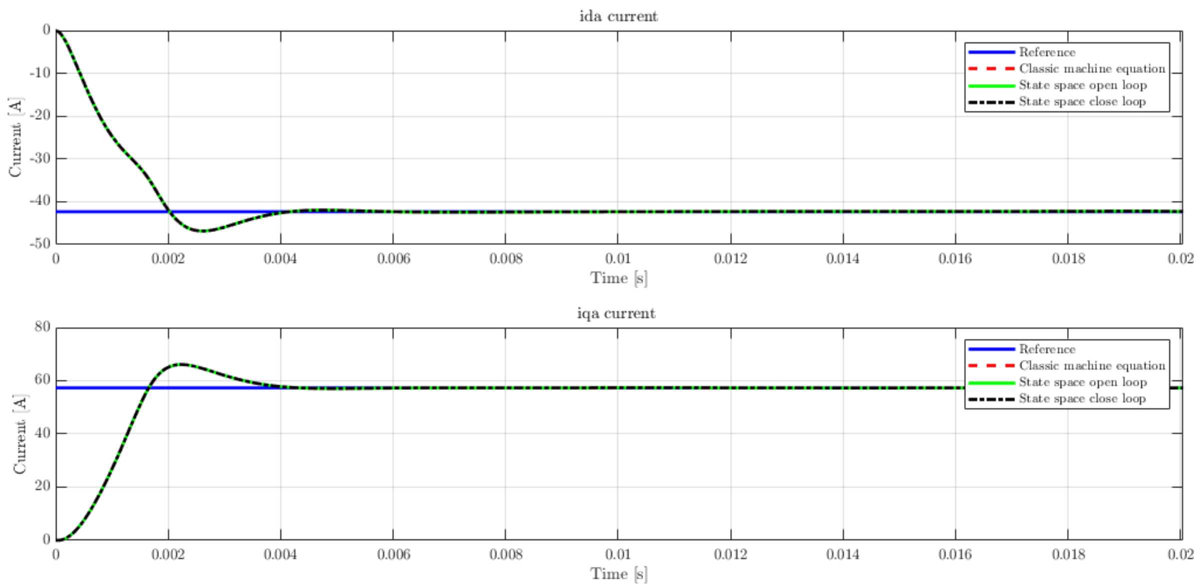

Figure 5.30: IPM - current comparison between machine equation and state space

SISO and MIMO

Starting from the simplified equations in (2.39) and (2.43), both can be reformulated in the form of the three-phase motor equations as shown in (1.41). For a dual three-phase motor, the equations must be rewritten by doubling the number of transfer functions to account for the additional phases.

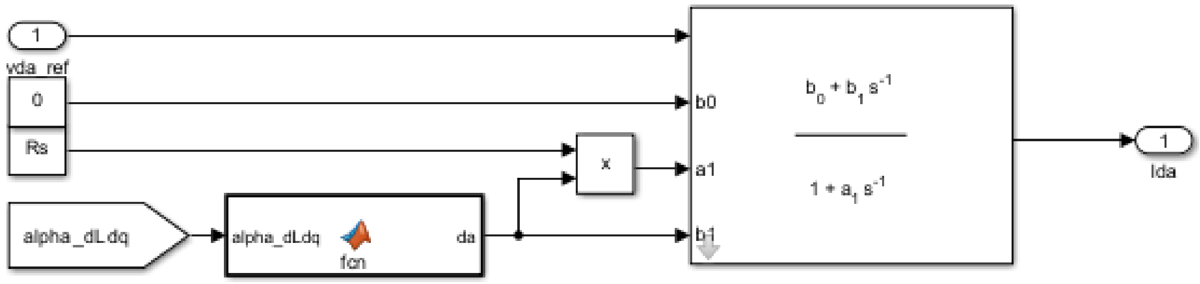

Figure 5.31: Transfer function scheme for d_a axis

This test aims to evaluate the impact of using a MIMO system, which accounts for mutual interactions between different axes, compared to a SISO approach that models each axis with an independent transfer function. All tests are conducted using a modified PI controller with feedforward compensation based on self-inductances at nominal current.

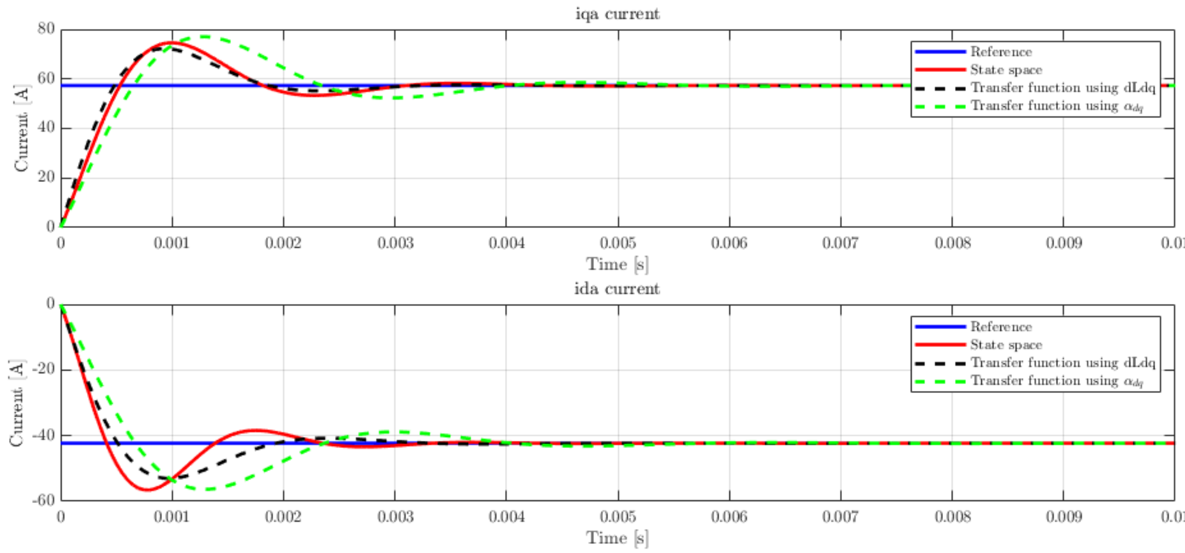

Figure 5.32: IPM - current comparison between SISO and MIMO

As anticipated in the theoretical analysis, the speed control system of a dual-three-phase machine can be modeled as a SISO system. In contrast, the current control requires a MIMO approach to accurately capture the system dynamics. As shown in the two figures, the characteristics resulting from the SISO and MIMO models differ significantly.

Machine equation and state space with VSD

The same test described in the subsection "Machine equation and state space with modular approach" is performed here using the VSD method, instead of the modular approach.

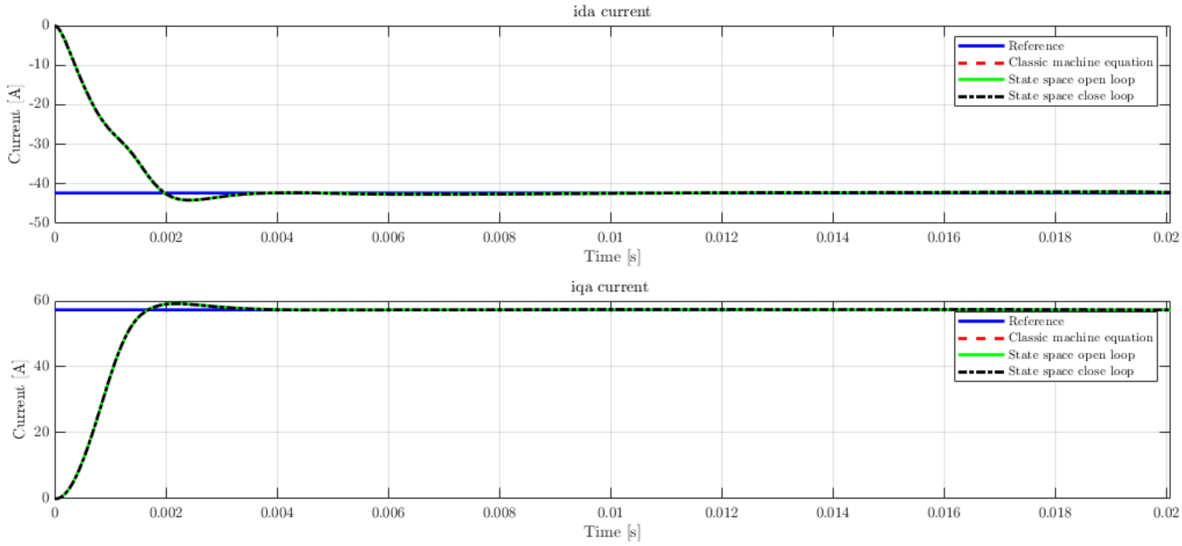

Figure 5.33: IPM - current comparison between machine model and state space

In this case as well, all three methods analyzed showed perfect agreement, as expected.

Current response with modular approach and VSD

After analyzing the modular approach and the VSD and performing various system comparisons to verify the correctness of the model, the differences between the two control strategies are presented below:

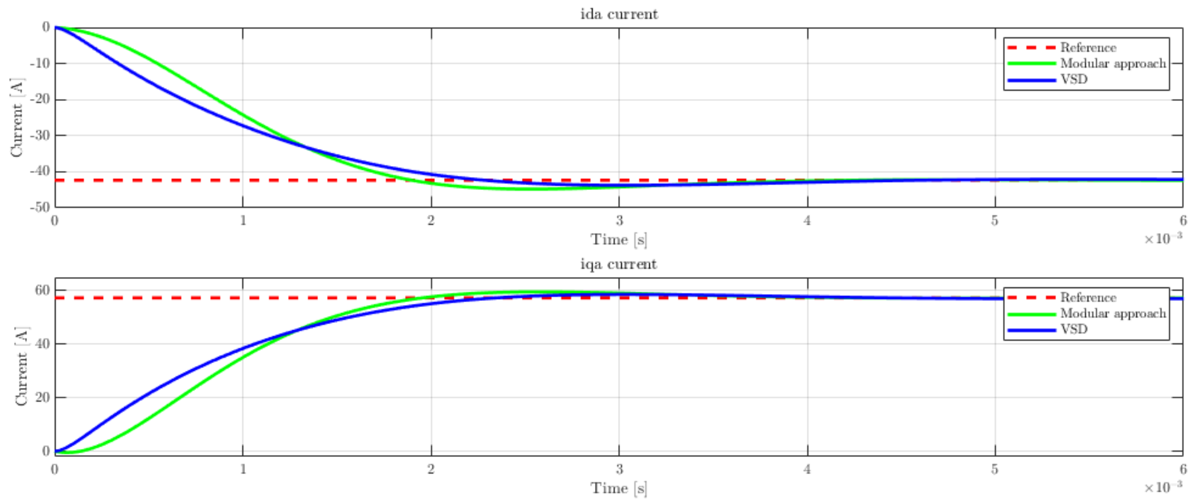

Figure 5.34: IPM - current comparison between modular approach and VSD

Both controls reach steady state in approximately the same amount of time. The main differences lie in the rise time, which is shorter for the modular approach, and the overshoot, which is lower for the VSD. Therefore, each control strategy exhibits different performance characteristics, and the choice between them should be based on the specific requirements of the application.

Continuous and discrete PI

Up to this point, a continuous PI controller has been considered, representing a theoretical approach. In this simulation, the focus is on how the motor current and torque are affected when passing from a continuous to a discrete PI controller. The test is carried out at nominal speed, where the differences between the two methods are most pronounced.

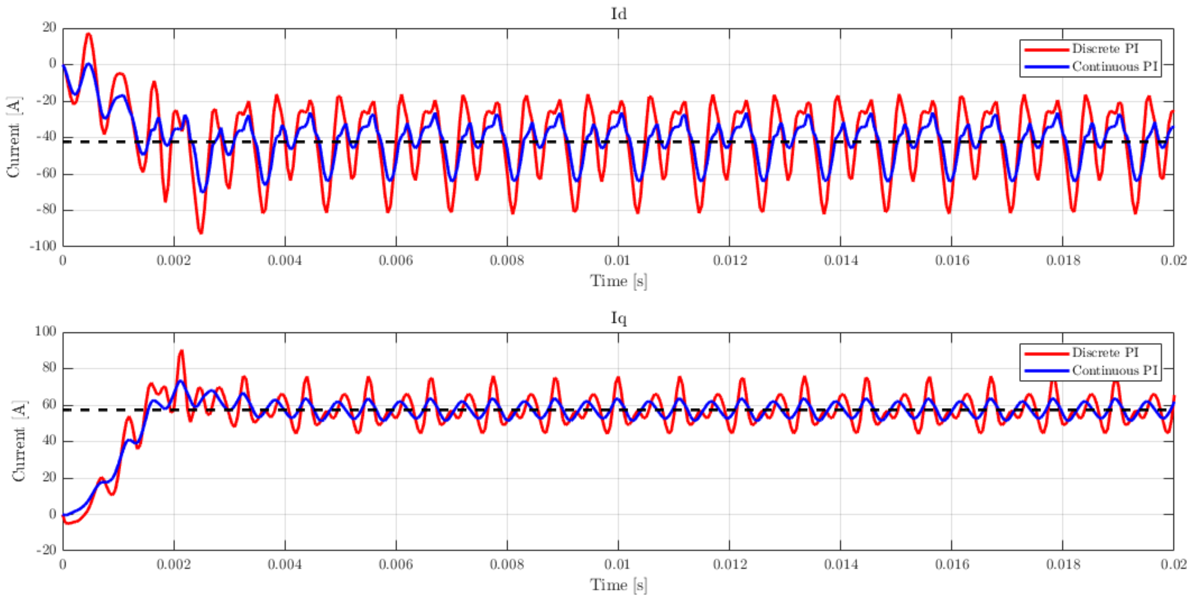

Figure 5.35: IPM - current comparison between continuous and discrete PI

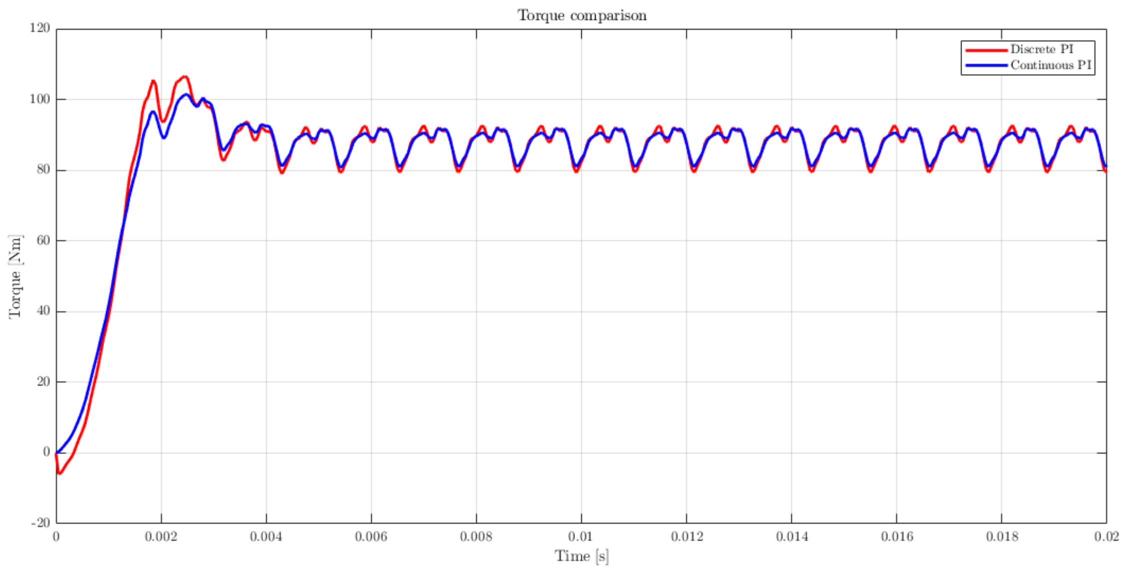

Figure 5.36: IPM - torque comparison between continuous and discrete PI

Significant differences are observed in both axes, with more pronounced discrepancies in the d-axis. The torque contribution varies notably during transients, while steady-state discrepancies occur only during rapid changes.

5.3.2 System response to current variation

To evaluate the system's robustness to electrical disturbances, particularly relevant in automotive and aerospace applications, an oscillatory noise is injected into the i_d current reference in Simulink. This choice allows testing the system's behavior under flux-related disturbances without affecting the torque generation too much, which is primarily controlled by the i_q component. The test is conducted at nominal speed to simulate standard operating conditions of the motor.

As a first step, the noise is injected only into the current component i_{da}:

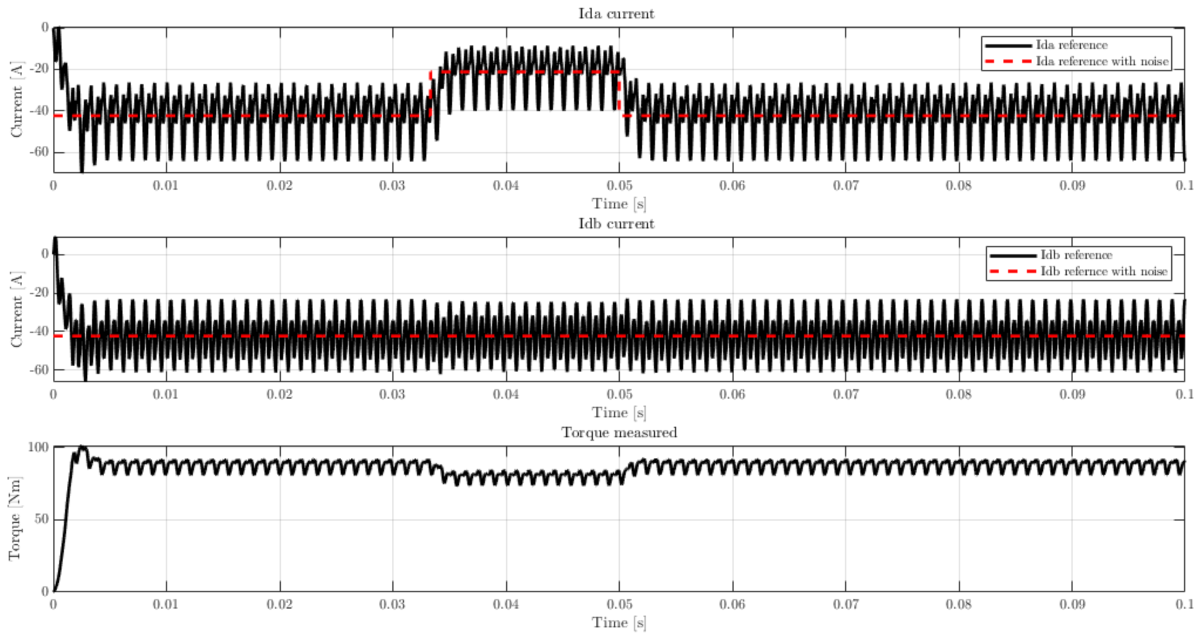

Figure 5.37: IPM - noise injection in i_{da}

The torque variation is negligible, even when the current request is reduced to half of its nominal value along the i_{da} axis. Additionally, the transient response during current noise injection, both in current and torque, is rapid.

As a second step, the noise is injected into both the current component i_{da} and i_{db}:

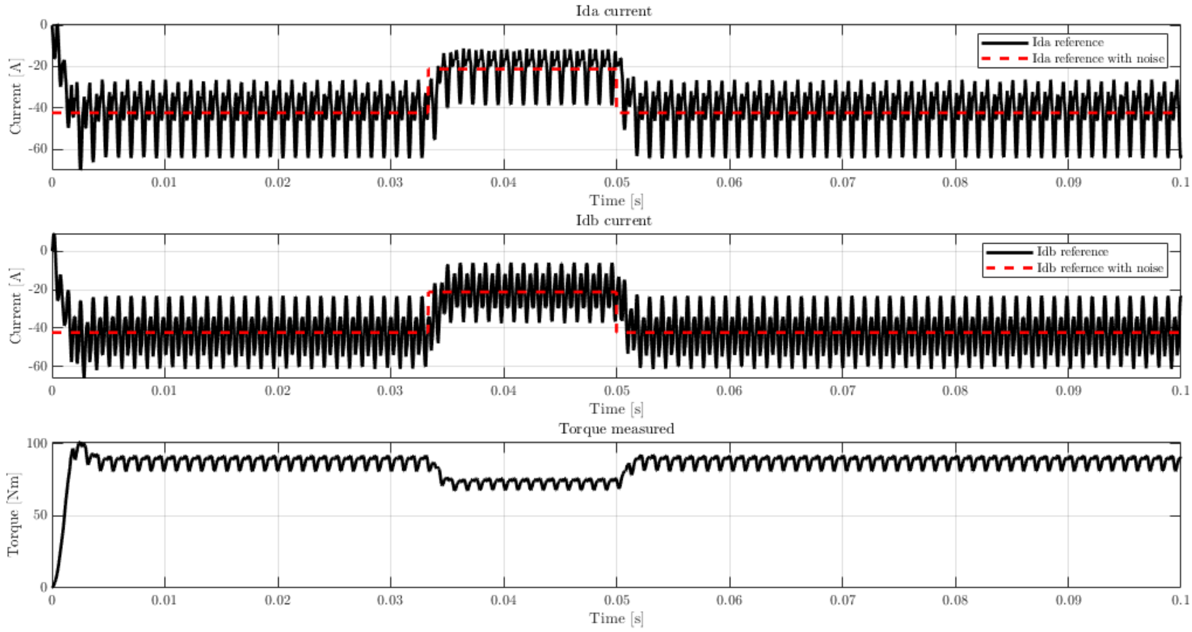

Figure 5.38: IPM - noise injection in i_{da} and i_{db}

Despite requiring only half the current in both the d-axis components, the torque maintains a reasonable level of production.

5.3.3 Proportional and integral gains as functions of the current

Modular approach

The following test is conducted by applying twice the nominal torque, using step increments of 5 Nm up to 100 Nm, and then 10 Nm increments thereafter. Doubling the nominal torque allows for a more extended and detailed graph of the system response.

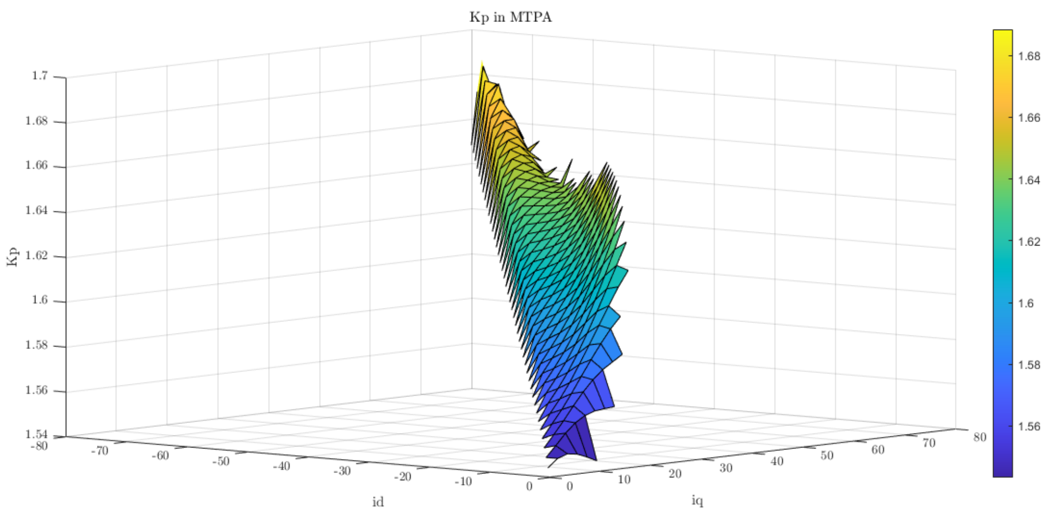

Figure 5.39: IPM - proportional gain

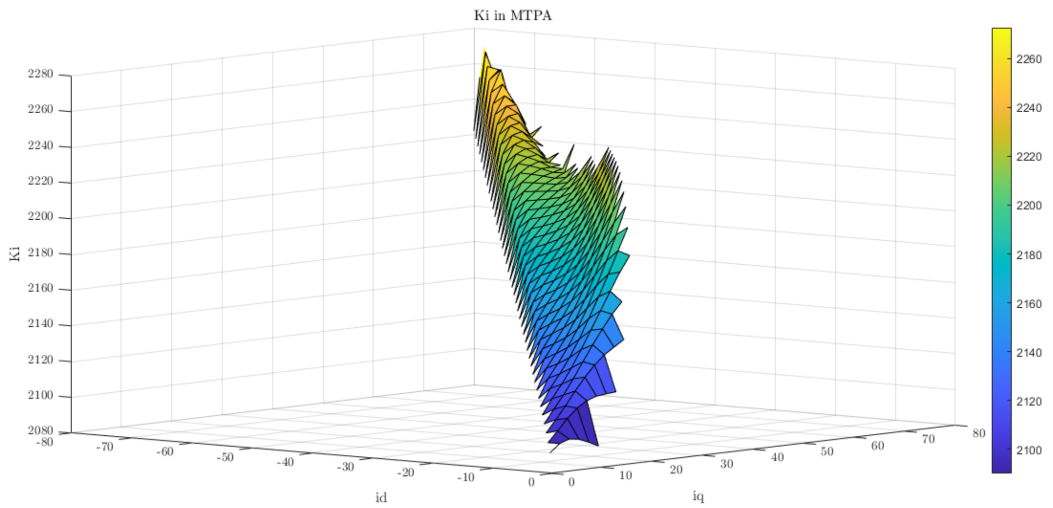

Figure 5.40: IPM - integral gain

Referring to equations (2.44) and (2.45), as well as their counterparts in the other sector, the proportional and integral gains vary as a function of the differential inductances, which in turn depend on the current.

VSD

To understand the differences between the two control strategies, it is also important to visualize also in this case the variation of the K_p and K_i parameters as functions of the current. For a valid comparison, the same torque demand and identical test conditions are used, with only the current control strategy being varied.

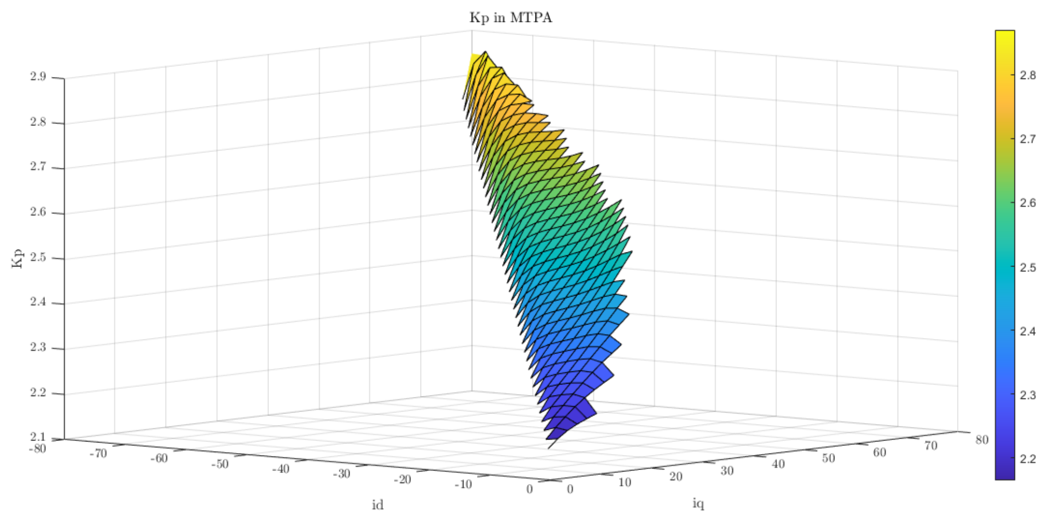

Figure 5.41: IPM - proportional gain VSD

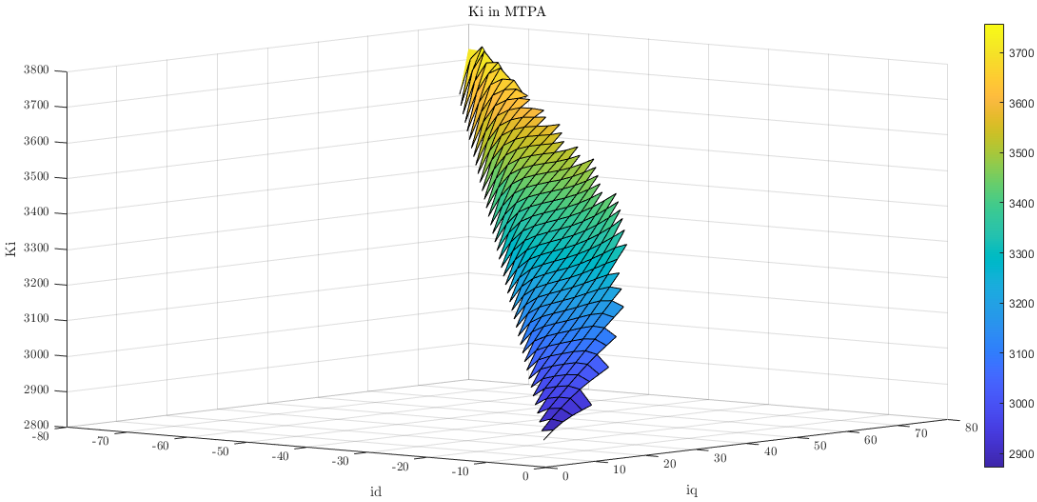

Figure 5.42: IPM - integral gain VSD

The control gains obtained using the VSD approach are smoother compared to those from the modular method. In particular, spikes that appear in the modular approach are absent with VSD, for both K_p and K_i. This behavior is also reflected in the eigenvalue analysis discussed in chapter 5.

5.3.4 Efficiency map

The following efficiency map is obtained using formulas that estimate Joule, iron, and mechanical losses, considering all operating conditions below the nominal values for both torque and speed. As shown, efficiency is lower at low speeds or low torques due to losses being significant relative to the generated power.

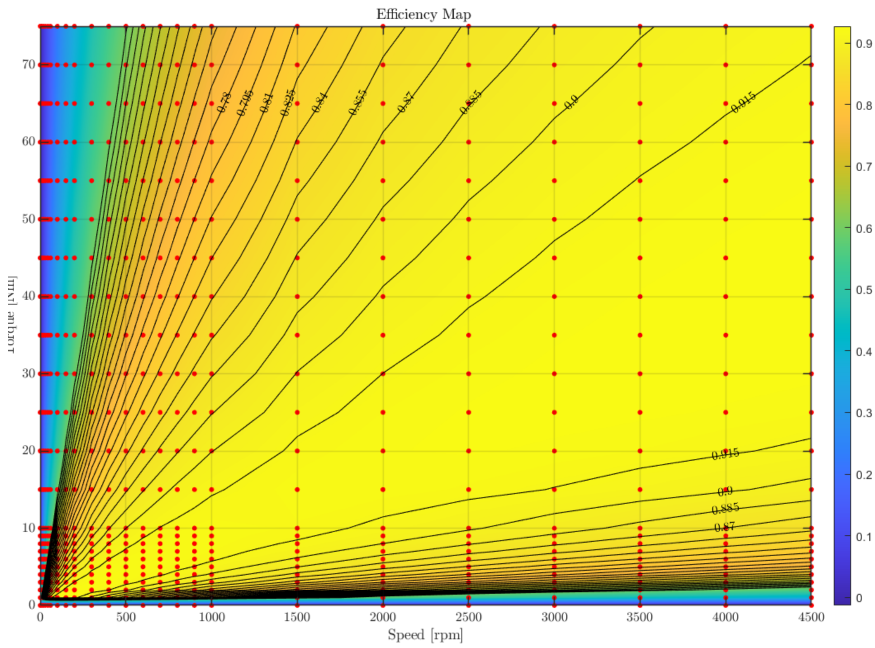

Figure 5.43: IPM - efficiency map

5.3.5 Bode diagram

In accordance with the open-loop transfer function derived in equation 3.5, figure 5.44 presents the Bode magnitude and phase plots of the speed control and the mechanical plant.

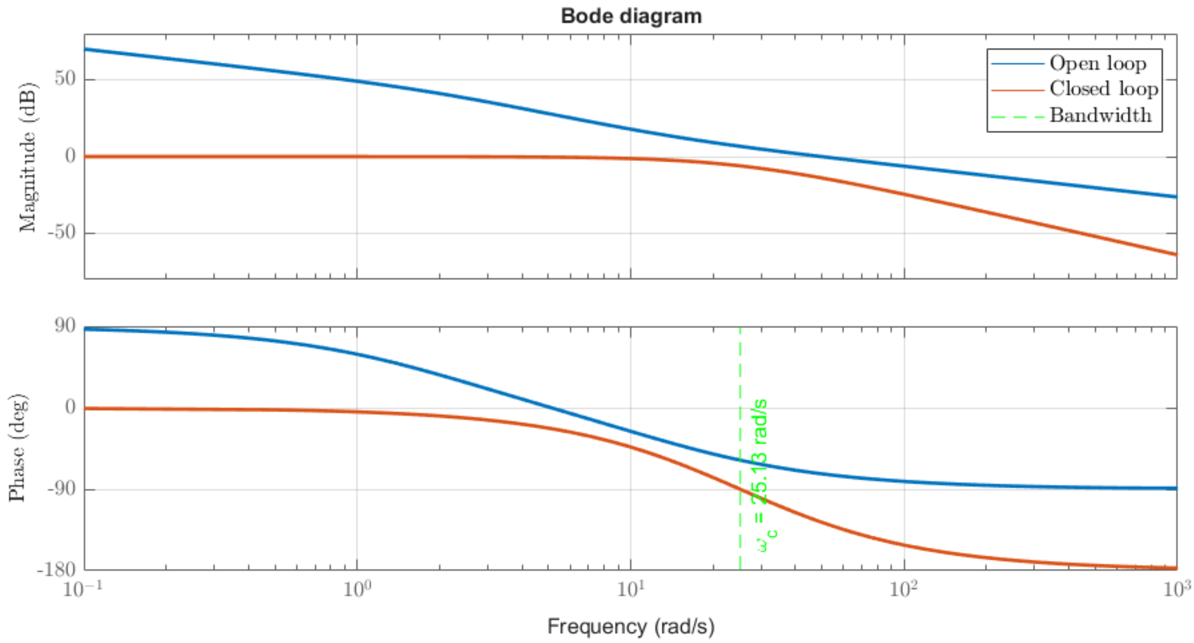

Figure 5.44: IPM - Bode diagram

The figure presents two transfer functions: the open-loop transfer function (blue curve) and the closed-loop transfer function (red curve). These are compared against the reference values introduced in the theoretical framework to evaluate the stability of the system.

From the analysis of the open-loop transfer function, a phase margin of approximately 107° is observed. This exceeds the commonly recommended threshold of 75°, indicating that the system is stable with a considerable safety margin. Additionally, the magnitude margin satisfies the recommended criterion of exceeding 3 dB, further confirming system stability.

A vertical green dashed line is drawn at approximately ω_b = 25.13 rad/s, denoting the closed-loop bandwidth. This corresponds to the frequency at which the magnitude of the closed-loop response falls by 3 dB.

5.3.6 Nyquist plot

Another approach to assess the system's stability is presented here, based on the **Nyquist stability criterion** introduced in section 3.2.

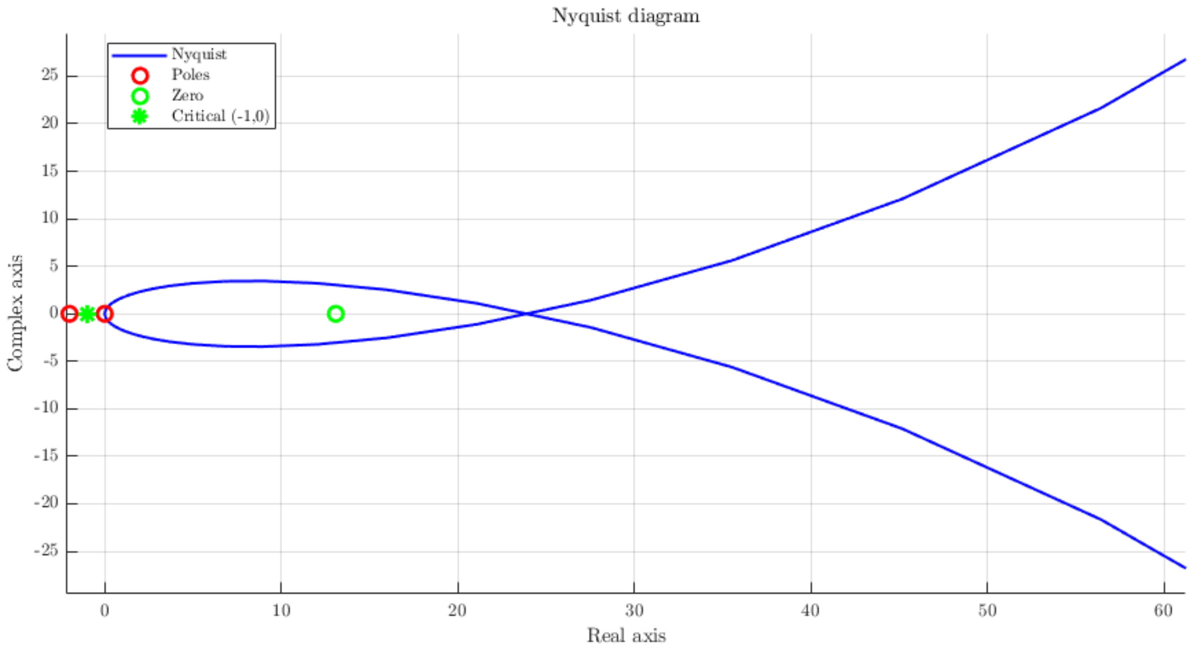

Figure 5.45: IPM - Nyquist diagram

The Nyquist diagram shown allows for a detailed analysis of the closed-loop stability of the system by applying the Nyquist stability criterion. Below are the key observations:

- **Shape of the Nyquist curve (blue line):** the Nyquist plot of the open-loop transfer function does not encircle the critical point $-1 + j0$. In fact, the entire plot lies to the right of this point and does not intersect it. Since the critical point is not encircled by the Nyquist plot, it follows that:

$$N = 0.$$

- **Open-loop poles (red markers):** all poles of the open-loop transfer function are located in the left half of the complex plane (i.e., they have negative real parts), so:

$$P = 0$$

- **Conclusion Nyquist criterion:** by applying the following equation, where Z represents the number of unstable closed-loop poles, is obtained:

$$Z = N + P = 0 + 0 = 0$$

Therefore, the closed-loop system is also stable according to this method.

5.3.7 Pole position

The eigenvalues of the matrix A_{cl}, introduced in chapter 3.3.3, are analyzed in this section considering nominal working conditions. Since A_{cl} is an 8×8 matrix, the system has eight poles. The eigenvalues are arranged in symmetric pairs with respect to the real axis, resulting in four poles with positive imaginary parts and four with negative imaginary parts.

Fix K_p and K_i

Control systems are typically implemented using fixed values of K_p and K_i, which remain constant across all operating conditions. In this first part of the eigenvalues analysis, this conventional approach is analyzed.

Modular approach

As a first step, the variation of the pole positions with respect to speed is analyzed, keeping both the motor model and the controller parameters unchanged.

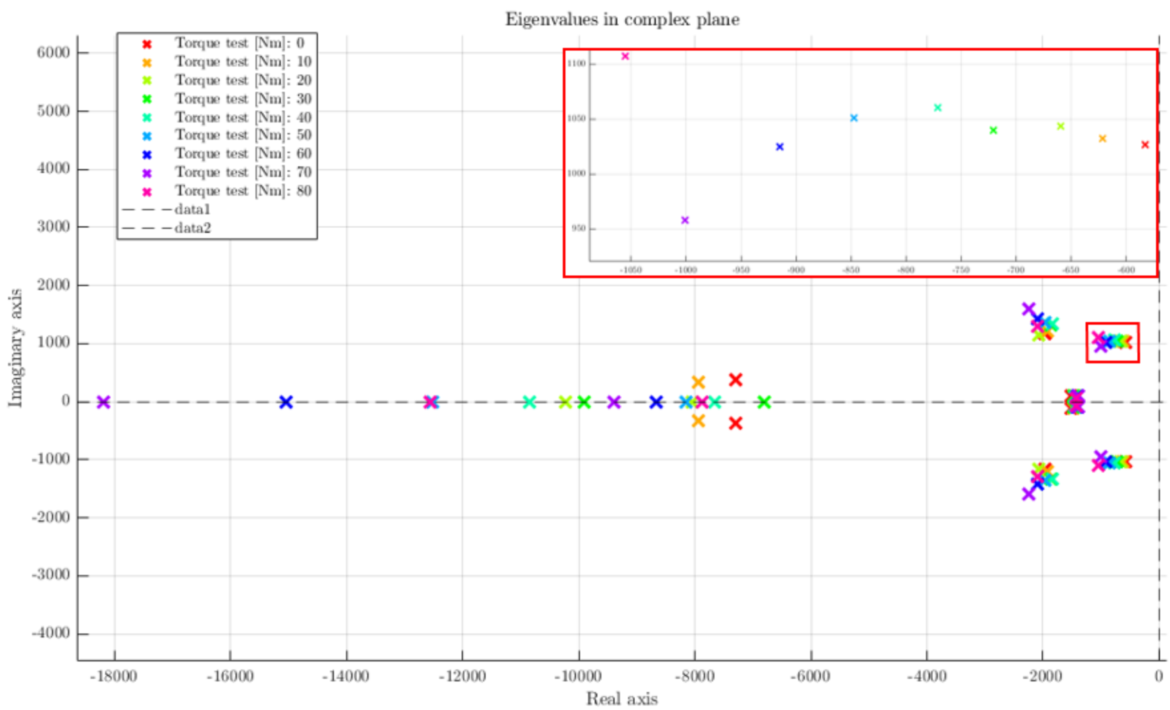

Figure 5.46: IPM - eigenvalues at 1000 rpm with fixed K_p and K_i

In this first graph, the torque test is performed at intervals of 10 Nm up to the nominal torque, in order to highlight the symmetry of the eigenvalues and confirm that the system has eight poles. In the following analysis, the test is extended to include overload conditions, reaching up to twice the nominal torque. The most critical area is highlighted with a red box, and a zoomed-in view of this region is shown near the image.

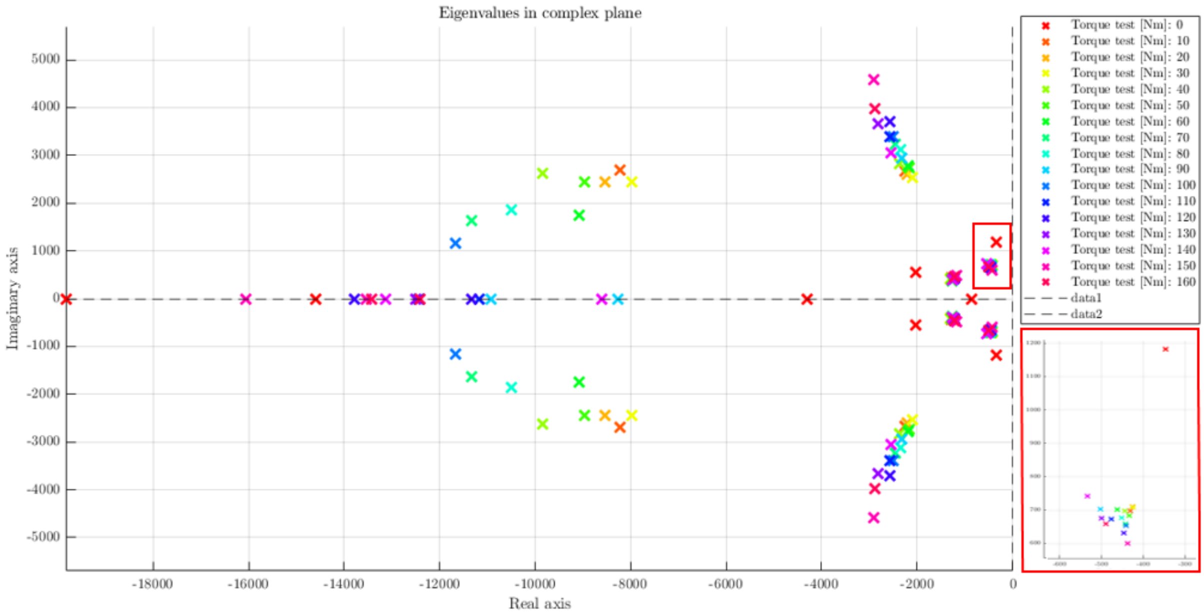

Figure 5.47: IPM - eigenvalues at nominal speed with fixed K_p and K_i

Compared to the case tested at 1000 rpm, the eigenvalues in this scenario exhibit a generally higher imaginary range and are less clustered. Nevertheless, in both cases, all eigenvalues lie in the left half of the complex plane, confirming that the system remains stable under all tested conditions.

Additionally, the eigenvalues are symmetrically distributed with respect to the real axis, which is characteristic of an underdamped system. This behavior is consistent with typical three-phase motor dynamics and is particularly evident in figure 1.5.

The zoomed view at nominal speed reveals that the eigenvalues at zero torque present the lower damping compared to other operating conditions. Consequently, the start-up phase represents the worst-case scenario, even more critical than when the system operates at twice the nominal torque.

VSD

Now let's analyze the second control strategy developed, performing the same test used for the modular approach, to determine the characteristics of this system:

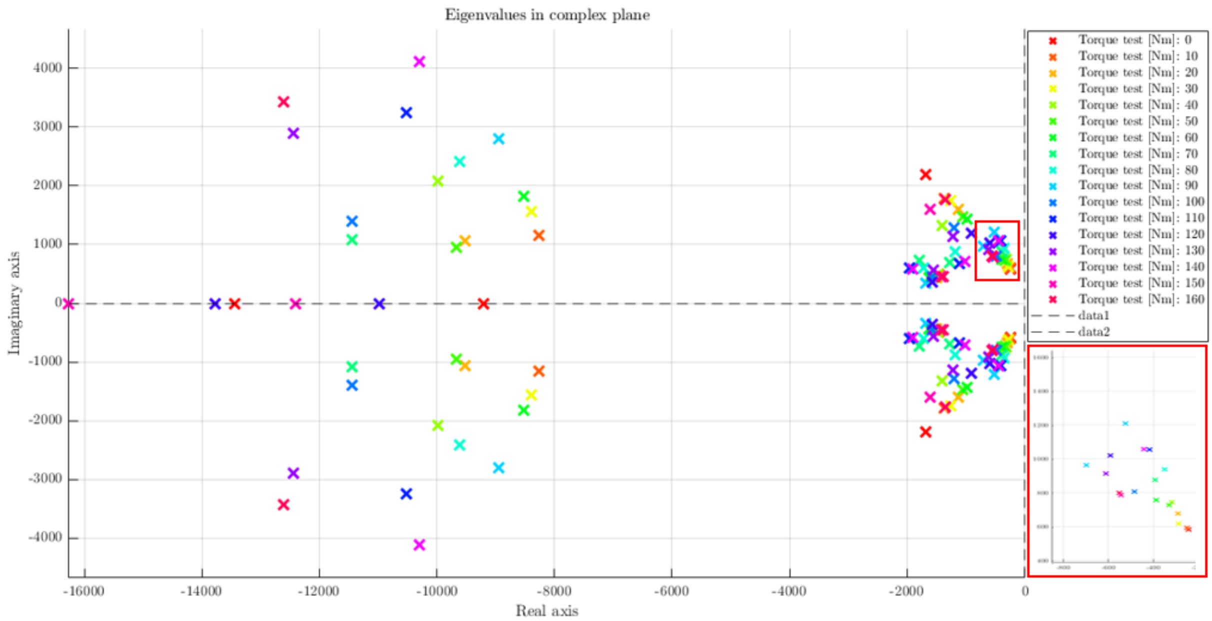

Figure 5.48: IPM - eigenvalues at nominal speed with fixed K_p and K_i VSD

In this case as well, all eigenvalues lie in the left half of the complex plane, confirming that the system remains stable under all tested conditions. Compared to the modular approach shown in figure 5.47, the poles near the imaginary axis are more tightly clustered and exhibit lower and more consistent natural frequencies across all torque levels.
Another notable difference is that, whereas the modular approach revealed a distinct pole at zero torque with unique damping and frequency characteristics, the eigenvalues in this case are more uniformly distributed. At low torque demand, the system operates at lower frequencies; however, as the torque increases, both the frequency and the damping of the system response increase accordingly.

Variable K_p and K_i in function of the reference torque

Since the K_p and K_i gains are typically tuned and fixed based on nominal operating conditions, this section highlights the impact of using different gain values that are specifically calculated for each torque demand. This comparison illustrates how autotuning tuning can influence system performance under varying load conditions.
The tests presented in this subsection are identical to those performed in the previous one, using the same operating conditions and torque references. This consistency ensures a fair and meaningful comparison between the different control strategies.

Modular approach

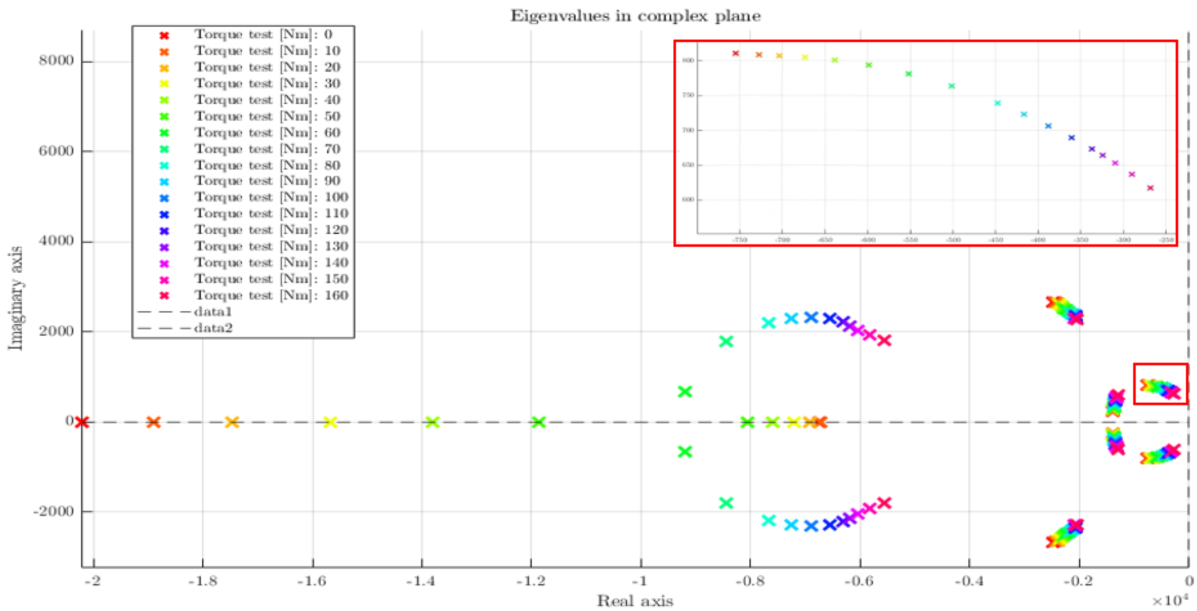

Figure 5.49: IPM - eigenvalues at nominal speed with variable K_p and K_i

In this analysis, the eigenvalues exhibit a more structured distribution, forming a curve along which each pole, corresponding to a specific torque level, appears sequentially. This behavior contrasts with the case of fixed K_p and K_i, shown in figure 5.47, where the zero-torque condition produced a distinct pole isolated from the others. In the current case, that same condition results in a pole that is closely grouped with the others and represents the most favorable configuration, characterized by high pulsation and strong damping. Conversely, the least favorable condition corresponds to the highest torque level, where the system exhibits reduced damping and lower natural frequencies.

VSD

In the following analysis, the theoretical best-case scenario is presented. This scenario combines the advantages of implementing variable proportional and integral gains with the VSD method. By allowing the controller gains to adapt dynamically based on operating conditions, the system can achieve improved performance in terms of stability, responsiveness, and robustness. The integration of gain variability with the VSD approach is expected to exploit the full potential of both techniques.

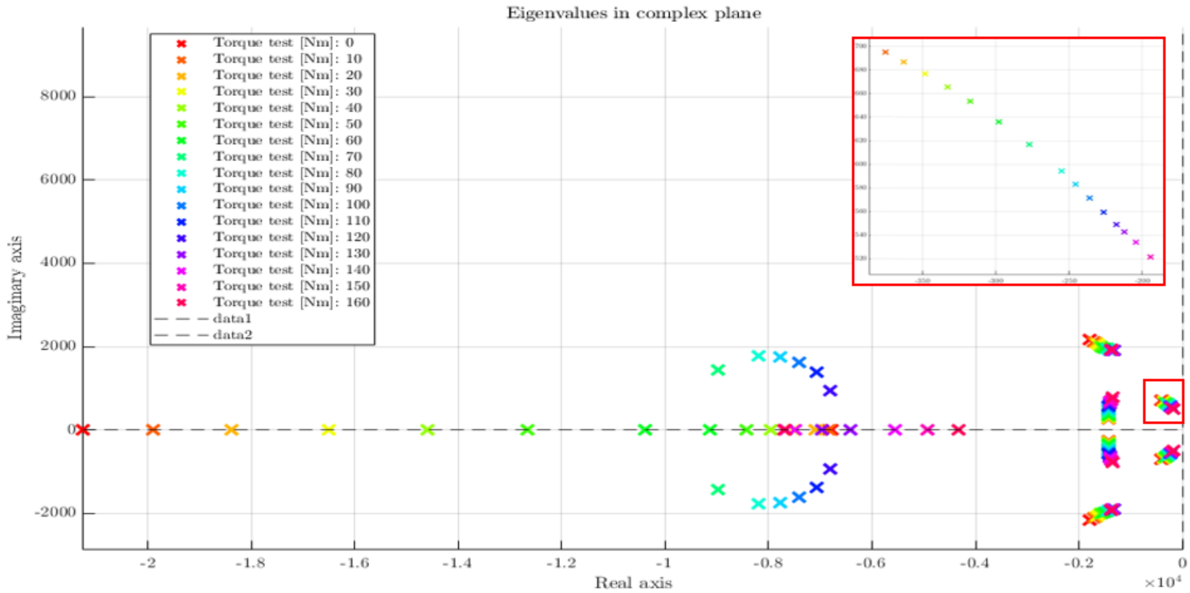

Figure 5.50: IPM - eigenvalues at nominal speed with variable K_p and K_i VSD

Similarly to the modular approach, the pole positions are well-ordered; however, in this case, the poles are more closely clustered for the same torque requests, both in terms of oscillation frequency and damping. This indicates that the system exhibits more consistent behavior even when the torque demand varies.
As expected, this configuration demonstrates the best overall performance compared to all the previously analyzed cases.

5.4 Simulation of SPM motor with non-linear BH curve

An IPM motor typically exhibits greater torque ripple compared to SPM motor. According to the torque equation (2.33), the torque is a function of the flux linkages, which depend on the rotor position. In an SPM motor, the magnetic flux produced by the permanent magnets is relatively constant and aligned with the d-axis of the rotating reference frame. As a result, the q-axis flux component is ideally zero. This flux distribution remains nearly constant with respect to the rotor position in the dq reference frame.

In contrast, an IPM motor exhibits magnetic saliency due to its embedded magnet structure. The rotor geometry introduces a variation in magnetic reluctance along the d- and q-axes, which leads to a flux linkage that varies with the rotor position.

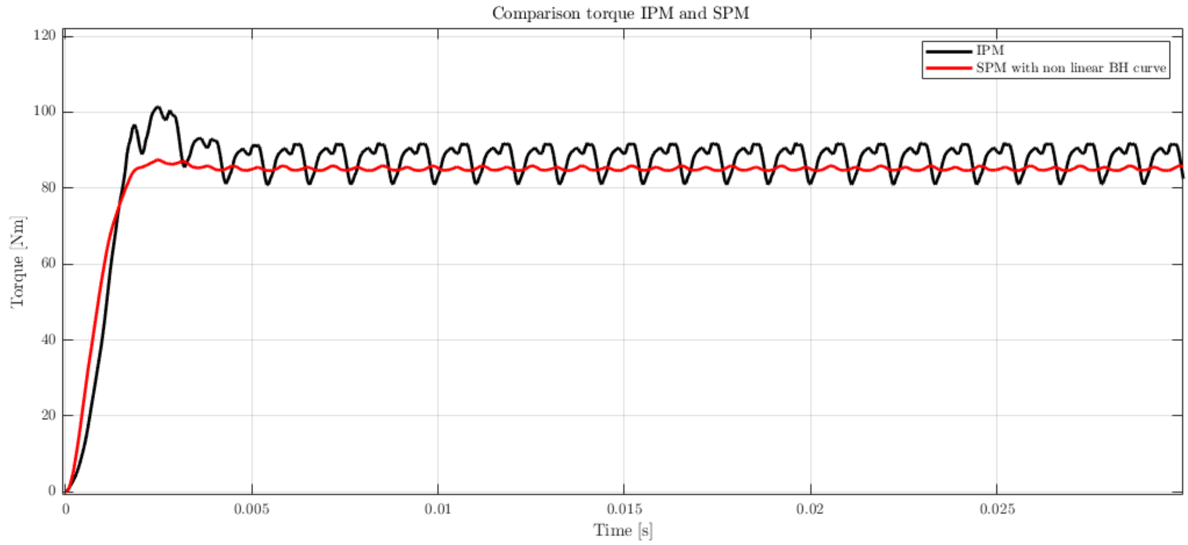

Figure 5.51: Comparison torque produced by IPM and SPM (non-linear BH curve)

The IPM motor was analyzed in greater detail to highlight its specific characteristics. Since the SPM motor shares several similarities with the IPM motor, many features remain comparable. Therefore, only the most significant studies are presented and discussed in the following.

5.4.1 Comparative analysis

PI control

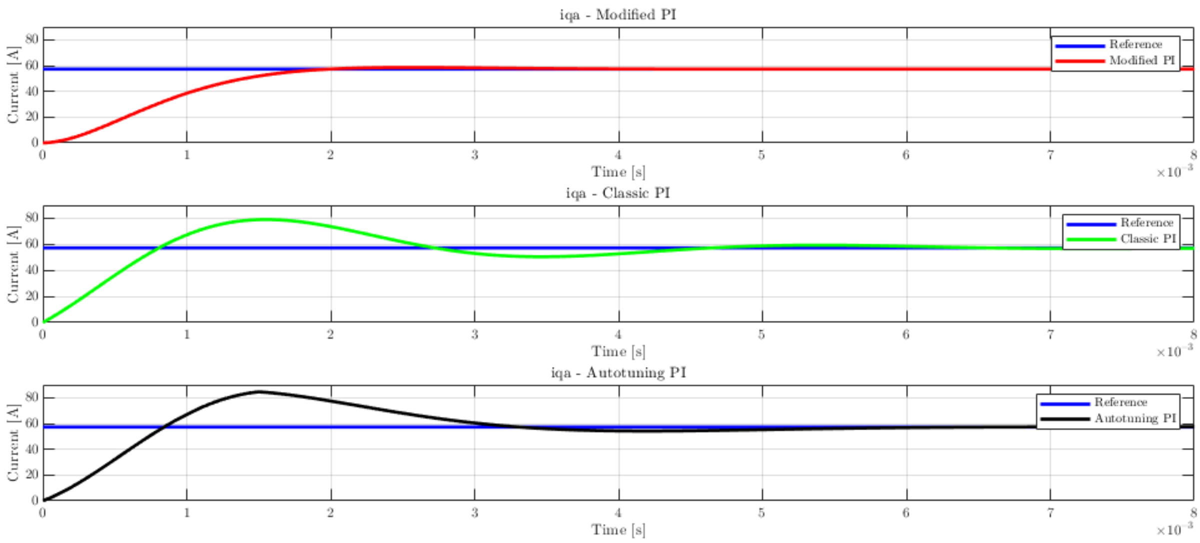

Figure 5.52: SPM - comparison of classic PI, modify PI, and autotuning PI in q axis

For the SPM motor as well, the best performing controller is the modified PI, followed by the classic PI, with the autotuning PI yielding the least favorable results. This ranking holds true for both the time required to reach steady state and the overshoot.

Current response with modular approach and VSD

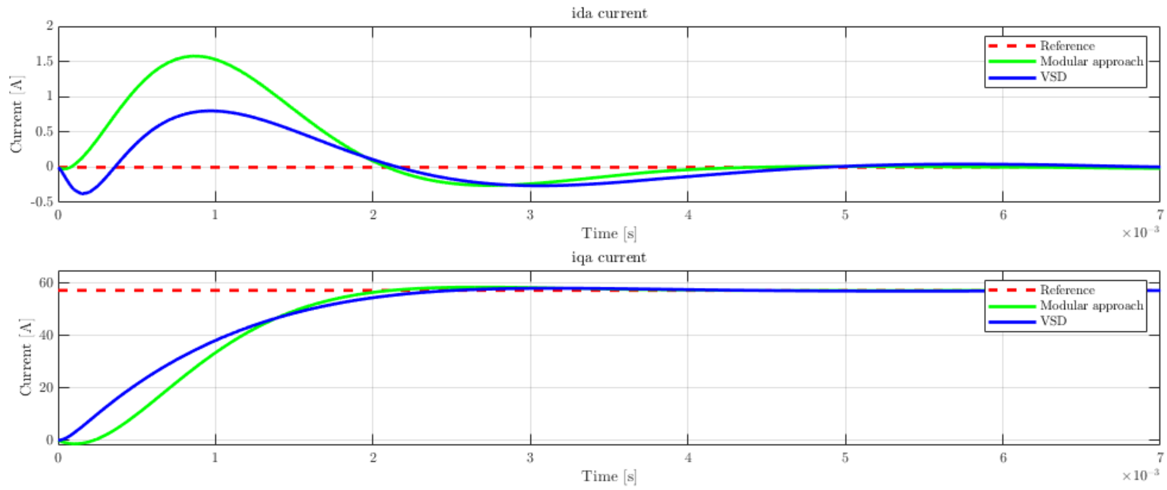

Figure 5.53: SPM - comparison modular approach and VSD

Both control strategies reach steady state in approximately the same amount of time. The main difference lies in the overshoot, which is lower for the VSD control, particularly along the i_d axis.

Feedforward compensation

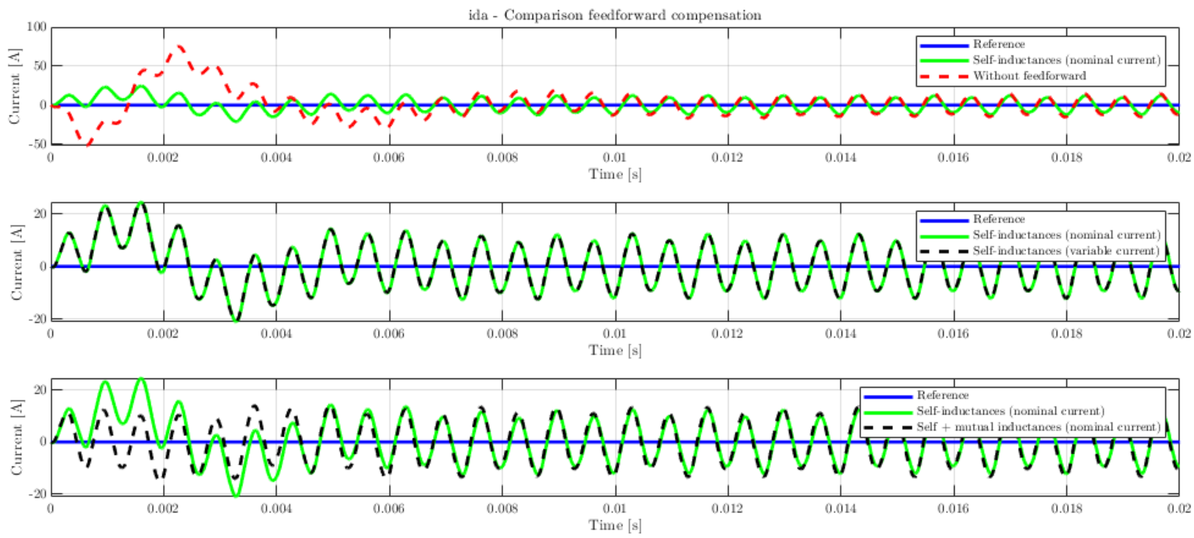

Figure 5.54: SPM - comparison feedforward compensation in d axis

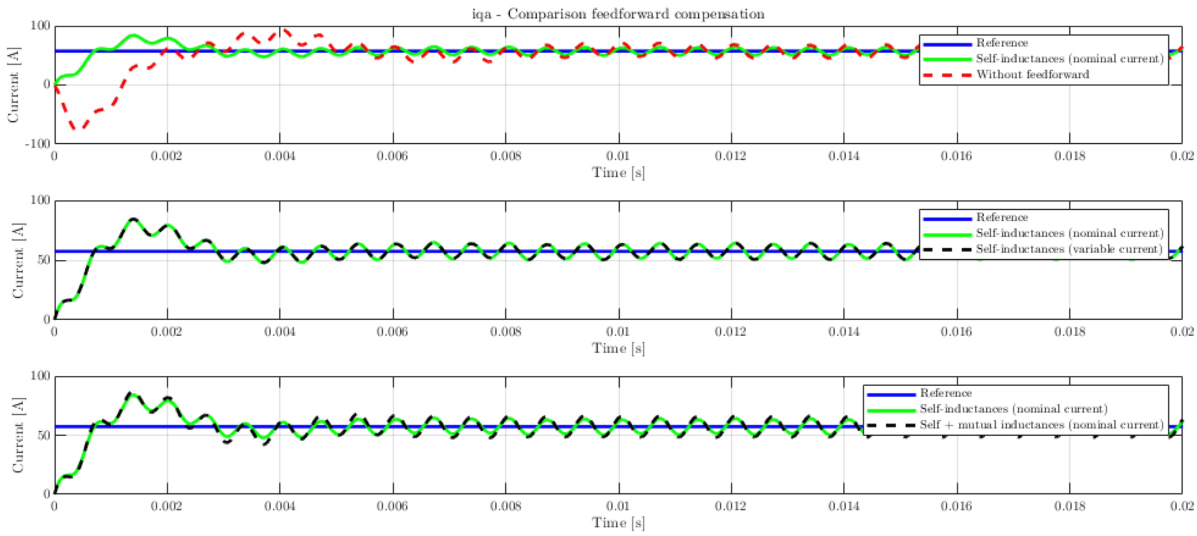

Figure 5.55: SPM - comparison feedforward compensation in q axis

The importance of feedforward compensation is evident in IPM motors, but it becomes even more apparent in SPM motors. In particular, the performance differences are clearly visible when comparing the absence of feedforward compensation to a configuration that includes a feedforward term based solely on self-inductances. Additionally, the mutual inductance plays a significant role, especially along the d-axis.

5.4.2 Efficiency map

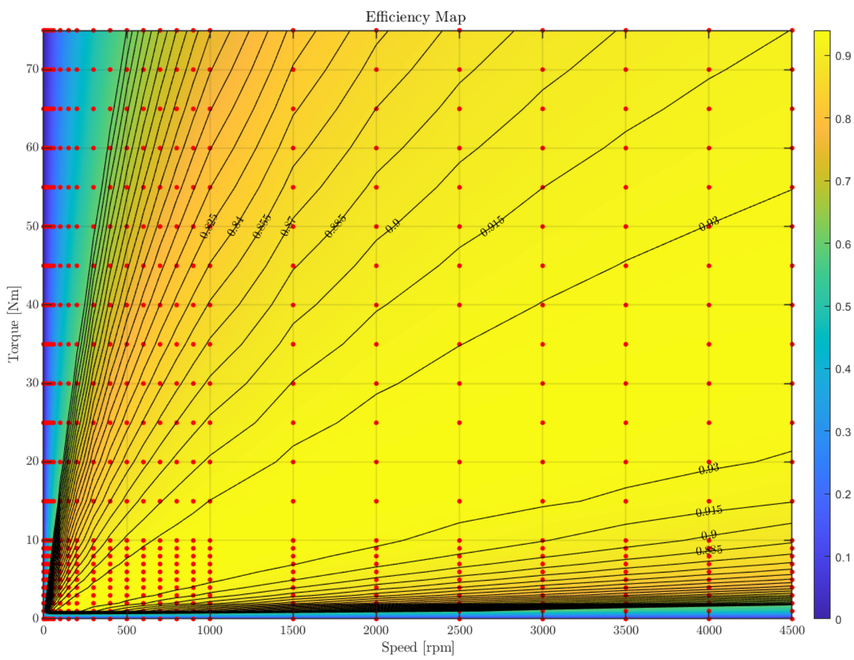

Figure 5.56: SPM - efficiency map

The efficiency map is similar to that presented for the IPM motor; however, when considering the efficiency values, the SPM motor exhibits superior performance compared to the IPM.

5.4.3 Pole position

The same analysis and visualizations performed for the IPM motor are repeated here. The test conditions remain identical; the only substantial difference lies in the dL_{dq} matrix, where the self-inductance values are higher than the mutual inductance.

Fix K_p and K_i

Modular approach

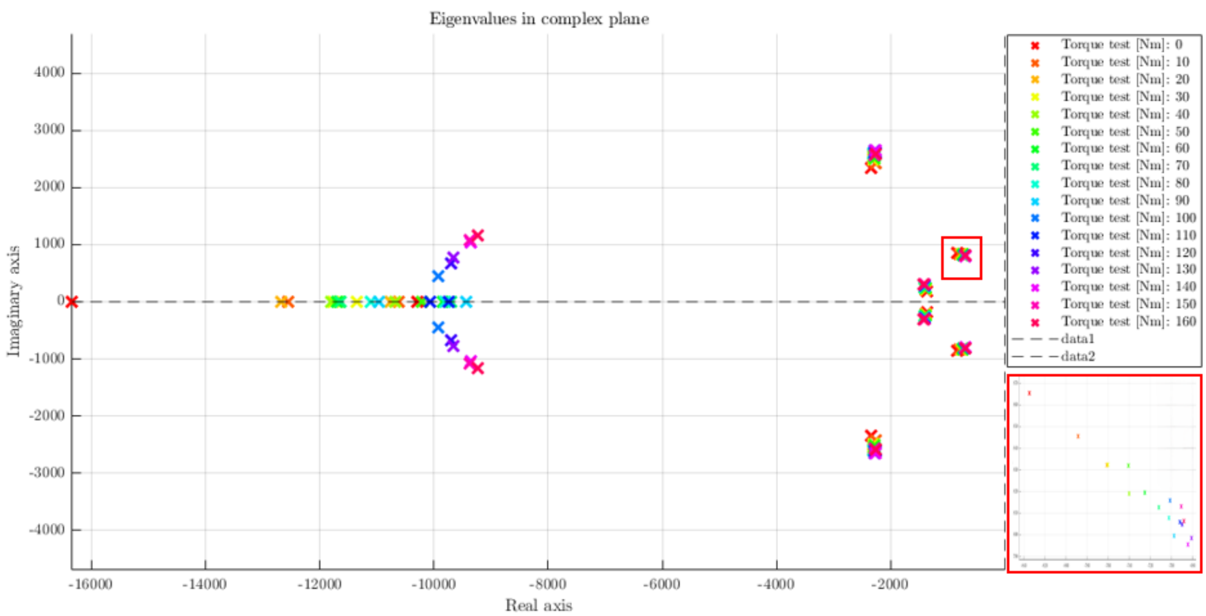

Figure 5.57: SPM - eigenvalues at nominal speed with fixed K_p and K_i

The pole locations are more uniformly distributed than those obtained with the IPM based control. This improvement stems from the fact that the closed-loop system matrix A_{cl} depends on the differential inductance dL_{dq}. In IPM machines, the mutual inductances are comparable to the self-inductances, whereas in SPM machines the self-inductances dominate, leading to better ordered pole placement.
Since the most significant poles are those closest to the origin and the system exhibits symmetry, a zoomed-in view around the real axis is provided within the red box. It can be observed that, even in the case of the IPM machine, the operating point at zero torque deviates the most from the other conditions. However, in this case, it is characterized by high damping and pulsation response.

VSD

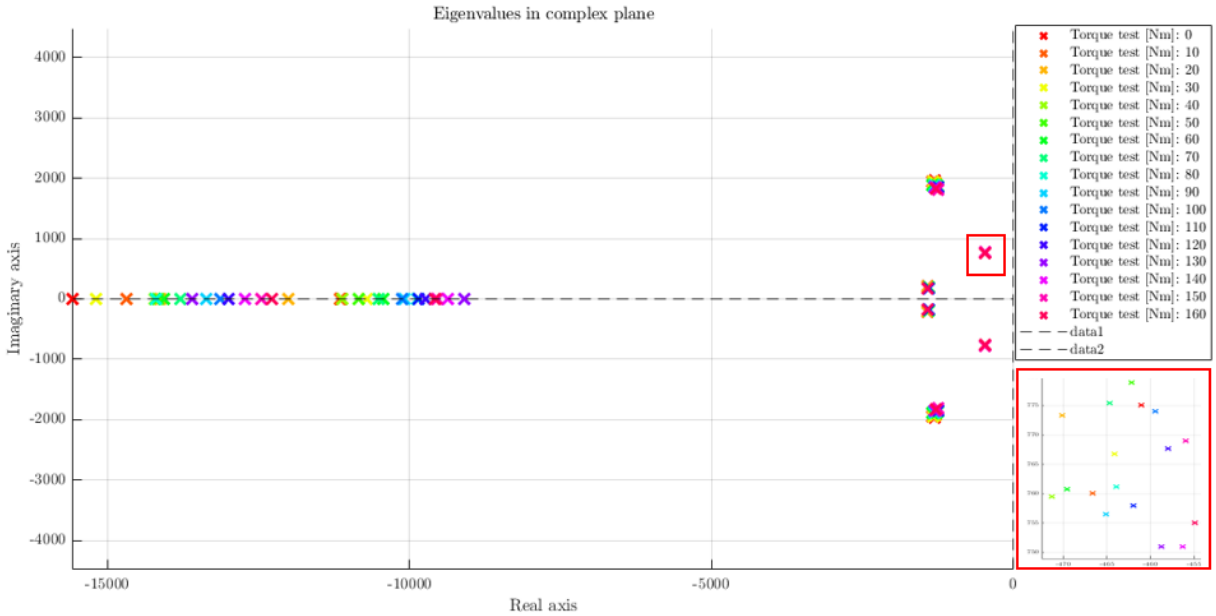

Figure 5.58: SPM - eigenvalues with nominal speed with fixed K_p and K_i VSD

For the VSD, many poles are located along the real axis, particularly those associated with high pulsation. This is more evident compared to the modular approach and is especially pronounced in the case of the IPM motor.

Variable K_p and K_i in function of the reference torque

Modular approach

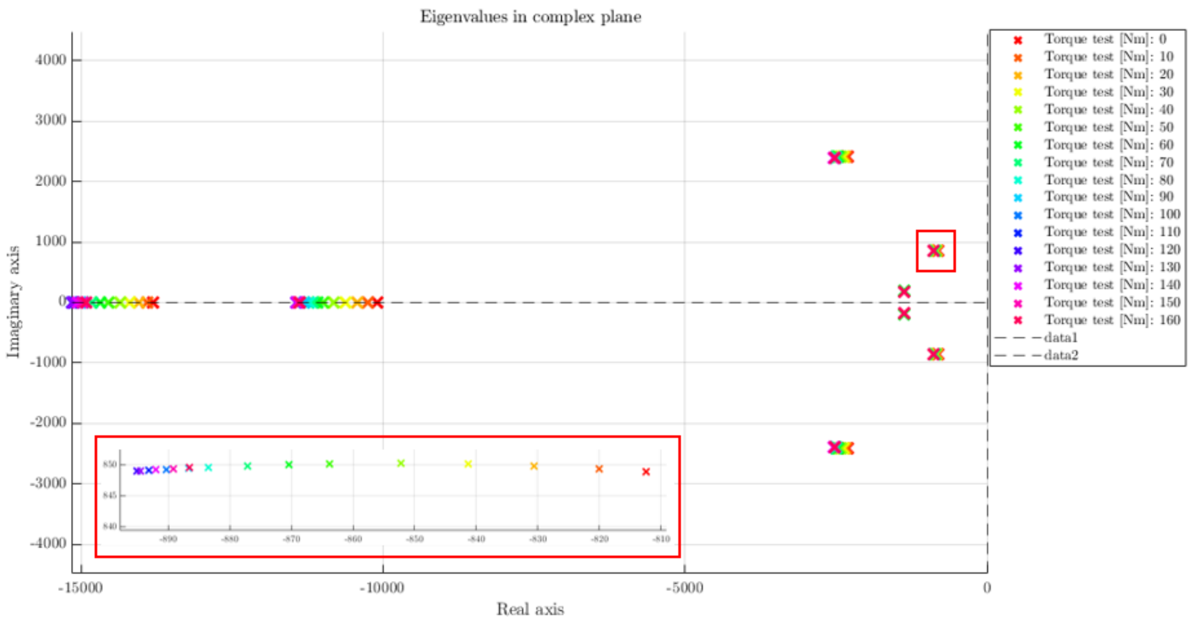

Figure 5.59: SPM - eigenvalues at nominal speed with variable K_p and K_i

The variables K_p and K_i enable the placement of poles along a curved axis, allowing the dominant pole for each reference torque to maintain an approximately constant oscillation frequency across all considered torque levels.

VSD

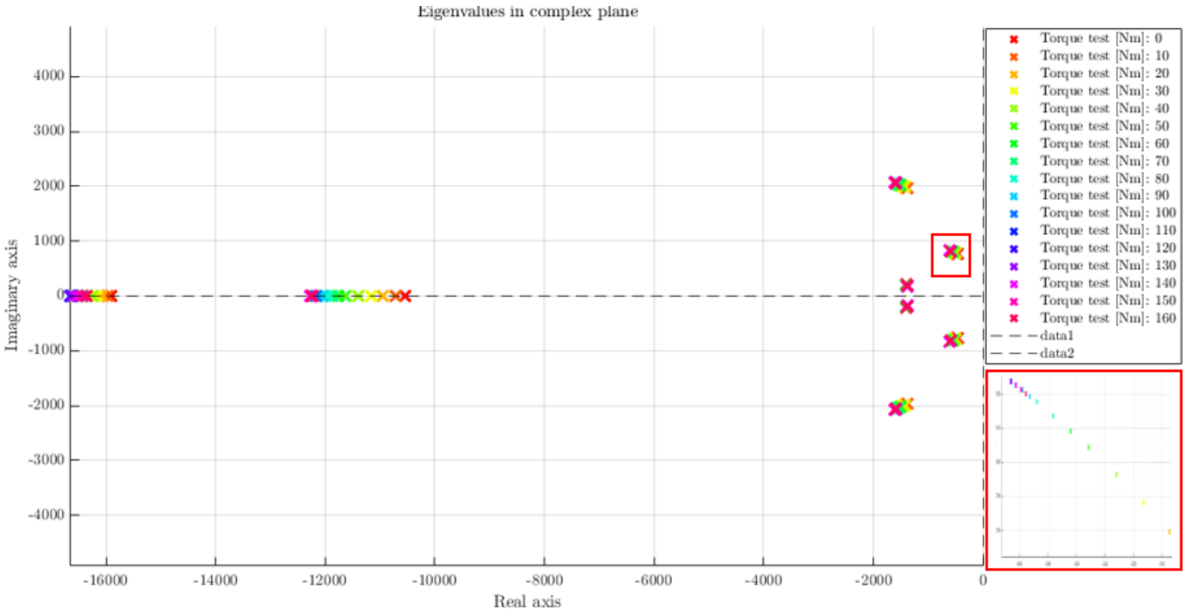

Figure 5.60: SPM - eigenvalues at nominal speed with variable K_p and K_i VSD

The most significant observation is that the pole corresponding to zero torque request is not the most isolated; rather, it is located very close to the pole associated with high torque requests. This characteristic is also observed in VSD systems with fixed K_p and K_i; however, in this case, the poles are aligned along a well-defined curve.

In all previously presented cases, it is evident that all eigenvalues are negative, a necessary condition for system stability, which is the most important parameter.

Chapter 6

Conclusions

This thesis investigates the modeling and control of dual-three-phase permanent magnet motors, encompassing both IPM and SPM types. The study incorporates both linear and nonlinear B–H curves across several control topologies. It begins with the derivation of the machine and control equations for a conventional three-phase system, which are then extended to the dual-three-phase configuration. For both cases, obtaining the complete inductance matrix is essential. In particular, understanding which mutual inductances can be neglected is fundamental for simplifying the control strategy.

Based on the inductance analysis, a modified PI current controller is proposed. This controller is initially tuned under nominal current conditions and then evaluated across multiple gain settings (K_p and K_i). In parallel, both the classical PI controller and an autotuning PI controller are implemented and compared.

Feedforward compensation is studied through four different strategies: (i) no feedforward term, (ii) feedforward using self-inductances evaluated at nominal current, (iii) feedforward using current-dependent self-inductances, and (iv) full feedforward based on the complete inductance matrix.

The stability of the speed loop is analyzed within a SISO framework, using Bode and Nyquist diagrams to assess system stability. For the MIMO current loop, a state-space representation is adopted, and eigenvalue analysis is performed to determine the location of system poles and verify stability.

Validation is conducted through comprehensive simulations in Matlab and Simulink. Key results show that the modified PI controller offers the fastest response with minimal overshoot. Feedforward compensation using self-inductances at nominal current offers a good balance between simplicity, performance, and implementation cost

Speed loop stability margins remain robust throughout the operating range, and current-loop stability is preserved for all control strategies up to twice the nominal torque.

Future Developments

Future work should focus on enhancing the system model by incorporating additional components and effects that were not considered in this study. In particular, the influence of the inverter and the battery must be included to capture the true dynamic behavior of the overall system. Additionally, the motor model currently implemented in Simulink lacks temperature dependence, which should be addressed in future iterations.

The control strategy developed in this thesis is based on maximum torque per ampere. However, a more efficient approach would be to implement maximum torque per efficiency control, which accounts not only for Joule losses but also for iron and inverter losses.

While simulation outcomes are encouraging, further work, particularly experimental testing on prototypes in a realistic environment, is necessary to confirm the accuracy and robustness of the proposed methods.

Bibliography

[1] L. Carbone, “Stability analysis and advanced control strategies for matrix converter,” Ph.D. dissertation, Electrical, Electronics and Telecommunication Engineering and Naval Architecture Department, University of Genova, Genova, Italy, 2024, phD thesis. [Online]. Available: https://iris.unige.it/handle/11567/1175959

[2] W.-S. Jung, H.-K. Lee, Y.-K. Lee, S.-M. Kim, J.-I. Lee, and J.-Y. Choi, “Analysis and comparison of permanent magnet synchronous motors according to rotor type under the same design specifications,” *Energies*, vol. 16, no. 3, p. 1306, 2023. [Online]. Available: https://doi.org/10.3390/en16031306

[3] Y. Hu, Z. Q. Zhu, and M. Odavic, “Comparison of two-individual current control and vector space decomposition control for dual three-phase pmsm,” *IEEE Transactions on Industry Applications*, vol. 53, no. 5, pp. 4483–4492, 2017.

[4] R. Gozdur, P. Gębara, and K. Chwastek, “A study of temperature-dependent hysteresis curves for a magnetocaloric composite based on la(fe, mn, si)-h type alloys,” *Energies*, vol. 13, no. 6, p. 1491, 2020. [Online]. Available: https://doi.org/10.3390/en13061491

[5] D. D. Gaetano, “On multi-phase machines and current harmonic injection for torque capability improvement,” PhD thesis, University of Nottingham, July 2022, available under Creative Commons Attribution license. [Online]. Available: https://eprints.nottingham.ac.uk/id/eprint/68951/

[6] S. Hassaine, S. Moreau, and F. Bensmaine, “Design and hardware implementation of pmsm sliding mode control in siso and mimo cases,” in *2014 IEEE 23rd International Symposium on Industrial Electronics (ISIE)*, 2014, pp. 762–767.

[7] Y.-J. Shin and L. Bleris, “Linear control theory for gene network modeling,” *PLoS ONE*, vol. 5, no. 7, p. e12030, 2010. [Online]. Available: https://journals.plos.org/plosone/article?id=10.1371/journal.pone.0012785

[8] P. K. Panda and R. K. Behera, “Five-phase induction motor drive: A comprehensive review,” *Frontiers in Energy Research*, vol. 11, no. 1, pp. 1–15, 2023, online. [Online]. Available: https://www.frontiersin.org/articles/10.3389/fenrg.2023.1178169/full

[9] R. Bojoi, A. Cavagnino, A. Tenconi, A. Tessarolo, and S. Vaschetto, "Multiphase electrical machines and drives in the transportation electrification," in *2015 IEEE 1st International Forum on Research and Technologies for Society and Industry Leveraging a better tomorrow (RTSI)*, 2015, pp. 205–212.

[10] A. K. Pandey and R. K. Behera, "A review of drive techniques for multiphase machines," *Energy Reports*, vol. 6, pp. 1–14, Jan. 2020, online. [Online]. Available: https://www.researchgate.net/publication/326019070_A_Review_of_Drive_Techniques_for_Multiphase_Machines

[11] D. J. Griffiths, *Introduction to Electrodynamics*, 4th ed. Cambridge University Press, 2017. [Online]. Available: https://www.hlevkin.com/hlevkin/90MathPhysBioBooks/Physics/Physics/Electrodynamics/David%20J.%20Griffiths%20-%20Introduction%20to%20Electrodynamics-Prentice%20Hall%20(1999).pdf

[12] M. N. O. Sadiku, *Elements of Electromagnetics*, 6th ed. Oxford University Press, 2014. [Online]. Available: https://archive.org/details/matthew-n.-o.-sadiku-elements-of-electromagnetic-book-fi/page/12/mode/2up?

[13] G. Sala, M. Mengoni, A. Tani, A. Galassini, and M. Degano, "Advantages of communication in double three-phase surface permanent magnet machines fed by independent inverters," in *2019 21st European Conference on Power Electronics and Applications (EPE '19 ECCE Europe)*, 2019, pp. P.1–P.10.

[14] S. Rubino, O. Dordevic, E. Armando, I. R. Bojoi, and E. Levi, "A novel matrix transformation for decoupled control of modular multiphase pmsm drives," *IEEE Transactions on Power Electronics*, vol. 36, no. 7, pp. 8088–8101, 2021. [Online]. Available: https://ieeexplore.ieee.org/document/9286687

[15] G. Pellegrino, R. I. Bojoi, and P. Guglielmi, "Unified direct-flux vector control for ac motor drives," *IEEE Transactions on Industry Applications*, vol. 47, no. 5, pp. 2093–2102, 2011. [Online]. Available: https://ieeexplore.ieee.org/document/5948379

[16] M. Montelau, "Eigenvalues and eigenvectors (lecture 5–6, computational mathematics)," in Italian. [Online]. Available: https://www.dm.unibo.it/~montelau/html/Lezione5-6_MC.pdf

[17] M. M. Peet, "Spacecraft and aircraft dynamics – lecture 11: Longitudinal dynamics," Lecture notes, 2009. [Online]. Available: https://control.asu.edu/Classes/MMAE441/Aircraft/441Lecture11.pdf

[18] Y. Wang, L. Wu, and S. Chen, "Study on the mode and characteristics of ssos in hybrid ac–dc transmission systems via multitype power supply," *Sustainability*, vol. 15, no. 8, p. 6763, 2023. [Online]. Available: https://doi.org/10.3390/su15086763

[19] S. Hassaine, S. Moreau, and F. Bensmaine, “Design and hardware implementation of pmsm sliding mode control in siso and mimo cases,” in *2014 IEEE 23rd International Symposium on Industrial Electronics (ISIE)*, 2014, pp. 762–767. [Online]. Available: https://ieeexplore.ieee.org/document/6864708

Acknowledgment of AI usage
This thesis has been developed and written with the support of Artificial Intelligence (AI)-based tools, employed as auxiliary instruments to assist in tasks such as language refinement, coding, and preliminary drafting. The use of these tools was conducted in accordance with the principles of academic integrity and transparency defined by the University of Bologna, as outlined on its institutional webpage on Artificial Intelligence in academic activities (https://www.unibo.it/it/ateneo/chi-siamo/intelligenza-artificiale). All conceptual development, critical analysis, and final content decisions were made by the author, who assumes full responsibility for the originality and scientific validity of the work presented.

Acknowledgements

I would like to express my sincere gratitude to the Research Group of Electrical Machines and Drives at the University of Bologna. In particular, I am deeply thankful to my supervisor, Giacomo Sala, for giving me the invaluable opportunity to conduct my thesis work at the University of Nottingham and for his continuous guidance and support throughout every stage of the project.

I would also like to express my heartfelt gratitude to Prof. Michele Degano, Dr. Lorenzo Carbone, and Dr. Meiqi Wang for warmly welcoming me into the Power Electronics and Machines Centre (PEMC) research group in Nottingham. I am especially thankful for the supportive and friendly environment they helped promote, both within and beyond the research group.

A special thanks goes to all the friends I made during my time abroad, and in particular to Antonio, Carlo, Davide, Eric, Fabrizio, Gabriele, Gaia, Luca, Margherita, Riccardo, and Shrey, for their companionship and the unforgettable memories we shared.